

Géotechnique

Exploring the linkage between mechanical behaviour and particle-scale interaction of kaolinite

GEOT-2023-193-R2 | Paper

Submitted on: 18-06-2025

Submitted by: Yohei Nakamichi,Catherine O'Sullivan,Stefano Angioletti-Uberti,Paul Tangney,Sara Bandera

Keywords: CLAYS,PARTICLE-SCALE BEHAVIOUR,COMPUTATIONAL GEOTECHNICS,COMPRESSIBILITY,MICROSTRUCTURE

PDF auto-generated using **ReView**
from


RIVER VALLEY
TECHNOLOGIES

Template for engineering journal articles

- Article type: paper (3000-5000 words, excluding abstract and References list)
- One illustration per 500 words.
- Date text written or revised.
- Number of words in your main text and tables, followed by the number of figures.
- This is an example created from parts of other articles; it is not designed to be read for sense.
- Text should be double line spaced, line numbered and pages should be numbered.

- Exploring the linkage between mechanical behaviour and particle-scale interaction of kaolinite
-

Yohei Nakamichi, PhD

Geotechnical Engineering Department, Technical Research Institute, Obayashi Corporation, Tokyo, Japan

Formerly Department of Civil and Environmental Engineering, Imperial College London, London, UK

0000-0003-1118-2586

Catherine O'Sullivan, PhD, FIEI, FICE, MASCE

Department of Civil and Environmental Engineering, Imperial College London, London, UK

0000-0002-0935-1910

Paul Tangney, PhD

Department of Materials, Imperial College London, London, UK

0000-0003-2917-2415

Stefano Angioletti-Uberti, PhD

Department of Materials, Imperial College London, London, UK

0000-0001-8789-9618

Sara Bandera, PhD

Department of Civil Engineering and Architecture (DICAr), University of Pavia, Pavia, Italy

0000-0001-9389-344X

Full contact details of corresponding author.

Yohei Nakamichi

Geotechnical Engineering Department, Technical Research Institute, Obayashi Corporation, 4-640, Shimokiyoto, Kiyose-shi, Tokyo, 204-8558, Japan

nakamichi.yohei@obayashi.co.jp

In this revision modified text is highlighted in blue, while the original text as per the first revision is in black.

Abstract

The response of clay to mechanical compression is highly dependent on its stress history. Generally, normally consolidated clays exhibit a relatively soft response, while over-consolidated clays exhibit a much stiffer response upon reloading. In the literature this difference has been qualitatively attributed to differences in clay microstructure. This paper uses coarse-grained molecular dynamics simulations to propose that an additional contribution comes from the non-linear, non-monotonic relationship between the inter-particle forces and the separation distances. At large separation distances, clay particles interact via repulsive non-contact forces when the particles initially become close enough to interact. The strength of the mutual repulsion increases with decreasing separation until a maximum repulsive interaction energy, termed an energy barrier, is reached. Once this energy barrier is overcome, the particle interactions become attractive so that the particles effectively become bonded to each other. This paper uses a new approach to interaction models for particle-scale simulation to show that the compressive forces experienced by particles under engineering stress levels are sufficient to push particle pairs into this attractive force regime; and that, upon subsequent unloading, these particles remain bonded to each other. The difference in macro-scale compressibility between normally consolidated and over-consolidated clays can be explained, at least in part, by this attraction and by particles irreversibly bonding together.

Keywords chosen from ICE Publishing list

Clays; Particle-scale behaviour; Compressibility; Computational geotechnics; Microstructure

Notation

Roman symbols

A, B, C	energy scale parameters
a_i, b_i, c_i	ellipsoid radii
$\mathbf{A}_1, \mathbf{A}_2, \mathbf{A}_i$	rotation matrices
A_{E-E}	interaction area for two ellipsoids in the edge-edge configuration
A_{F-F}	interaction area for two ellipsoids in the face-face configuration
$\mathbf{B}_1, \mathbf{B}_2, \mathbf{B}_{12}$	matrices which are defined in terms of the energy matrix and rotation matrix
C_c	compression index
C_s	swelling index
D	ellipsoid diameter
e	void ratio
E	system energy
F	interaction force
$\mathbf{G}_1, \mathbf{G}_2, \mathbf{G}_{12}$	symmetric overlap matrices
H_A	Hamaker constant
h_{12}	surface-to-surface distance
h_{eb}	surface-to-surface distance at the energy barrier
h_{ew}	surface-to-surface distance at the energy well
k, m, n	parameter to control potential energy
k_B	Boltzmann constant
M	mass of particle
N	total number of particles
N_{eb}	number of interactions exceeding the energy barrier
N_{t}	total number of interactions
P	system pressure
p'	mean effective stress
p'_c	pre-consolidation stress
r_{12}	centre-to-centre distance
$\mathbf{r}_{12}$	centre-to-centre vector
$\hat{\mathbf{r}}_{12}$	unit vector related to the centre-to-centre vector
s_1, s_2, s_i	geometrical scaling constants
$\mathbf{S}_1, \mathbf{S}_2, \mathbf{S}_i$	shape matrices
T	temperature of the system
U	potential energy of interaction
$U_{\mathrm{eb}}^{\max}$	local maximum in the potential energy at the energy barrier
U_{ew}^{min}	local minimum in the potential energy at the energy well
U_{EB}	energy barrier potential energy function

U_{GB}	Gay-Berne potential energy function
U_{PR}	purely repulsive potential energy function
$\widehat{U}_{\mathrm{Edl}}$	double layer electrostatic energy per unit area
$\widehat{U}_T$	total energy per unit area
$\widehat{U}_{\mathrm{vdW}}$	van der Waals energy per unit area
$\mathbf{U}_1, \mathbf{U}_2, \mathbf{U}_i$	energy matrices
V	system volume
$\bar{v}$	average velocity of particles

Greek symbols

γ	shift parameter
δ	thickness of the ellipsoids
δ_1, δ_2	thicknesses of the interacting particles
Δt	time step
ε	energy scale parameter
ε_r	relative permittivity
ϵ_0	permittivity of free space
$\epsilon_{ia}, \epsilon_{ib}, \epsilon_{ic}$	relative well depths
η_{12}	dimensionless quantity related particle shape anisotropy
κ	reciprocal thickness of the double layer.
μ, υ	user-specified exponents
σ	minimum effective radius (atomic interaction radius)
σ_{12}	parameter related to inter-particle separation distance
χ_{12}	dimensionless quantity related to the energy anisotropy
ψ_1, ψ_2	surface potentials of the interacting particles

Acronyms

AFM	atomic force microscopy
CGMD	coarse-grained molecular dynamics
CLAYFF	force field for FAMD simulation of clay particles (Cyan et al., 2004)
DEM	discrete element method
DLVO	Derjaguin, Landau, Verwey, and Overbeek
EB	energy barrier
FAMD	fully atomistic molecular dynamics
GB	Gay-Berne
LJ	Lennard-Jones
KDE	kernel density estimation
MD	molecular dynamics

NPT	MD simulation configuration in which the number of particles, the system pressure and the system temperature are controlled.
NVE	MD simulation configuration in which the number of particles, the system volume and the system energy are controlled.
NVT	MD simulation configuration in which the number of particles, the system volume and the system temperature are controlled.
PR	purely repulsive
REV	representative element volume
S-EB	simulations using energy barrier potential
S-PR	simulations using purely repulsive potential
SEM	scanning electron microscope

Introduction

The mechanical behaviour of clay is stress-history dependent. Analysis of scanning electron microscope (SEM) images over the past 10-15 years in particular have provided significant insight into the fundamental mechanisms at play from the perspectives of particle kinematics, electro-chemical processes, and fabric evolution. SEM imaging can capture fabric evolution due to particle rearrangement, evolution of agglomerates (formation and breakdown), and changes in the equilibrium of electrostatic forces, electro-dynamic forces and chemical equilibria. Experimental studies using SEM imaging to study the clay fabric evolution in compression, including Hattab & Fleureau (2010), Zheng et al. (2022), and Guglielmi et al. (2024), have advanced understanding of the evolution of clay fabric, but they could not quantify any changes in the particle interactions. The influence of the particle interactions on the overall behaviour can be indirectly probed by modifying the pore-water chemistry, i.e. the pH or the electrolyte (salt) concentration of the pore-fluid. Pedrotti & Tarantino (2018) and Wang & Siu (2006a) varied the pore-fluid pH in oedometer tests and used SEM imaging to show that kaolinite samples with a dispersed microfabric exhibit a lower initial void ratio and compressibility than kaolinite samples with a flocculated microfabric. Interpretation of these studies has often involved hypothetical particle-scale schematics of clay particle interactions (e.g. Palomino & Santamarina, 2005; Pedrotti & Tarantino, 2018; Wang & Siu, 2006b). Gupta and colleague (Gupta, 2011; Gupta & Miller, 2010) used Atomic Force Microscopy (AFM) to show that particle interactions are highly influenced by the pH of the solution. This contribution complements these earlier studies by exploiting coarse-grained molecular dynamics (CGMD) to further advance understanding of links between the particle-scale interactions and the observed macro- and meso-scale responses.

The specific feature of clay particle interactions considered here is outlined in Fig. 1, which assumes validity of the DLVO (Derjaguin & Landau, 1941; Verwey & Overbeek, 1948) interaction framework and that both interacting surfaces are negatively charged. Figure 1(a) shows the variation in the interaction energy (U) with h_{12}, the particle surface-surface distance, while the variation in the interparticle force, F with h_{12}, is illustrated in Fig. 1(b). F and U are related as $F = -dU/dh_{12}$ and both F and U have a non-monotonic relationship with h_{12}. Consider the case where two particles approach each other from a distance (i.e. a very large h_{12} value) so that $U =$

0. Once the particles start to interact, there is a non-monotonic relationship between h_{12} and U. U continues to increase with decreasing h_{12} until U attains a local maximum, $U = U_{\mathrm{eb}}^{\max}$ at $h_{12} = h_{\mathrm{eb}}$, of the interaction energy termed an "energy barrier", where the subscript eb denotes "energy barrier". At $h_{12} = h_{\mathrm{eb}}$ the interaction force, F, changes from being repulsive to attractive. U then decreases with decreasing h_{12} until a local minimum, $U = U_{\mathrm{ew}}^{\min}$ at $h_{12} = h_{\mathrm{ew}}$, is reached, where the subscript ew denotes "energy well". When $h_{\mathrm{ew}} < h_{12} < h_{\mathrm{eb}}$ the two particles experience a strong mutual attraction and for $h_{12} < h_{\mathrm{ew}}$ there is a mechanical repulsive force, sometimes termed Born repulsion. Therefore, once the particles have been pushed close enough together to overcome the energy barrier at $h_{12} = h_{\mathrm{eb}}$, the particles are held together firmly at a separation of $h_{12} \approx h_{\mathrm{ew}}$.

This contribution examines the possibility that the non-monotonic nature of the $U - h_{12}$ and $F - h_{12}$ relationships illustrated in Fig. 1 can explain, at least in part, the differences in macro-scale stiffness between normally consolidated clay and over-consolidated clay. The key question is whether, for stress levels of geotechnical engineering interest, the forces that push pairs of clay particles together during normal consolidation are sufficient to overcome their strong mutual repulsion and overcome the energy barrier so that the particle interactions become attractive, and the particles effectively become bonded to each other within the energy well at $h_{12} \approx h_{\mathrm{ew}}$. The term "bond" is used to describe the attraction between the particles because, once $h_{12} < h_{\mathrm{eb}}$, the height, $U_{\mathrm{eb}}^{\max} - U_{\mathrm{ew}}^{\min}$, of the energy barrier that must be surmounted to separate them is significantly larger than the height $U_{\mathrm{eb}}^{\max}$ of the energy barrier that was surmounted to push them together. Therefore, unless the particles are pulled apart very strongly during unloading, they will be unable to leave the energy well at $h_{12} \approx h_{\mathrm{ew}}$. Effectively, they will have formed a physical bond (Israelachvili, 2011). If this were to be the case, the particles would not separate during unloading, which would contribute to a lower void ratio and might help to explain the formation of flocculated clusters, domains, and stacks that have been reported in SEM studies.

The hypothesis put forward here is explored using clay particle-scale CGMD simulations and interaction models specifically developed to look at the impact of the energy barrier. The clay

mineral considered is kaolinite. This paper firstly contextualizes the research by introducing prior discussions on fabric evolution during compression. Then kaolinite particle interactions within the DLVO framework are discussed, before the details of the numerical model are outlined and a new type of potential function that can be calibrated against DLVO-generated data and that can capture the energy barrier is described. The results of simulations of isotropic compression and unloading of assemblies of more than 100,000 kaolinite particles are then presented to show that a model that considers the non-monotonic nature of particle interactions can capture the irreversible response of clay in compression.

Clay particle interactions

Particle-scale simulations using either CGMD or the discrete element method (DEM) require an analytical or numerical model of how F or U varies with h_{12} and with relative particle orientation. Two options are available to develop interaction models informed by the fundamental physics of the interactions: (i) models developed from fully atomistic molecular dynamics (FAMD) simulations, (ii) models based on Derjaguin, Landau, Verwey, and Overbeek (DLVO) theory. Data from both types of models informed the current study.

Fully atomistic molecular dynamics (FAMD)

In FAMD, both the clay particles and the surrounding pore-fluid (or solution) are modelled at the atomic level (i.e. each atom and molecule in the clay platelets and solution are explicitly modelled individually). Examples of research that has used FAMD to study clay platelets and their interactions include Boulet et al. (2004), Ebrahimi et al. (2014), Honorio et al. (2017) and Zhu et al. (2022). These studies have mostly focused on small, active clay particles such as montmorillonite. The number of atoms that can be considered in FAMD simulations renders modelling a single kaolinite particle with 70–140 units layers of aluminosilicate challenging due to the high computational cost (Casarella et al., 2024). Some studies (e.g. Luo et al., 2022; Volkova et al., 2021; Zen et al., 2022) have modelled kaolinite particles in the FAMD framework, but they consider only a couple of layers of aluminosilicate units of kaolinite particles and the resultant data cannot be used in CGMD or DEM simulations. Authors including Güven (1992), Israelachvili (2011) and Mitchell & Soga (2005) have stated that FAMD is the most effective approach to

accurately define interactions between clay particles. However, results of systematic studies of pairwise force fields for oxides and water (e.g. Jing et al., 2019; Tangney & Scandolo, 2002; Wernersson & Jungwirth, 2010), like those used by Ebrahimi et al. (2014), have revealed inaccuracies so that it is more accurate to state that these models are qualitatively correct. These issues of computational cost and accuracy prompted use of DLVO theory in this research. However, the FAMD simulations in Ebrahimi et al. (2014), Zen et al. (2022) and Zhu et al. (2022) predicted relatively complex U - h_{12} relationships with multiple energy barriers and energy wells, leading to alternate attractive and repulsive forces between two particles as their separation, h_{12}, reduces. Observation of the FAMD data in Ebrahimi et al. (2014) was the initial catalyst for the exploration of the mechanical significance of the local minima described in the current study.

Derjaguin, Landau, Verwey, and Overbeek (DLVO) theory

DLVO theory (Derjaguin & Landau, 1941; Verwey & Overbeek, 1948) was used to obtain the parameters in the clay particle interaction models used in the CGMD model presented below. DLVO theory was developed to explain the stability of colloidal suspensions and is often used to describe interactions between clay particles in geotechnical engineering (e.g. Mitchell & Soga, 2005). As shown in Fig. 2, DLVO theory considers the interaction energy to have a contribution from the van der Waals forces and a contribution from the electrical double-layer. DLVO theory can provide an analytical expression describing the interaction energy (usually per unit area) between two particle surfaces assumed to be infinite parallel planes and provide the necessary information to develop particle-based models of clay. DLVO theory is based on several unrealistic assumptions such as low salt concentrations, low and uniform surface charges, and ignores ion size and particle shape effects (Mitchell & Soga, 2005; Ebrahimi et al., 2014; Carrier, 2013; Casarella et al., 2024). Some researchers (e.g. Carrier, 2013; Ebrahimi et al., 2014) contend that DLVO theory is inadequate in representing actual particle interactions at short separation distances (less than 1 nm). However, for clay particles sized in the micron range, such as kaolinite clay particles, the DLVO limitations are less significant than the case for smaller montmorillonite particles. In a more general discussion on CGMD, Angioletti-Uberti (2017) argued that all of the fine details of the energy-separation distance relation may not be needed for a correct prediction of meso-scale or integrated properties, as long as the gross features, such as the presence of

minima, or barriers, and their relative positions, are correctly captured. DLVO theory has been applied to develop the contact models used in many recent particle-scale simulations of clay which have demonstrated reasonable macro-scale behaviour (e.g. Aminpour & Sjoblom, 2019; Anandarajah, 2000a; Guo & Yu, 2023; Jaradat & Abdelaziz, 2019; Liu, 2015; Niu & Jiang, 2023; Sjoblom, 2016; Yao & Anandarajah, 2003).

Published AFM data support the application of DLVO theory to kaolinite particles. AFM measures interaction forces between a nanoscopic tip and a clay particle surface (Ducker et al., 1991, 1992; Israelachvili, 2011) and so cannot be directly used to develop interaction models for use in CGMD. Previous AFM studies of kaolinite include Gupta (2011), Kumar (2017), and Liu (2015). Gupta (2011) and Kumar (2017) interpreted their data within a DLVO framework; so their research provides particle-scale empirical data in support of the application of DLVO theory to describe the overall interaction forces of clay various conditions (pH and salt concentration). Importantly the AFM data in Gupta (2011) and Kumar (2017) confirm the existence of a local maximum in repulsive force at $h_{12} \approx 1$ nm for pH values of 6 and 9. At smaller separation distances the interaction shows either a small repulsion or an attraction. This experimental evidence for this existence of an energy barrier motivated the hypothesis explored in this paper. Here material parameters derived from AFM studies were used in the DLVO model of the particle interactions used to calibrate the potential function that was implemented in the CGMD modelling framework.

Linking overcoming the energy barrier to the irreversible behaviour of clay during consolidation

Moving interactions into the energy well by lowering the energy barrier

The idea of using salt to promote flocculation of colloidal particles is well known. The height of the energy barrier introduced in Fig. 1 is influenced by the pH and the salt concentration of the pore-water surrounding the clay particles (Israelachvili, 2011; Butt, 2003). Researchers including Herrington et al. (1992), Braggs et al. (1994) and Gupta (2011) used the potentiometric titration technique to examine the salt concentration effect on the surface of kaolinite particles. They showed that the magnitude of the surface charge of kaolinite particles increases with an increase in salt concentration in alkaline pore-water. This is because, as salt concentration increases, the

thickness of the double layer decreases and more ions are adsorbed on the particle surfaces. Although the magnitude of the surface charge density increases, the repulsive forces between particles decrease due to the reduction of the thickness of the double layer, resulting in a decrease in the height of the energy barrier (Masliyah & Bhattacharjee, 2005; Trefalt, 2016; Trefalt et al., 2020) (see Fig. 2). Several researchers (e.g. Palomino & Santamarina, 2005; Wang & Siu, 2006b; Won & Burns, 2023) showed that the salt concentration in suspensions of clay particles influences deposition behaviour of kaolinite particles. They indicated that a low energy barrier due to high salt concentration promotes the formation of aggregated and flocculated microfabrics. The aggregates can, however, be broken apart relatively easily as the attractive forces only exist within relatively low energy barriers. The sensitivity of kaolinite in compression to variations in the salt concentration was also shown in contributions including Ajmera & Tiwari (2014) and Wang & Siu (2006a). Looking beyond kaolinite, one example of pore chemistry influences on clay compression behaviour is the significant reduction in volume of saturated samples of Ponza bentonite in an oedometer upon exposure to NaCl, KCl and $CaCl_2$ solutions detailed in Di Maio (1996) and cited in Gens (2010). One can hypothesize that the introduction of the electrolyte lowered the energy barriers in the particle interactions leading to a collapse in the clay fabric as particle interactions moved into the energy wells.

Moving interactions into the energy well by mechanically overcoming the energy barrier

From Fig. 1, the following mechanism for irreversible behaviour of clay during consolidation is explored: As a clay is consolidated along the initial compression line, and the interparticle separation distances reduce, the energy barrier is overcome for a significant number of interacting particle pairs. These pairs then continue to experience an attractive interaction (physical bond) that remains stable when the pressure is released, and the clay becomes over-consolidated. The higher stiffness of over-consolidated clays is due, at least in part, to some of the particles bonding physically and irreversibly to one another during the initial compression. In other words, the relatively stable clusters or clumps that have been observed in the SEM studies of clay cited above may be a consequence of (i) the position of the energy barrier, which depends on the clay mineralogy and the pore-fluid chemistry or (ii) interaction forces that are sufficiently large to overcome the maximum repulsive force indicated schematically in Fig. 1(b). Other authors have

noted that when interactions between individual colloids overcome the energy barrier, irreversible aggregation can occur (e.g. Goehring et al., 2010). However, no prior simulation study has linked the contact-level overcoming of the energy barrier with the response of clay to mechanical compression.

Development and calibration of interaction model for coarse-grained molecular dynamics

Available frameworks for particle-scale simulation of clay

Particle-scale simulations are often used to generate the data needed to develop rational explanations for complex phenomena observed in laboratory tests, rather than to reproduce physical response (Potyondy & Cundall, 2004). DEM is well-established as a tool for exploring sand behaviour (O'Sullivan, 2011). In contrast to sand, the application of particle-scale simulation to study clay behaviour is still in the early stages due to the geometric complexity of clay particles and the challenges in characterizing their interactions. DEM models particle interactions through a force-separation relationship. While some researchers have utilized DEM to simulate clay behaviour, these efforts have been limited. For instance, 2-D models have employed line elements or small groups of connected disks (Anandarajah, 1994, 2000a, 2000b; Pagano et al., 2020), offering conceptual insights. Yao and Anandarajah (Yao, 2001; Yao & Anandarajah, 2003) utilized 3-D cuboid particles to model kaolinite; however, the small number of particles considered (400 particles) is not representative of real-world scenarios. de Bono & McDowell (2022a, 2022b, 2023a, 2023b) used composite particles that modelled a single clay particle as being composed of spherical sub-particles, each of which was itself a composite particle representing many atoms. The use of composite particles allows us to explicitly capture the physicochemical properties of each surface of a clay particle (i.e. in the case of a kaolinite particle, the alumina face, the silica face, and the edge surface) into a rigid body. However, this modelling method is computationally expensive: de Bono & McDowell (2023b) used over 1,200 sub-particles per single clay particle and in simulations with only 4,080 clay particles. Due to the high computational cost, it is difficult or impossible to simulate a large enough number of clay particles to yield a representative element volume (REV), which is the smallest volume that can be measured or simulated to produce results representative of the entire material. Bandera et al. (2021) indicated that, in the case of clay systems, the number of particles required to achieve a REV is on the order of 100,000 or higher.

The number of particles in a REV for clay is larger than in the case of granular materials including sand, as a consequence of the meso-scale stacks, domains, or aggregates of clay particles that form, as is well documented in the SEM studies above and in the seminal contribution by Collins & McGown (1974) and Sides & Barden (1971).

CGMD is a type of molecular dynamics (MD) that uses larger particles (in comparison with FAMD) to model the groups of atoms and molecules that comprise clay particles. CGMD is algorithmically similar to DEM, but CGMD considers interactions in terms of the relationship between potential energy and separation using a potential function (potential function describes potential energy between two particles as a function of their separation distance). Similar to the DEM simulations conducted by de Bono & McDowell (2022a, 2022b, 2023a, 2023b), Sjoblom (2016) used CGMD to simulate kaolinite, with each kaolinite particle modelled as a composite of spherical sub-particles (the sub-particles are not atoms, and so this is a CGMD framework). Liu et al. (2015) also used composites of spherical sub-particles to simulate flocculation in suspensions. As is the case with DEM, due to the large number of sub-particles in these simulations, it is impossible to achieve a simulation with a sufficient number of particles to obtain a REV. However, the computational cost can be significantly reduced by modelling each clay particle as a single aspherical particle, rather than as a composite of many spherical sub-particles. Ebrahimi et al. (2014) approximated montmorillonite clay particles as rigid ellipsoids to examine particle behaviour under isotropic compression. Later, Bandera et al. (2021) applied the same modelling strategy (i.e. clay particles were modelled as rigid ellipsoids) to kaolinite particles to examine the particle-scale behaviour of kaolinite during compression tests. Bandera et al. (2021) showed that their CGMD simulations using ellipsoids can simulate systems with hundreds of thousands of particles a low enough computational cost to attain a REV. The current contribution develops upon the CGMD approaches documented in Ebrahimi et al. (2014) and Bandera et al. (2021).

Assumed conditions

This study considers kaolinite saturated in a pH=8 (alkaline) pore-water with a KCl (potassium chloride) salt concentration of 1 mM. This scenario was selected because the surface potential values required for DLVO theory can be obtained from the AFM data in Gupta et al. (2011), and

particle interactions are similar to the idealized particle interaction shown in Fig. 1, i.e. it can be assumed that the alumina face and silica face possess identical surface charges. Here one clay particle is taken to be a platelet comprising 70-140 aluminosilicate layers (as in Casarella et al., 2024).

DLVO expressions used to calibrate CGMD potential functions

DLVO theory gives the interaction energy per unit area between two semi-infinite parallel plates as a function of their surface-to-surface distance (h_{12}). While the Derjaguin approximation (Derjaguin, 1934; Israelachvili, 2011) enables the extension of the theory to finite-sized particles of arbitrary shape, the complexity of its implementation means that the interaction energy between clay particles is most often described as the energy per unit area of the particle surface without considering particle morphology.

In DLVO theory, the total interaction energy per unit area, $\widehat{U}_T$ [J/nm^2], is the sum of the van der Waals energy, $\widehat{U}_{vdW}$ [J/nm^2], and the double layer electrostatic energy layer, $\widehat{U}_{Edl}$ [J/nm^2], i.e.:

$$\widehat{U}_T = \widehat{U}_{vdW} + \widehat{U}_{Edl} \tag{1}$$

Following Gupta (2011), $\widehat{U}_{vdW}$ can be expressed as:

$$\widehat{U}_{vdW} = -\frac{H_A}{12\pi}[h_{12}^{-2} + (h_{12} + \delta_1 + \delta_2)^{-2} - (h_{12} + \delta_1)^{-2} - (h_{12} + \delta_2)^{-2}] \tag{2}$$

where δ_1 [nm] and δ_2 [nm] are the thickness of the plates, and H_A [J] is the Hamaker constant.

Here, assuming that clay particles have constant and low surface potential, $\widehat{U}_{Edl}$ between two interacting plates with different surface potentials can be expressed by the Hogg–Healy–Fuerstenau expression (Bandera, 2022; Gupta, 2011; Nguyen & Schulze, 2003):

$$\widehat{U}_{Edl} = \varepsilon_r \epsilon_0 \kappa \left[\frac{2\psi_1\psi_2 \exp(\kappa h_{12}) - \psi_1^2 - \psi_2^2}{\exp(2\kappa h_{12}) - 1}\right] \tag{3}$$

where ψ_1 [mV] and ψ_2 [mV] are the surface potentials of the two plates (surfaces), ε_r [-] is the relative permittivity, ϵ_0 [F/m] is the permittivity of the free space, and κ [nm^{-1}] is the reciprocal thickness of the double layer.

Table 1, developed with reference to Gupta (2011), gives the DLVO parameters for kaolinite particles saturated by pore-water (potassium chloride solution) with pH = 8 and salt concentration of 1 mM for the silica face surface-to-alumina face surface (face-face) configuration and the edge surface-to-edge surface (edge-edge) configuration.

The simulations presented here considered ellipsoidal particles 2,000 nm in diameter and 200 nm thick. Following Bandera et al. (2021), the DLVO energy (in J) for interaction between two ellipsoids was obtained by multiplying the DLVO energy per unit area by the interaction areas defined as $A_{F-F} = \pi \times (D/2)^2 \times \delta$ and $A_{E-E} = (\pi \times D)/2 \times \delta$ for the face-face and the edge-edge configurations, respectively, where D is the particle diameter and δ is the thickness. As the full thickness (δ) is used the ellipsoid tapering does not impact the edge-edge interactions, although the geometric idealization of a pseudo-hexagonal shape as an ellipsoid remains. The data denoted DLVO in Fig. 3 (also in Fig. 4) show the variation in the (total) DLVO interaction energy (in J) and the surface-to-surface distance for the face-face and edge-edge for the ellipsoids used in the simulations presented here. The DLVO generated data resemble the idealised interaction profile shown in Fig. 1(a), however, the DLVO does not consider the Born repulsion at very short range (see Figs 1(a) and (b)). The face-to-edge/edge-to-face interactions cannot directly be considered. The DLVO data were used to calibrate or tune simpler potential function expressions that could be used within a CGMD modelling framework.

Using the surface potential data for the pore fluid conditions here, the DLVO framework predicts that both faces and the edges are negatively charges so that all interactions (face-face, face-edge and face-face) are repulsive. All kaolinite particles have a silica face and an alumina face, so including the edges, there are three surface types. Gupta (2011) and Gupta et al. (2011) showed that all three surfaces have different charges that depend on the pore-water chemistry (i.e. the pH and salt concentration), resulting in different interaction energy (U) and particle separation (h_{12}) relationships depending on relative particle configuration. In the case of pH=4 (acidic pore-water) there is a surface charge anisotropy (i.e. the alumina face is positively charged, the silica face remains negatively charge and the edges are positively charged). Refer to Bandera et al. (2024) and Nakamichi et al. (2024) for a more detailed discussion on this point.

Mechanical or contact force

As shown in Fig. 1(b), the mechanical (contact) force is a short-range repulsion that exists for $h_{12} < h_{ew}$ that rapidly increases with decreasing surface-to-surface distance to prevent particle penetration. This force is quantum-mechanical in nature, and it is often termed Born repulsion (Israelachvili, 2011). As outlined in Israelachvili (2011), there is no agreement on a specific analytical expression to describe Born repulsion. However, the exact form of the relationship between force and h_{12} in this region is not crucial for the analyses presented here so long as the repulsion is strong enough to counterbalance the effects of van der Waals attraction at short distances.

Framework used for CGMD potential functions

Building upon Bandera et al. (2021) and Ebrahimi et al. (2014), in the CGMD simulations presented here, the clay particles are idealized to be flat ellipsoids (oblate spheroids), and the Gay-Berne (GB) potential function (Everaers & Ejtehadi, 2003; Gay & Berne, 1981) was adopted as a basis/framework to develop equations relating the interaction energy and the particle separations. Modified forms of the GB potential function were used in the CGMD model because the DLVO expressions given by Eqs (1)-(3) cannot be directly used to describe interaction energy between clay particles with finite shapes and arbitrary orientations in 3-D space. The GB potential function is an anisotropic form of the Lennard-Jones (LJ) potential function, a typical potential function used in MD simulations to describe interactions between atoms. The GB potential can account for the energy and shape anisotropy of an ellipsoid.

In a CGMD framework where a clay particle is modelled using a flat ellipsoid, the GB potential energy (U_{GB}) is given by:

$$U_{GB} = 4\varepsilon\left[\left(\frac{\sigma}{h_{12}+\gamma\sigma}\right)^{12} - \left(\frac{\sigma}{h_{12}+\gamma\sigma}\right)^{6}\right] \times \eta_{12} \times \chi_{12} \quad (4)$$

where ε is the energy scale parameter, σ is the atomic interaction radius (minimum effective particle radius), γ is the shift of the potential minimum, and η_{12} and χ_{12} are parameters related to the shape and energy anisotropy, respectively.

Equation (4) is similar in form to the LJ potential function. However, whereas the LJ potential function is a function of the centre-to-centre distance between two spheres, the GB potential function is a function of the surface-to-surface distance (closest distance) between two ellipsoids, which varies depending on their relative orientation. The details of the calculation of h_{12}, η_{12} and χ_{12} are included in an Appendix to this paper.

Use of the GB potential function requires the ellipsoid semi-axis lengths (denoted by a_i $(= b_i)$, and c_i). There are additional five tuneable parameters, i.e. ε, σ, γ, ϵ_{ia} $(= \epsilon_{ib})$, ϵ_{ic} that lack a precise physical interpretation and need to be calibrated. An underlying assumption of the GB potential function is that the potential energy in intermediate configurations (e.g. face-edge/edge-face configurations when the particle long axes are mutually orthogonal) can be correctly extrapolated using the same tuned parameters providing the face-face and edge-edge configurations (Gay & Berne, 1981). As previously indicated in Bandera et al. (2021), the potential expression defined in Eq. (4) cannot reproduce the energy barrier.

Purely repulsive (PR) potential function

This study considers two potential functions, the first is a purely repulsive (PR) potential (U_{PR}) originally proposed in Bandera et al. (2021) who assumed that the interaction energy at short surface-to-surface distances does not highly affect mechanical response of clay. Bandera et al. (2021) implemented U_{PR} by removing the attractive term from the GB potential function so that:

$$U_{PR} = 4\varepsilon\left(\frac{\sigma}{h_{12} + \gamma\sigma}\right)^{12} \times \eta_{12} \times \chi_{12} \quad (5)$$

Bandera et al. (2021) calibrated the parameters required in U_{PR} against DLVO theory for $h_{12} > h_{\mathrm{eb}}$, i.e. they did not consider the energy barrier. They showed that the U_{PR} can capture the fundamental features of mechanical response that normally consolidated kaolinite exhibits during initial loading. However, they did not examine its ability to simulate unloading and reloading. Bandera et al. (2021) manually calibrated the U_{PR} parameters using trial and error; here the Levenberg–Marquardt (mini-max) algorithm (Levenberg, 1944; Marquardt, 1963) was

implemented to calibrate the U_{PR} parameters using the DLVO-generated data. Both the face-face and the edge-edge configurations were considered. Table 2 shows the calibrated parameters for the current study, and Fig. 3 compares the calibrated U_{PR} with the DLVO theory.

Energy barrier (EB) potential function

A new energy barrier (EB) potential function (U_{EB}) was developed by augmenting the GB potential function in Eq. (4) to capture the variation in interaction energy with separation distance shown in Fig. 1(a). U_{EB} is given by:

$$For\ h_{12} > h_a:\quad U_{\mathrm{EB}} = \left[A\left(\frac{\sigma}{h_{12}+\gamma\sigma}\right)^{12} - B\left(\frac{\sigma}{h_{12}+\gamma\sigma}\right)^{6} + C\left(\frac{\sigma}{h_{12}+\gamma\sigma}\right)^{3}\right] \times \eta_{12} \times \chi_{12} \tag{6a}$$

$$\text{For } h_{12} < h_a:\quad U_{\mathrm{EB}} = (kh_{12}^2 + mh_{12} + n) \times \eta_{12} \times \chi_{12} \tag{6b}$$

where h_a is the position of the maximum attractive force (i.e. maximum gradient of the potential energy profile), A, B and C are new, tuneable, energy scale parameters introduced in place of ε in the GB potential function (see Eq. (4)). k, m and n are tuneable parameters that were calibrated so that the two expressions in Eqs (6a) and (6b) connect continuously and smoothly at $h_{12} = h_a$. U_{EB} has 10 tuneable parameters requiring calibration ($\epsilon_{ia}(=\epsilon_{ib}), \epsilon_{ic}, \sigma, \gamma, A, B, C, k, m, n$), while the U_{GB} has 5 tunable parameters ($\epsilon_{ia}(=\epsilon_{ib}), \epsilon_{ic}, \sigma, \varepsilon, \gamma$).

The first term in Eq. (6a) aims to reproduce the very short-range repulsion, i.e. Born repulsion, the second term aims to reproduce short-range attraction, and the third term aims to reproduce the medium- and long-range repulsion. Although the new parameters (A, B and C) are introduced, the substantial major change from U_{GB} (see Eq. (4)) is the introduction of the third term, i.e. the medium- and long-range repulsion. Introducing the third term allows U_{EB} to have a local maximum as well as a local minimum, i.e. U_{EB} can reproduce both the energy well and the energy barrier. However, the initial calibration results showed that while the EB potential given in Eq. (6a) captures the DLVO-generated data, the slope of the Born repulsion was quite steep. The time integration algorithm used requires a time increment that is inversely proportional to the square root of this stiffness, and the timestep required for integration using the calibrated EB potential function was prohibitively small to obtain results with a tractable computational cost. These considerations motivated the development of Eq. (6b). In the course of developing this potential

expression, alternative candidate expressions were explored, and Eqs (6a) and (6b) differ from the expression documented in Nakamichi et al. (2023).

To constrain the calibration process, the tuneable parameters were determined to satisfy the following four conditions:

i. To simplify the energy scale, $\epsilon_{ic} = 1.0$, A=2B=C, and $\gamma = 1.0$.
ii. In the face-face configuration, $U_{\mathrm{eb}}^{\max}$ equals the DLVO theory prediction.
iii. In the face-face configuration, h_{eb} equals the DLVO theory prediction.
iv. In the edge-edge configuration, the $U_{\mathrm{eb}}^{\max}$ equals the DLVO theory prediction (the position of the energy barrier does not equal the DLVO theory prediction, rather it equals the position for the face-face configuration).

Figure 4 shows that when the U_{EB} is calibrated against DLVO theory using the Levenberg–Marquardt algorithm (Levenberg, 1944; Marquardt, 1963) for the face-face and the edge-edge configurations, a good match is achieved (the calibrated parameters are shown in Table 2). In the edge-edge configuration, although the height of the energy barrier in the U_{EB} and that in DLVO theory are the same, their positions are different. This is because, in the U_{EB}, as was also the case in the original GB potential function, the positions of the energy barrier and the energy well are uniquely determined regardless of particle configuration. Accordingly, for any configuration, the energy barrier exists at h_{eb} = 4.64 nm, and the energy well exists at h_{ew} = 0.0 nm. Both Bandera et al. (2024) and Nakamichi et al. (2024) present variants of this modelling framework that can capture the charge anisotropy associated with low pH (pH=4) environments.

Isotropic compression simulation

All simulations discussed in the following were performed using a modified version of the LAMMPS software (Thompson et al., 2022) in which U_{PR} and U_{EB} were implemented. The sensitivity of the predicted macro-scale response in compression to the choice of potential function was considered in isotropic compression and unloading simulations. The simulation using U_{EB} (see Eqs (6a) and (6b)) is denoted “S-EB”, and the simulation using U_{PR} (see Eq. (5)) is

407 denoted “S-PR”. The potential function parameters are presented in Table 2 (i.e. for pore water
408 with pH = 8 and salt concentration = 1 mM).
409
410 *Sample generation and initial pre-compression*
411 Mono-disperse assemblies of ellipsoids (2,000 nm in diameter and 200 nm in thickness) were
412 considered. The randomly orientated particles were initially arranged in a cubic simulation box
413 with 47 particles evenly spaced along each cartesian direction. The initial particle centre-to-centre
414 distance of 2,050 nm was sufficiently large so that there were no mechanical contacts. The initial
415 particle velocities were assigned to give a system temperature of 300 K, calculated from the
416 relationship between kinetic energy and temperature, i.e. $\frac{1}{2}M\bar{v}^2 = \frac{3}{2}k_{\mathrm{B}}T$, where M is the mass, $\bar{v}$
417 is the average velocity, k_{B} is the Boltzmann constant, and T is the temperature (here T=300 K).
418 There were 103,823 particles in the simulation box (47×47×47); Bandera et al. (2021) showed
419 that a system of 100,000 particles is sufficient to give an overall mechanical response which is
420 not sensitive to the system size. The use of periodic boundary conditions imposed in all three
421 Cartesian axis directions enabled the bulk material behaviour to be captured with a smaller
422 sample size than would be the case with rigid boundaries (e.g. Frenkel et al., 1997; Huang et al.,
423 2014). (Periodic boundary conditions are conditions under which the structure of the simulation
424 box repeats infinitely, which means that when a particle crosses the boundary of the simulation
425 box, it reappears on the other side with the same velocity (O’Sullivan, 2011; Thornton, 2000)).
426 The influence of gravity was ignored in the simulations.
427
428 The isotropic compression simulations had three phases: sample equilibration, pre-compression,
429 and compression; a simulation flow chart is given in Fig. 5. The sample equilibration phase
430 included NVE and NVT stages (adopting terminology common in the MD community). In an NVE
431 simulation, the number of particles (N), the volume of the virtual sample (V), and the total energy
432 in the sample (E) are constants of the simulation; this simulation enabled a check on energy
433 conservation. In the NVT simulation, N, V, and the kinetic temperature (T) of the virtual sample
434 are preserved; this stage was performed at a kinetic temperature of 300 K. After the NVT, a
435 second NVE was performed to confirm the energy equilibration of the virtual sample. Figures 6(a)
436 and 6(b) show the virtual CGMD simulation samples after the sample equilibration phase used in

S-EB and S-PR, respectively. At this stage the particle assembly can be considered a virtual slurry or suspension (with a void ratio of 19.6).

Compression was achieved via an NPT simulation in which N is constant and both the pressure (P) applied to the virtual sample and its temperature (T) are preserved/controlled. Bandera et al. (2021) discussed the need to consider strain rate in this type of simulation. Preliminary simulations showed that in the initial compression of the very low-density virtual samples, a very slow compression speed must be employed to maintain a constant temperature (here temperature is used to quantify the particles' average kinetic energy). Through a trial-and-error process, it was established that the best way to avoid high kinetic energies was to include a pre-compression phase, in which the target isotropic compression stress was p'=0.1 kPa.

During pre-compression, the samples changed from ideal slurry to a slightly consolidated state. Figure. 7 shows the variations of the void ratio (e) with the simulation time during pre-compression. The void ratio of $e = 19.6$ for both simulation samples (S-PR and S-EB) reflects the fact that the initial state was an ideal virtual suspension in which the particles were sufficiently disperse that they did not interact. The void ratios converged to the constant values of $e = 1.04$ for S-PR and $e = 1.21$ for S-EB at the end of pre-compression. This difference in the e values for the two samples reflects the difference in the particle interactions at large surface-to-surface distances. The gradient of the energy-separation ($U - h_{12}$) relationship at separation distances greater than h_{eb} is steeper for U_{EB} than for U_{PR}; this gradient determines the interaction force ($F = -\partial U/\partial h_{12}$ as noted above) and so the larger repulsive forces in the S-EB simulations led to a higher void ratio.

As shown in Figs 6(c) and 6(d), following pre-compression, both virtual samples had a microfabric in which face-face association dominated while there was not significant edge-face association. The colour of the particles in Fig. 6 indicates the rotation angle with respect to the x-z plane so that groups of particles with similar colours indicate domains. The simulations do not appear to exhibit the orthogonal particles or orthogonal domains of particles (these would manifest as a blue domain in close proximity to a red domain, for example) that would indicate an edge-face fabric.

Referring to Sides & Barden (1971), this observed microfabric can be classified to the turbostratic microfabric which is one of the dispersed microfabrics. This dispersed microfabric formation is consistent with the SEM images of kaolinite samples after sedimentation in alkaline water (Liu et al., 2015; Shabanian & Ouria, 2022; Wang & Siu, 2006a; Zhang et al., 2008). Figures 6(c) and 6(d) indicate that both domains (groups of particles which are approximately parallel) and stacks (groups of perfectly orientated platelets in face-face contact) form (using the terminology explained in Sides & Barden (1971) and Cotecchia & Chandler (1997)). Consequently, a heterogeneity in the microfabric has emerged from the simulations, even though the stress state is isotropic, and all particles have the same properties. However, a review of the surface-to-surface distance data at the end of pre-compression showed that almost all interactions were outside the energy barrier and not bonded each other, i.e. stable aggregates did not form.

Figure 8 shows that polar histograms of particle orientations in the x-z plane at the beginning (see Figs 8(a) and (b)) and the end (see Figs 8(c) and 8(d)) of pre-compression. Although particle orientations remain relatively isotropic during pre-compression, certain changes in particle orientations can be seen in both simulations (the polar histograms changed from a perfect semi-circle to a slightly distorted semi-circle). This means that particle rotations and particle rearrangements occurred during this phase.

Loading – Unloading – Reloading Simulations

The main compression phase included loading, unloading and reloading simulations. In the loading simulations, the mean effective stress p' increased from 0.1 kPa to 500 kPa. The unloading simulations started from five different p' values (100, 200, 300, 400, and 500 kPa), reducing p' to 10 kPa in each case. Hence, following the unloading simulations, each virtual sample had a different over-consolidation ratio. In the reloading simulation, p' was increased from 10 kPa to 500 kPa for the virtual sample in which previously p' had been reduced from 200 kPa to 10 kPa, i.e. the pre-consolidation stress was 200 kPa.

In the compression phase, a small timestep, $\Delta t=1.0\times10^{-10}$ s was used to meet the critical timestep condition (O'Sullivan, 2011) for numerical stability. Two compression speeds, 2.0×10^4 kPa/s for

497 the loading and reloading simulations and -2.0 × 10^5 kPa/s for the unloading simulation, were
498 used following Bandera et al. (2021) to maintain a quasi-static condition. In all simulations,
499 temperature and kinetic energy in the system remained constant, confirming that a quasi-static
500 state was achieved. While fully saturated kaolinite was simulated, pore-water was not directly
501 modelled and its flow was not considered, i.e. a fully drained compression is assumed.
502
503 Figures 9(a) and 9(b) show the results of the loading and unloading simulations in $e - log\, p'$
504 space for samples S-PR and S-EB respectively. Table 3 gives the compression indexes (C_c) and
505 swelling indexes (C_s). The additional subscripts in Table 3 indicate the interval of mean effective
506 stress over which they were calculated; for example, $C_{c,10-500}$ was calculated by linearly
507 interpolating between the data for p' = 10 kPa and p' = 500 kPa on the loading curve.
508
509 In the S-PR simulations (see Fig. 9(a)), which capture neither the energy barrier nor the energy
510 well in the potential function, the loading curve and the five unloading curves follow almost the
511 same path. The C_c and C_s values given in Table 3 for S-PR are very similar. Hence, the observed
512 response is almost completely elastic and reversible. It differs considerably from the physical
513 behaviour of kaolinite. The emergent compressive response in Fig. 9(a) differs from the data
514 presented in Bandera et al. (2021) because the Levenberg–Marquardt optimization approach
515 used here to calibrate the potential function parameters differs from the trial-and-error calibration
516 technique used in Bandera et al. 2021). In S-EB (see Fig. 9(b)), which considers both the energy
517 barrier and the energy well, the loading curve and five unloading curves are distinct. The C_s values
518 for the S-EB in Table 3 are consistently smaller than the corresponding C_c values, i.e. the stiffness
519 during unloading exceeded that during loading. This material response agrees with the
520 conventional understanding of the response of initially normally consolidated clay during loading
521 and unloading. Taken together the simulation results in Figs 9(a) and 9(b) confirm that the non-
522 monotonic particle interaction characterized by the energy barrier and the energy well contributes
523 to the irreversible behaviour of clay.
524
525 Available experimental data indicate slightly higher C_C values than obtained here, i.e. C_C=0.19-
526 0.30 (Hattab, 2011; Lambe & Whitman, 1969; Pedrotti & Tarantino, 2018; Wang & Siu, 2006a)

and similar C_s values to those obtained here for S-PR, i.e. C_s =0.03-0.08 (Hattab & Hicher, 2004; Pedrotti & Tarantino, 2018). Additional simulations in Nakamichi (2025) gave C_C similar values in 1-D compression. The DLVO parameters used were not tuned by a macro-scale calibration, and so the differences must be a consequence of the inherent model simplifications (all particles have the same surface energy and the same size). The C_c and C_s values reduced with increasing consolidation stress, i.e. the slope of the $e - \log p'$ curve reduces with increasing pressure and the compression curve has a slight upward concavity. While Di Maio et al. (2004) and Chong & Santamarina (2016) reported this phenomenon for some clay mineralogies, it is not apparent in the kaolinite data in Di Maio et al. (2004). The data in Pedrotti & Tarantino (2018) indicate a reducing C_c only when the pore fluid is acidic (i.e. pH=4); for their alkaline samples the $e - \log \sigma_v'$ curve is almost linear. Simulations in Nakamichi (2025) showed that this response geometry is insensitive to inter-particle friction or the assumed pH. It is known that the slope of the $e - \log p'$ relationship in sand increases when there is sand particle crushing (e.g. Cheng et al., 2003), and so it may be that a more advanced model capable of capturing particle crushing or domain crushing/compression is required to get a compression curve with a more realistic shape. What is noteworthy in the simulations is not the quantitative comparison with experimental data, but the ability of the materials to undergo irreversible volumetric compression and reproduce a situation where $C_s < C_C$.

Figure 10 presents histograms of the surface-to-surface distances between interacting particle pairs and their fitting curves obtained using the kernel density estimation (KDE) for S-PR. In the loading simulation (see Fig. 10(a)), the number of interactions that exist at around $h_{12} = 0$ increases as p' increases. Correspondingly, the maximum value of the KDE curve approaches $h_{12} = 0$ as p' increases. The distributions of the surface-to-surface distances are similar following all the simulations of unloading (see Fig. 10(b)). In each case, despite the different pre-consolidation stresses, the KDE curve attains a maximum value at $h_{12} \approx 49$ nm. This can be explained by the monotonic shape of the PR potential.

For the S-EB potential, Fig. 11(a) indicates that as p' increases during the loading simulation, the number of interactions with $h_{12} < h_{\mathrm{eb}}$, i.e. the number of interactions that are inside the energy

557 barrier, increases. At the end of the unloading simulations (see Fig. 11(b)), while the maximum
558 value of the KDE curve shift occurs at a larger h_{12} value than was the case before unloading, the
559 number of interactions that have exceeded the energy barrier does not significantly change. The
560 particle pairs that overcame the energy barrier during the loading simulation were effectively
561 physically bonded or trapped in an attractive interaction that persisted during unloading. These
562 interactions remain stuck in the energy well throughout unloading as the energy barrier cannot be
563 overcome. This particle-scale response explains the irreversible mechanical response between
564 during the loading and unloading simulations.
565
566 Figures 5(c) to 5(f) and Figs. 8(c) to 8(f) show for both S-PR and S-EB that particle orientations
567 did not change significantly during initial loading. This is consistent with the experimental
568 observations of kaolinite sample prepared with alkaline pore water (Pedrotti & Tarantino, 2018;
569 Wang & Siu, 2006a).
570
571 As detailed above, evidence gained via SEM imaging indicates that formation of stacks of
572 platelets is important for the mechanical behaviour of clay during consolidation. A stack is defined
573 as a band of groups of particles at face-face contact, hence, it is important to identify face-face
574 contacts. Referring to Ebrahimi et al. (2014) and Bandera et al. (2021), face-face contact was
575 defined here using the following two geometrical criteria (i) the surface-to-surface distance is less
576 than the energy barrier position (i.e. $h_{12} < h_{eb}$) and (ii) the absolute value of dot product of the
577 normal vectors of the two particles is greater than 0.95. These criteria were applied to S-EB and
578 S-PR assuming that the energy barrier position was the same although the PR potential does not
579 have the energy barrier (i.e. $h_{eb} = 4.61$ nm was used for both S-PR and S-EB). Figure 12 gives
580 the face-face contact coordination number which is the total number of face-face contacts divided
581 by twice the number of particles in the simulation box. During initial loading, both simulations show
582 the same trend: as the mean effective stress increases, the face-face coordination number
583 increases. This means that many particles form new stacks or join existing stacks as the external
584 pressure increases. During unloading in S-PR the face-face coordination number decreases
585 through the same pathway as the initial loading when the mean effective stress is released. In
586 other words, the stack is not maintained and falls apart again during unloading. On the other hand,

in S-EB, the face-face coordination number does not decrease during unloading although the mean effective stress decreases, which means that stacks are maintained. One might expect more stacks to form in 1-D compression rather than in the isotropic compression scenario considered here.

Reloading simulation

As expected, preliminary reloading for S-PR simulations showed almost the same response as that of its loading simulation. Hence, only the reloading simulation results for the S-EB simulations are presented in Fig. 13; these data are for the S-EB virtual sample that had previously been unloaded from 200 kPa to 10 kPa. During reloading, the sample was isotropically loaded from 10 kPa to 500 kPa so that at the start of loading, its pre-consolidation pressure, p'_c was 200 kPa. Data for the loading simulation (from 0.1 kPa to 500 kPa) and the unloading simulation (from 200 kPa to 10 kPa) are also presented on Fig. 13. As long as p' remained smaller than the pre-consolidation stress (i.e. $p' < p'_c$), the reloading and unloading simulation curves completely overlapped, indicating an elastic and reversible mechanical response. In physical clay samples hysteresis may be evident (e.g. Burland, 1990); the lack of hysteresis here is likely a consequence of the sample homogeneity and the absence of a dissipating parameter such a friction. However, once $p' > p'_c$, the reloading simulation curve follows the same path as the loading simulation curve. This mechanical response of the virtual sample upon the reloading simulation is very similar to the consolidation behaviour that an over-consolidated clay sample exhibits before and after pre-consolidation stress in a laboratory consolidation test. This difference in the observed mechanical response during loading and reloading indicates a stress-history dependence that is a key feature of clay behaviour. Data on Fig. 14 show that the number of interactions exceeding the energy barrier, N_{eb} (see Fig. 14(a)), and the proportion of interactions, N_{eb}/N_t (see Fig. 14(b)) (N_t is the total number of interactions) increases with increasing p' during loading, while, during unloading, N_{eb} remains almost constant, reflecting the interactions that became stuck in the energy well, as explained above. During reloading, while $p' < p'_c$ (i.e. so long as the sample remains over-consolidated), N_{eb} remains almost constant, which indicates that the energy provided by the applied stress is insufficient to generate new interactions that overcome the energy barrier. However, once $p' > p'_c$ (i.e. the sample can be considered normally consolidated),

N_{eb} increases with increasing p' as the applied stress to the virtual sample is sufficient to generate new interactions/transform existing interactions to overcome the energy barrier.

Influence of height of energy barrier

Based upon the data presented above, it can be expected that a kaolinite sample with particle interactions that have a lower energy barrier height (U_{eb}^{max}) will exhibit more distinct behaviours in loading and unloading as more particles will cross the energy barrier. It is also important to include a parametric study on energy barrier height given the known limitations of the DLVO framework adopted here. To explore the sensitivity to the energy barrier height, isotropic compression simulations were performed using the EB potential functions with U_{eb}^{max} values that were 50% and 25% of the U_{eb}^{max} predicted from DLVO theory, as shown in Fig. 15. The depths of the energy wells (U_{ew}^{min}) also differed from the original EB potential function. These simulations are parametric studies to examine the influence of the height of the energy barrier, hence, no specific salt concentration was assumed although pH=8 was assumed. However, in a physical experiment, lower energy barriers could be achieved by reducing the electrostatic repulsive force by increasing salt concentration (see Fig. 2) (Masliyah & Bhattacharjee, 2005). Here the U_{eb}^{max} values were adjusted by changing the energy scale parameters, A, B and C that were 50%, and 25% of the original values shown in Table 2. The remaining parameters adopted are given in Table 2. These simulations were conducted by following the loading and unloading protocol for S-EB simulations with a maximum p' of 100 kPa in loading simulation and subsequent unloading 100 kPa to 10 kPa.

Figure 16 shows the $e - log\ p'$ relationship for virtual samples with different energy barrier heights, and Table 4 shows the compression and swelling Indexes (i.e. C_c and C_s) calculated by linear interpolation between p' = 10 kPa and p' =100 kPa. During loading, a higher U_{eb}^{max} gives a larger C_c. This may be explained by the fact that the initial e increases with increasing U_{eb}^{max} (see Fig. 16). The virtual sample with a higher U_{eb}^{max} also has a larger C_s, which means that the virtual sample with a higher U_{eb}^{max} shows a larger volumetric change (rebound behaviour) upon unloading. The data on Table 4 show that C_s/C_c increases with increasing U_{eb}^{max}; a lower C_s/C_c means a larger difference in the mechanical response considering loading and unloading.

646

647 The histograms of h_{12} at p' = 100 kPa (end of loading) presented in Fig. 17 show that the number
648 of interactions exceeding the energy barrier increases with reducing $U_{\mathrm{eb}}^{\max}$; because as $U_{\mathrm{eb}}^{\max}$;
649 reduces, the energy barrier can be exceeded with less energy/less applied compressive stress.
650 As explained before, the number of the particle interactions that overcome the energy barrier is
651 directly related to the mechanical response of clay. Hence, the different mechanical responses
652 exhibited by the virtual samples with energy barrier heights were likely caused by different
653 numbers of interactions overcoming the energy barrier.

654

655 **Conclusions**

656 This contribution has used coarse-grained molecular dynamics (CGMD) of systems of more than
657 100,000 particles to explore the relationship between the particle interactions and the overall
658 mechanical response of kaolinite. The simulations assumed a specific pore water condition with
659 pH=8 (alkaline) and a salt (KCl) concentration=1 mM and that DLVO theory can give a reasonable
660 model of kaolinite particle interactions.

661

662 The following conclusions can be drawn from the study:

663 1. The Gay-Berne potential function can be taken as a basis to develop potential functions
664 to simulate kaolinite particles in CGMD simulations. Addition or removal of terms allows
665 features including the energy barrier, the energy well and Born repulsion to be simulated
666 as well as an exploration of the sensitivity of the macro-scale response to assumptions
667 about the clay particle interactions. Invoking the Levenberg–Marquardt (mini-max)
668 algorithm can enable calibration of the potential functions to obtain a reasonably close
669 match to interactions predicted using the DLVO theory. This modelling approach can be
670 further extended to consider more complex scenarios (e.g. multiple energy
671 barriers/energy wells).
672 2. As clay particles approach each other, the potential energy of their interaction increases,
673 creating a repulsive force between them until they reach an energy barrier. Simulations
674 that captured both the energy barrier and energy well indicated that for stress levels of
675 interest in geotechnical engineering the applied pressure can generate enough

interparticle energy/force at the particle scale to overcome this energy barrier, the interaction becomes strongly attractive and clay particles are physically bonded together. Therefore, they remain bonded when the compressive pressure is reduced, although a loading scenario that generates inter-particle tensile or shear forces may disaggregate them. The presence of these bonded particles contributes to the dramatic and irreversible changes in the mechanical response of a clay sample, resulting in the experimentally observed differences in stiffness between normally- and over-consolidated clays.

3. While the model developed here is linked to DLVO theory and only one clay mineral was considered, numerous other data available in the literature also indicate a non-monotonic energy-separation relationship with sometimes with multiple energy barriers and energy wells. Consequently, despite the ideal nature of the model presented here and consideration of only one mineralogy, the findings and research approach are likely to be transferrable to other clay mineralogies and other pore water chemistries.

Limitations of this study contribution which may provide ideas for future research include the following:

1. While the influence of the height of the energy barrier was considered here, the study did not fully explore the sensitivity of microfabric formation or macroscale mechanical behaviour to pore water chemistry. It is possible to have clay particle interactions without an energy barrier, the energy well can be a weak repulsion rather than an attraction, or the presence of an energy barrier may depend on the orientation of the particles. If the energy barrier disappears completely, the hypothesis put forward here is not applicable. In these cases, the mechanisms of particle rotation and particle rearrangement revealed in the SEM images are likely the key contributors to the irreversible compressive behaviour of clay.
2. The current model presented here has looked only at isotropic compression. Additional simulations and analyses are required to examine the possibility for the bonds formed to be broken in shear deformation as might be applied in a mechanical remoulding.
3. The current model has a number of idealizations (e.g. uniform surface properties, mono-disperse particle sizes, geometrical idealization, and a relatively simple interaction model).

706 Further development of the model is needed to give more realistic C_c values that
707 increases with increasing pressure, hysteresis in unloading/reloading, etc. However,
708 despite the simplicity of the model the data presented here provide some novel insight
709 that should ultimately lead to models of clay macro-behaviour that are informed by micro-
710 mechanics.
711

712 **Acknowledgements**

713 The first author was supported by OBAYASHI Corporation and Imperial College Dixon
714 Scholarship. Sara Bandera's doctoral research was funded by the Leverhulme Trust, (Project no.
715 RPG-2017-055). Simulations were carried out using the High-Performance Computer (HPC)
716 facilities at Imperial College London and University College London. We are grateful to the UK
717 Materials and Molecular Modelling Hub for computational resources, which is partially funded by
718 EPSRC (EP/T022213/1, EP/W032260/1 and EP/P020194/1).
719

720 **References**

721 Ajmera, B., & Tiwari, B. (2014). Effects of saline fluid on compressibility of clay minerals.
722 *Environmental Geotechnics*, *1*(2). https://doi.org/10.1680/envgeo.13.00053
723 Aminpour, P., & Sjoblom, K. J. (2019). Multi-scale modelling of kaolinite triaxial behaviour.
724 *Géotechnique Letters*, *9*(3), 178–185. https://doi.org/10.1680/jgele.18.00194
725 Anandarajah, A. (1994). Discrete-element method for simulating behavior of cohesive soil.
726 *Journal of Geotechnical Engineering*, *120*(9). https://doi.org/10.1061/(ASCE)0733-
727 9410(1994)120:9(1593)
728 Anandarajah, A. (2000a). Numerical simulation of one-dimensional behaviour of a
729 kaolinite. *Géotechnique*, *50*(5), 509–519.
730 https://doi.org/https://doi.org/10.1680/geot.2000.50.5.509
731 Anandarajah, A. (2000b). On influence of fabric anisotropy on the stress-strain behavior of
732 clays. *Computers and Geotechnics*, *27*(1). https://doi.org/10.1016/S0266-
733 352X(00)00005-7
734 Angioletti-Uberti, S. (2017). Theory, simulations and the design of functionalized
735 nanoparticles for biomedical applications: A Soft Matter Perspective. In *npj*
736 *Computational Materials* (Vol. 3, Issue 1). https://doi.org/10.1038/s41524-017-0050-y
737 Bandera, S. (2022). *Fundamental analysis of the influence of structure on clay behaviour*.
738 PhD thesis. Imperial College London.
739 Bandera, S., O'Sullivan, C., Tangney, P., & Angioletti-Uberti, S. (2021). Coarse-grained
740 molecular dynamics simulations of clay compression. *Computers and Geotechnics*,
741 *138*. https://doi.org/10.1016/j.compgeo.2021.104333
742 Bandera, S., O'Sullivan, C., Tangney, P., & Angioletti-Uberti, S. (2024). Composite
743 ellipsoids to model charge anisotropy in particle-scale simulations of kaolinite.
744 *Géotechnique Letters*, *14*(2), 27–34. https://doi.org/10.1680/jgele.23.00085
745 Boulet, P., Coveney, P. V., & Stackhouse, S. (2004). Simulation of hydrated Li+-, Na+- and
746 K +-montmorillonite/polymer nanocomposites using large-scale molecular dynamics.
747 *Chemical Physics Letters*, *389*(4–6). https://doi.org/10.1016/j.cplett.2004.03.084

748 Braggs, B., Fornasiero, D., Ralston, J., & St. Smart, R. (1994). The effect of surface
749 modification by an organosilane on the electrochemical properties of kaolinite. *Clays*
750 *and Clay Minerals*, *42*(2). https://doi.org/10.1346/CCMN.1994.0420203
751 Burland, J. B. (1990). On the compressibility and shear strength of natural clays.
752 *Geotechnique*, *40*(3). https://doi.org/10.1680/geot.1990.40.3.329
753 Butt, H., Graf, K. and Kappl, M. (2003), Physics and Chemistry of Interfaces, John Wiley &
754 Sons, Ltd.
755 Carrier, B. (2013). *Influence of water on the short-term and long-term mechanical*
756 *properties of swelling clays: experiments on self-supporting films and molecular*
757 *simulations*. PhD Thesis. Université Paris-Est. https://pastel.archives-
758 ouvertes.fr/pastel-00960833/document
759 Casarella, A., Tarantino, A., & di Donna, A. (2024). Revisiting DLVO theory to inform
760 particle-scale modelling of clays. *Computers and Geotechnics*, *165*.
761 Cheng, Y. P., Nakata, Y., & Bolton, M. D. (2003). Discrete element simulation of crushable
762 soil. *Geotechnique*, *53*(7). https://doi.org/10.1680/geot.2003.53.7.633
763 Chong, S.H., & Santamarina, J. C. (2016). Soil Compressibility Models for a Wide Stress
764 Range. *Journal of Geotechnical and Geoenvironmental Engineering*, *142*(6).
765 https://doi.org/10.1061/(asce)gt.1943-5606.0001482
766 Collins, K., & McGown, A. (1974). The Form and Function of Microfabric Features in a
767 Variety of Natural Soils. *Geotechnique*, *24*(2).
768 https://doi.org/10.1680/geot.1974.24.2.223
769 Cotecchia, F., & Chandler, R. J. (1997). The influence of structure on the pre-failure
770 behaviour of a natural clay. *Geotechnique*, *47*(3).
771 https://doi.org/10.1680/geot.1997.47.3.523
772 de Bono, J. P., & McDowell, G. (2023a). Simulating multifaceted interactions between
773 kaolinite platelets. *Powder Technology*, *413*.
774 https://doi.org/10.1016/j.powtec.2022.118062
775 de Bono, J. P., & McDowell, G. R. (2022a). Discrete element modelling of normal
776 compression of clay. *Journal of the Mechanics and Physics of Solids*, *162*.
777 https://doi.org/10.1016/j.jmps.2022.104847

de Bono, J. P., & McDowell, G. R. (2022b). Some important aspects of modelling clay platelet interactions using DEM. *Powder Technology*, *398*. https://doi.org/10.1016/j.powtec.2021.117056

de Bono, J. P., & McDowell, G. R. (2023b). Particle-scale simulations of the compression and shearing of kaolin clay. *Geotechnique*. https://doi.org/10.1680/jgeot.22.00423

Derjaguin, B. (1934). Untersuchungen über die Reibung und Adhäsion, IV - Theorie des Anhaftens kleiner Teilchen. *Kolloid-Zeitschrift*, *69*(2). https://doi.org/10.1007/BF01433225

Derjaguin, B., & Landau, L. (1941). Theory of the Stability of Strongly Charged Lyophobic Sols and of the Adhesion of Strongly Charged Particles in Solutions of Electrolytes. *Progress in Surface Science*, *Volume 43*(Issues 1–4), 30–59. https://doi.org/https://doi.org/10.1016/0079-6816(93)90013-L

Di Maio, C. (1996). Exposure of bentonite to salt solution: Osmotic and mechanical effects. *Geotechnique*, *46*(4). https://doi.org/10.1680/geot.1996.46.4.695

Di Maio, C., Santoli, L., & Schiavone, P. (2004). Volume change behaviour of clays: The influence of mineral composition, pore fluid composition and stress state. *Mechanics of Materials*, *36*(5–6). https://doi.org/10.1016/S0167-6636(03)00070-X

Ducker, W. A., Senden, T. J., & Pashley, R. M. (1991). Direct measurement of colloidal forces using an atomic force microscope. *Nature*, *353*(6341). https://doi.org/10.1038/353239a0

Ducker, W. A., Senden, T. J., & Pashley, R. M. (1992). Measurement of Forces in Liquids Using a Force Microscope. *Langmuir*, *8*(7). https://doi.org/10.1021/la00043a024

Ebrahimi, D., Whittle, A. J., & Pellenq, R. J.-M. (2014). Mesoscale properties of clay aggregates from potential of mean force representation of interactions between nanoplatelets. *The Journal of Chemical Physics*, *140*(15), 154309. https://doi.org/10.1063/1.4870932

Everaers, R., & Ejtehadi, M. R. (2003). Interaction potentials for soft and hard ellipsoids. *Physical Review E - Statistical Physics, Plasmas, Fluids, and Related Interdisciplinary Topics*, *67*(4). https://doi.org/10.1103/PhysRevE.67.041710

807 Frenkel, D., Smit, B., Tobochnik, J., McKay, S. R., & Christian, W. (1997). Understanding
808 Molecular Simulation. *Computers in Physics*, *11*(4).
809 https://doi.org/10.1063/1.4822570
810 Gay, J. G., & Berne, B. J. (1981). Modification of the overlap potential to mimic a linear
811 site-site potential. *The Journal of Chemical Physics*, *74*(6).
812 https://doi.org/10.1063/1.441483
813 Gens, A. (2010). Soil-environment interactions in geotechnical engineering. *Geotechnique*,
814 *60*(1). https://doi.org/10.1680/geot.9.P.109
815 Goehring, L., Clegg, W. J., & Routh, A. F. (2010). Solidification and ordering during
816 directional drying of a colloidal dispersion. *Langmuir*, *26*(12).
817 https://doi.org/10.1021/la100125v
818 Guglielmi, S., Cotecchia, F., Cafaro, F., & Gens, A. (2024). Analysis of the micro to macro
819 response of clays to compression. *Géotechnique*, *74*(2), 134–154.
820 https://doi.org/10.1680/jgeot.21.00233
821 Guo, Y., & Yu, X. (2023). Insight on bulk shear strength parameters of clay using discrete
822 element approach incorporating physics-based interparticle force model. *Soils and*
823 *Foundations*, *63*(1). https://doi.org/10.1016/j.sandf.2022.101250
824 Gupta, V. (2011). *Surface Charge Features of Kaolinite Particles and Their Interactions*.
825 PhD thesis. University of Utah.
826 Gupta, V., Hampton, M. A., Stokes, J. R., Nguyen, A. V., & Miller, J. D. (2011). Particle
827 interactions in kaolinite suspensions and corresponding aggregate structures.
828 *Journal of Colloid and Interface Science*, *359*(1), 95–103.
829 https://doi.org/10.1016/j.jcis.2011.03.043
830 Gupta, V., & Miller, J. D. (2010). Surface force measurements at the basal planes of
831 ordered kaolinite particles. *Journal of Colloid and Interface Science*, *344*(2), 362–
832 371. https://doi.org/10.1016/j.jcis.2010.01.012
833 Güven, N. (1992). Molecular Aspects of Clay-Water Interactions. In *Clay-Water Interface*
834 *and its Rheological Implications* (pp. 1–79). Clay Minerals Society.
835 https://doi.org/10.1346/CMS-WLS-4.1

Hattab, M. (2011). Critical state notion and microstructural considerations in clays. *Comptes Rendus - Mecanique*, *339*(11). https://doi.org/10.1016/j.crme.2011.07.007

Hattab, M., & Fleureau, J. M. (2010). Experimental study of kaolin particle orientation mechanism. *Geotechnique*, *60*(5). https://doi.org/10.1680/geot.2010.60.5.323

Hattab, M., & Hicher, P. Y. (2004). Dilating behaviour of overconsolidated clay. *Soils and Foundations*, *44*(4). https://doi.org/10.3208/sandf.44.4_27

Herrington, T. M., Clarke, A. Q., & Watts, J. C. (1992). The surface charge of kaolin. *Colloids and Surfaces*, *68*(3). https://doi.org/10.1016/0166-6622(92)80200-L

Honorio, T., Brochard, L., & Vandamme, M. (2017). Hydration Phase Diagram of Clay Particles from Molecular Simulations. *Langmuir*, *33*(44). https://doi.org/10.1021/acs.langmuir.7b03198

Huang, X., Hanley, K. J., O'Sullivan, C., & Kwok, F. C. Y. (2014). Effect of sample size on the response of DEM samples with a realistic grading. *Particuology*, *15*. https://doi.org/10.1016/j.partic.2013.07.006

Israelachvili, J. N. (2011). Intermolecular and Surface Forces: Third Edition. In *Intermolecular and Surface Forces: Third Edition*. https://doi.org/10.1016/C2011-0-05119-0

Jaradat, K. A., & Abdelaziz, S. L. (2019). On the use of discrete element method for multi-scale assessment of clay behavior. In *Computers and Geotechnics* (Vol. 112). https://doi.org/10.1016/j.compgeo.2019.05.001

Jing, Z., Liu, C., Cheng, S. Y., Qi, R., Walker, B. D., Piquemal, J. P., & Ren, P. (2019). Polarizable Force Fields for Biomolecular Simulations: Recent Advances and Applications. In *Annual Review of Biophysics* (Vol. 48). https://doi.org/10.1146/annurev-biophys-070317-033349

Kumar, N. (2017). *Surface charge characterisation of solid-liquid interfaces using atomic force microscopy*. The University of Twente.

Lambe, T. W., & Whitman, R. V. (1969). *Soil mechanics*. Wiley. https://archive.org/details/soilmechanics00lamb/mode/2up

Levenberg, K. (1944). A method for the solution of certain non-linear problems in least squares. *Quarterly of Applied Mathematics*, *2*(2). https://doi.org/10.1090/qam/10666

Liu, J. (2015). *Surface properties of kaolinite particles - their interactions and flotation considerations*. PhD thesis. University of Utah

Liu, J., Lin, C. L., & Miller, J. D. (2015). Simulation of cluster formation from kaolinite suspensions. *International Journal of Mineral Processing*, *145*, 38–47. https://doi.org/10.1016/j.minpro.2015.07.004

Luo, J., Liu, M., Xing, Y., Gui, X., & Li, J. (2022). Investigating agglomeration of kaolinite particles in the presence of dodecylamine by force testing and molecular dynamics simulation. *Colloids and Surfaces A: Physicochemical and Engineering Aspects*, *645*. https://doi.org/10.1016/j.colsurfa.2022.128930

Marquardt, D. W. (1963). An Algorithm for Least-Squares Estimation of Nonlinear Parameters. Journal of the Society for Industrial and Applied Mathematics. *Quarterly of Applied Mathematics*, *11*(2).

Masliyah, J. H., & Bhattacharjee, S. (2005). Electrokinetic and Colloid Transport Phenomena. In *Electrokinetic and Colloid Transport Phenomena*. https://doi.org/10.1002/0471799742

Mitchell, J. K., & Soga, K. (2005). Fundamentals of Soil Behavior. 3rd Edition. In *Angewandte Chemie International Edition, 6(11), 951–952.*

Nakamichi, Y. (2025). *Particle-scale simulations of clay using molecular dynamics*. PhD thesis. Imperial College London.

Nakamichi, Y., O'Sullivan, C., Angioletti-Uberti, S., Tangney, P., & Bandera, S. (2023). Isotropic compression simulation of kaolinite using coarse-grained molecular dynamics. *8th International Symposium on Deformation Characteristics of Geomaterials (IS-Porto 2023)*. https://doi.org/https://doi.org/10.1051/e3sconf/202454407006

Nakamichi, Y., O'Sullivan, C., Tangney, P., & Angioletti-Uberti, S. (2024). Modelling anisotropic surface charge of kaolinite particles depending on pore water pH. *Computers and Geotechnics*, *173*, 106505. https://doi.org/https://doi.org/10.1016/j.compgeo.2024.106505

Nguyen, A., & Schulze, H. J. (2003). Colloidal Science of Flotation. In *Colloidal Science of Flotation*. https://doi.org/10.1201/9781482276411

Niu, M. Y., & Jiang, M. J. (2023). DEM modeling mechanical behaviors of remolded and structured clays under constant stress ratio compression tests. In *Smart Geotechnics for Smart Societies*. https://doi.org/10.1201/9781003299127-40

O'Sullivan, C. (2011). Particulate Discrete Element Modelling: A Geomechanics Perspective. In *Particulate Discrete Element Modelling: A Geomechanics Perspective*. https://doi.org/10.1201/9781482266498

Pagano, A. G., Magnanimo, V., Weinhart, T., & Tarantino, A. (2020). Exploring the micromechanics of non-active clays by way of virtual DEM experiments. *Géotechnique*, *70*(4). https://doi.org/10.1680/jgeot.18.P.060

Palomino, A. M., & Santamarina, J. C. (2005). Fabric map for kaolinite: Effects of pH and ionic concentration on behavior. *Clays and Clay Minerals*, *53*(3). https://doi.org/10.1346/CCMN.2005.0530302

Pedrotti, M., & Tarantino, A. (2018). An experimental investigation into the micromechanics of non-active clays. *Géotechnique*, *68*(8), 666–683. https://doi.org/10.1680/jgeot.16.P.245

Potyondy, D. O., & Cundall, P. A. (2004). A bonded-particle model for rock. *International Journal of Rock Mechanics and Mining Sciences*, *41*(8 SPEC.ISS.). https://doi.org/10.1016/j.ijrmms.2004.09.011

Shabanian, M., & Ouria, A. (2022). Effect of the steady-state pH of kaolinite pore fluid on its microstructure and geotechnical properties. *Arabian Journal of Geosciences*, *15*(17). https://doi.org/10.1007/s12517-022-10689-z

Sides, G., & Barden, L. (1971). Microstructure of dispersed and flocculated samples of kaolinite, illite, and montmorillonite. *Canadian Geotechnical Journal*, *8*(3). https://doi.org/10.1139/t71-041

Sjoblom, K. J. (2016). Coarse-Grained Molecular Dynamics Approach to Simulating Clay Behavior. *Journal of Geotechnical and Geoenvironmental Engineering*, *142*(2). https://doi.org/10.1061/(asce)gt.1943-5606.0001394

Tangney, P., & Scandolo, S. (2002). An ab initio parametrized interatomic force field for silica. *Journal of Chemical Physics*, *117*(19). https://doi.org/10.1063/1.1513312

925 Thompson, A. P., Aktulga, H. M., Berger, R., Bolintineanu, D. S., Brown, W. M., Crozier, P.
926 S., in 't Veld, P. J., Kohlmeyer, A., Moore, S. G., Nguyen, T. D., Shan, R., Stevens,
927 M. J., Tranchida, J., Trott, C., & Plimpton, S. J. (2022). LAMMPS - a flexible
928 simulation tool for particle-based materials modeling at the atomic, meso, and
929 continuum scales. *Computer Physics Communications*, *271*.
930 https://doi.org/10.1016/j.cpc.2021.108171
931 Thornton, C. (2000). Numerical simulations of deviatoric shear deformation of granular
932 media. *Geotechnique*, *50*(1). https://doi.org/10.1680/geot.2000.50.1.43
933 Trefalt, G. (2016). Derivation of the inverse Schulze-Hardy rule. *Physical Review E*, *93*(3).
934 https://doi.org/10.1103/PhysRevE.93.032612
935 Trefalt, G., Szilágyi, I., & Borkovec, M. (2020). Schulze-Hardy rule revisited. *Colloid and*
936 *Polymer Science*, *298*(8). https://doi.org/10.1007/s00396-020-04665-w
937 Verwey, E. J. W., & Overbeek, J. T. G. (1948). Theory of the Stability of Lyophobic
938 Colloids. *The Journal of Physical and Colloid Chemistry*, *51*(3), 631–636.
939 https://doi.org/10.1021/j150453a001
940 Volkova, E., Narayanan Nair, A. K., Engelbrecht, J., Schwingenschlögl, U., Sun, S., &
941 Stenchikov, G. (2021). Molecular Dynamics Modeling of Kaolinite Particle
942 Associations. *Journal of Physical Chemistry C*, *125*(43).
943 https://doi.org/10.1021/acs.jpcc.1c06598
944 Wang, Y. H., & Siu, W. K. (2006a). Structure characteristics and mechanical properties of
945 kaolinite soils. II. Effects of structure on mechanical properties. *Canadian*
946 *Geotechnical Journal*, *43*(6), 601–617. https://doi.org/10.1139/T06-027
947 Wang, Y. H., & Siu, W. K. (2006b). Structure characteristics and mechanical properties of
948 kaolinite soils. I. Surface charges and structural characterizations. *Canadian*
949 *Geotechnical Journal*, *43*(6), 587–600. https://doi.org/10.1139/T06-026
950 Wernersson, E., & Jungwirth, P. (2010). Effect of water polarizability on the properties of
951 solutions of polyvalent ions: Simulations of aqueous sodium sulfate with different
952 force fields. *Journal of Chemical Theory and Computation*, *6*(10).
953 https://doi.org/10.1021/ct100465g

954 Won, J., & Burns, S. E. (2023). Role of ionic concentration in the kinetic attachment of
955 kaolinite and sand. *Canadian Geotechnical Journal*, *60*(2).
956 https://doi.org/10.1139/cgj-2021-0682
957 Yao, M. (2001). *Three-dimensional discrete element method analysis of cohesive soil*.
958 PhD thesis. Johns Hopkins University.
959 Yao, M., & Anandarajah, A. (2003). Three-Dimensional Discrete Element Method of
960 Analysis of Clays. *Journal of Engineering Mechanics*, *129*(6), 585–596.
961 https://doi.org/https://doi.org/10.1061/(ASCE)0733-9399(2003)129:6(585)
962 Zen, A., Bui, T., Bao Le, T. T., Tay, W. J., Chellappah, K., Collins, I. R., Rickman, R. D.,
963 Striolo, A., & Michaelides, A. (2022). Long-Range Ionic and Short-Range Hydration
964 Effects Govern Strongly Anisotropic Clay Nanoparticle Interactions. *Journal of*
965 *Physical Chemistry C*. https://doi.org/10.1021/acs.jpcc.2c01306
966 Zhang, X. P., Hu, Y. H., & Liu, R. Q. (2008). Hydrophobic aggregation of ultrafine kaolinite.
967 *Journal of Central South University of Technology (English Edition)*, *15*(3).
968 https://doi.org/10.1007/s11771-008-0069-9
969 Zheng, Y., Baudet, B. A., Delage, P., Pereira, J. M., & Sammonds, P. (2022). Pore
970 changes in an illitic clay during one-dimensional compression. *Geotechnique*, *73*(10).
971 https://doi.org/10.1680/jgeot.21.00206
972 Zhu, H., Whittle, A. J., & Pellenq, R. J. M. (2022). Potential of Mean Force for Face-Face
973 Interactions between Pairs of 2:1 Clay Mineral Platelets. *Langmuir*, *38*(43).
974 https://doi.org/10.1021/acs.langmuir.2c01632
975
976

977 **Appendix**

978

979 This appendix details the calculation of h_{12}, χ_{12} and η_{12}.

$$h_{12} = r_{12} - \sigma_{12} \tag{A.1}$$

980 And

$$\sigma_{12} = \left[\frac{1}{2}\hat{\mathbf{r}}_{12}^{T}\mathbf{G}_{12}^{T}\hat{\mathbf{r}}_{12}\right]^{-1/2} \tag{A.2}$$

981 where h_{12} is the surface-to-surface distance between two ellipsoids, r_{12} is the centre-to-centre
982 distance between two ellipsoids and $\hat{\mathbf{r}}_{12}$ is the unit vector of $\mathbf{r}_{12}$ which is the centre-to-centre
983 vector between two ellipsoids. $\mathbf{G}_{12}$ is expressed using the transformation matrix from simulation
984 box frame to body frame, $\mathbf{A}_i$ and the shape matrices, $\mathbf{S}_i$, given by each radius of the ellipsoid *i*,
985 i.e. $\mathbf{S}_i = diag(a_i, b_i, c_i)$.

$$\mathbf{G}_{12} = \mathbf{A}_1^T\mathbf{S}_1\mathbf{A}_1 + \mathbf{A}_2^T\boldsymbol{S}_2\mathbf{A}_2 = \mathbf{G}_2 + \mathbf{G}_1 \tag{A.3}$$

986 η_{12} in Eq. (4) is a parameter related to shape anisotropy that depends on the relative orientation
987 of the two ellipsoids and given by:

$$\eta_{12} = \left[\frac{2s_1s_2}{\det(\mathbf{G}_{12})}\right]^{\upsilon/2} \tag{A.4}$$

988 And

$$s_i = [a_ib_i + c_ic_i\,][a_ib_i]^{1/2} \tag{A.5}$$

989 where υ is a user-specified parameter, usually υ =1.

990

991 χ_{12} is a parameter related to energy anisotropy based on the depth of the energy well and is
992 given by:

$$\chi_{12} = [2\hat{\mathbf{r}}_{12}^{T}\mathbf{B}_{12}^{-1}\hat{\mathbf{r}}_{12}]^{\mu} \tag{A.6}$$

993 And

$$\mathbf{B}_{12} = \mathbf{A}_1^T\mathbf{U}_1\mathbf{A}_1 + \mathbf{A}_2^T\mathbf{U}_2\mathbf{A}_2 = \mathbf{B}_2 + \mathbf{B}_1 \tag{A.7}$$

994

995 where $\mathbf{U}_i = diag(\epsilon_{ia}, \epsilon_{ib}, \epsilon_{ic})$ is the energy matrix which is defined by determining $\epsilon_{ia}, \epsilon_{ib}, \epsilon_{ic}$
996 based on the depth of the energy well in the face-face and edge-edge configurations. μ is the
997 user-specified parameter, usually μ =2.

998 **Figure captions**

999

1000 Figure 1. Idealised interaction between two kaolinite particles (a) interaction energy and (b)
1001 interaction force adopted by Lu et al. (2008).
1002 Figure 2. Schematic diagram of interaction energy-separation distance profile for double-layer
1003 repulsion, van der Waals attraction, and net DLVO energy (modified from Israelachvili, 2011;
1004 Masliyah & Bhattacharjee, 2005).
1005 Figure 3. Calibrated PR (purely repulsive) potential (U_{PR}) compared with DLVO-generated data
1006 for face-face and edge-edge configurations for ellipsoids 2,000 nm in diameter and 200 nm thick.
1007 Figure 4. Calibrated EB (energy barrier) potential (U_{EB}) compared with DLVO-generated data for
1008 face-face and edge-edge configurations for ellipsoids 2,000 nm in diameter and 200 nm thick.
1009 Figure 5. Workflow of isotropic compression simulation.
1010 Figure 6. Illustrations of virtual samples (103,823 particles). Left hand column gives images from
1011 simulations using the purely repulsive potential function, U_{PR}, while the right hand column gives
1012 images simulations using the energy barrier potential function, U_{EB}: (a) and (b) illustrate the initial
1013 configuration before the pre-compression phase ($p' = 0.1$ kPa), (c) and (d) illustrate the virtual
1014 samples after the pre-compression phase, and (e) and (f) illustrate the samples after compression
1015 to $p' = 500$ kPa . The colour scaling indicates the orientation of the vectors normal to the particle
1016 principal planes in the x-z plane. These orientations are determined by projecting the vectors onto
1017 the x-z plane.
1018 Figure 7. Variation in void ratio with simulation time during pre-compression from an initial
1019 disperse cloud of non-contacting particles to a pressure of $p' = 0.1$ kPa.
1020 Figure 8. Polar histogram of the orientation of the vectors normal to the particle principal planes
1021 in the x-z plane. These orientations are determined by projecting the vectors onto the x-z plane:
1022 (a) and (b) before pre-compression phase, (c) and (d) after pre-compression phase, and (e) and
1023 (f) after initial compression.
1024 Figure 9. Results of simulations of initial loading and unloading using (a) the purely repulsive
1025 potential function (U_{PR}), i.e. S-PR; (b) the energy barrier potential (U_{EB}), i.e. S-EB.
1026 Figure 10. Histograms of surface-to-surface distance in S-PR during (a) loading simulation; (b)
1027 unloading simulations.

1028 Figure 11. Histograms of surface-to-surface distance in S-EB during (a) loading simulation; (b)
1029 unloading simulations (note change in limit on vertical axis).
1030 Figure 12. Variation in the face-to-face contact coordination number for (a) S-PR and (b) S-EB.
1031 Figure 13. Numerical results of simulations during reloading simulation.
1032 Figure 14. (a) Relationship between number of interactions exceeding the energy barrier and
1033 mean effective stress; (b) its proportion of interactions.
1034 Figure 15. Comparison of potential functions with different energy barrier heights.
1035 Figure 16. Numerical results for virtual samples with different energy barrier heights during loading
1036 and unloading.
1037 Figure 17. Histograms of surface-to-surface distance at 100 kPa (end of initial loading) for (a)
1038 100 % of height of original energy barrier, (b) 50 % of height of original energy barrier and (c)
1039 25 % of height of original energy barrier.
1040
1041 Table 1. DLVO parameters (see Eqs (2) and (3)) for the kaolinite particle saturated by the pore
1042 water with pH = 8 and salt concentration = 1 mM (developed with reference to Gupta (2011)).
1043 Table 2. Calibrated parameters for U_{PR} and U_{EB}.
1044 Table 3. Compression and swelling indexes (C_c and C_s) in loading and unloading simulations.
1045 Table 4. Compression and swelling indexes for EB potentials with different heights of energy
1046 barrier.
1047

1048 Table 1. DLVO parameters (see Eqs (2) and (3)) for the kaolinite particle saturated by the pore
1049 water with pH = 8 and salt concentration = 1 mM (developed with reference to Gupta (2011)).

DLVO parameter		face-face configuration	edge-edge configuration
A_H	J	2.08×10^{-20}	2.37×10^{-20}
$\delta_1 = \delta_2$	nm	200	2000
ε_r		78	78
ϵ_0	F/m	8.854×10^{-12}	8.854×10^{-12}
$1/\kappa$	nm	9.6	9.6
ψ_1	mV	-67.05	-219.97
ψ_2	mV	-55.27	-219.97

1050
1051

1052 Table 2. Calibrated parameters for U_{PR} and U_{EB}.

U_{GB}		U_{PR}	U_{EB}
γ		0.572	1.0
ε	J	2.98×10^{-21}	—
σ	nm	199.6	846.8
$\epsilon_{ia}=\epsilon_{ib}$		63.45	3.45
ϵ_{ic}		23.74	1.0
$a_i=b_i$	nm	1000	1000
c_i	nm	100	100
A	J	—	8.25×10^{-16}
B	J	—	1.65×10^{-15}
C	J	—	8.25×10^{-16}
k	J/nm^2	—	3.13×10^{-21}
m	J/nm	—	0.0
n	J	—	-6.17×10^{-17}

1053

1054 Table 3. Compression and swelling indexes (C_c and C_s) in loading and unloading simulations.

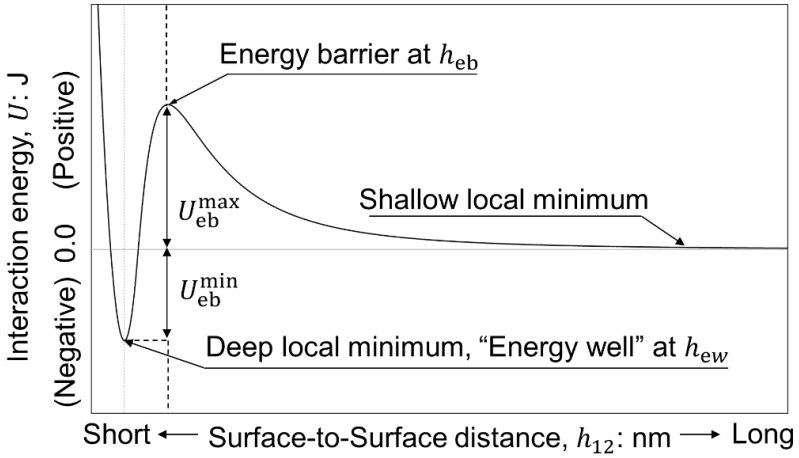
	Compression Index: C_c				
	$C_{c,\ 10\text{-}100}$	$C_{c,\ 10\text{-}200}$	$C_{c,\ 10\text{-}300}$	$C_{c,\ 10\text{-}400}$	$C_{c,\ 10\text{-}500}$
S-EB	0.0964	0.0915	0.0894	0.0877	0.0859
S-PR	0.1066	0.1041	0.1029	0.1020	0.1011

	Swelling Index: C_s				
	$C_{s,\ 10\text{-}100}$	$C_{s,\ 10\text{-}200}$	$C_{s,\ 10\text{-}300}$	$C_{s,\ 10\text{-}400}$	$C_{s,\ 10\text{-}500}$
S-EB	0.0736	0.0558	0.0414	0.0305	0.0201
S-PR	0.0986	0.0965	0.0952	0.0946	0.0941

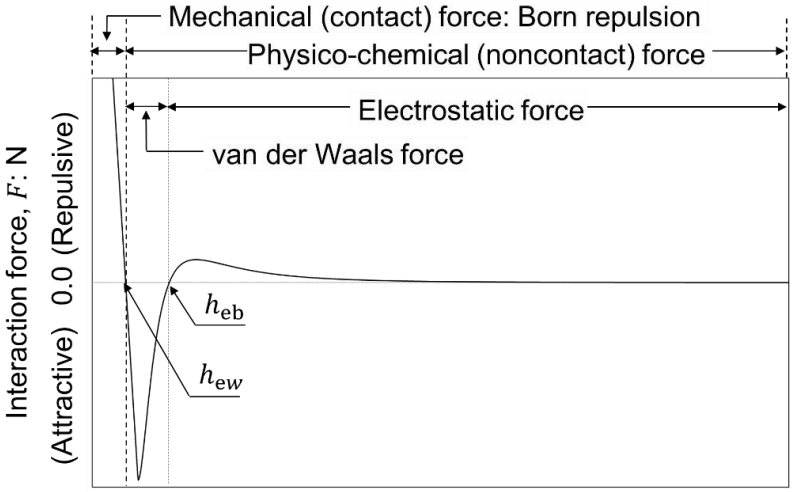
1055

Table 4. Compression and swelling indexes for EB potentials with different heights of energy barrier.

Case ID	Compression Index: C_c	Swelling Index: C_s	C_s/C_c
	$C_{c,\ 10\text{-}100}$	$C_{s,\ 10\text{-}100}$	
100%	0.0964	0.0736	0.763
50%	0.0848	0.0503	0.593
25%	0.0789	0.0218	0.276



(a)

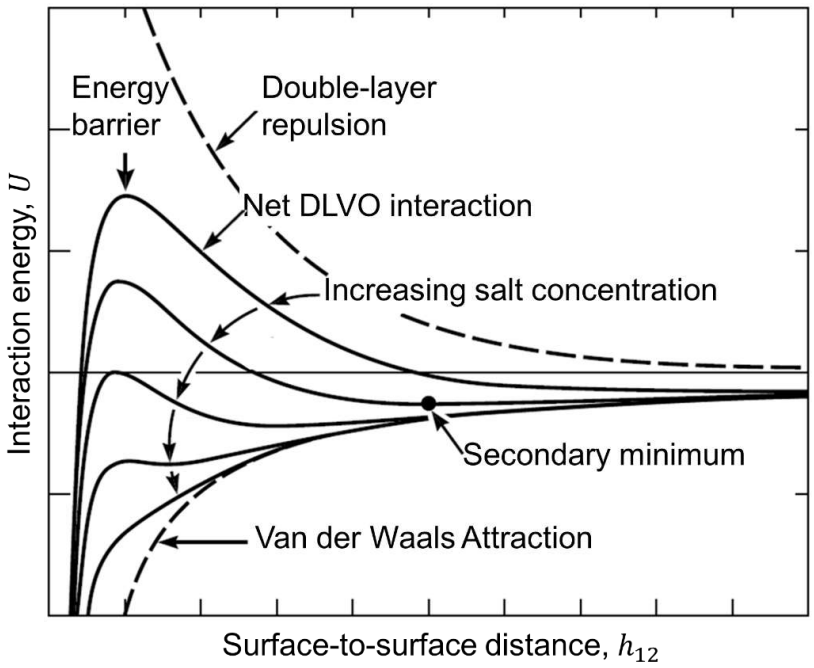


(b)

1060

1061 Fig. 1. Idealised interaction between two kaolinite particles (a) interaction energy and (b)

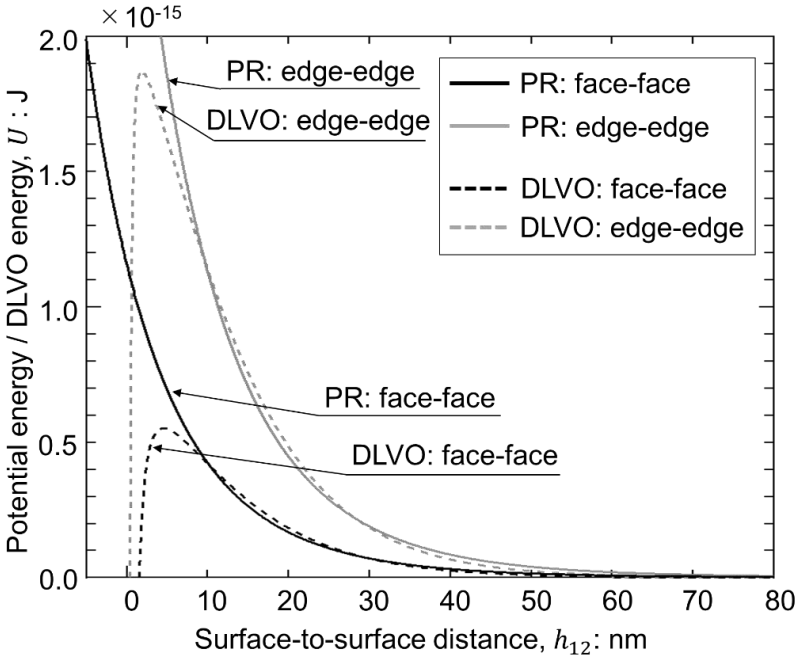
1062 interaction force adopted by Lu et al. (2008).



1063

1064 Fig. 2 Schematic diagram of interaction energy-separation distance profile for double-layer
1065 repulsion, van der Waals attraction, and net DLVO energy (modified from Israelachvili, 2011;
1066 Masliyah & Bhattacharjee, 2005).

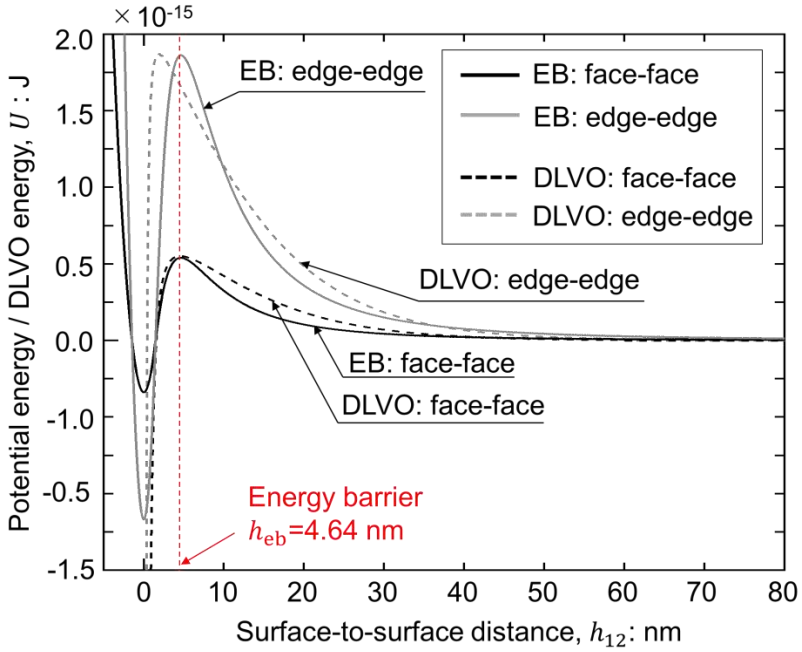
1067



1068

1069 Fig. 3. Calibrated PR (purely repulsive) potential (U_{PR}) compared with DLVO-generated data for

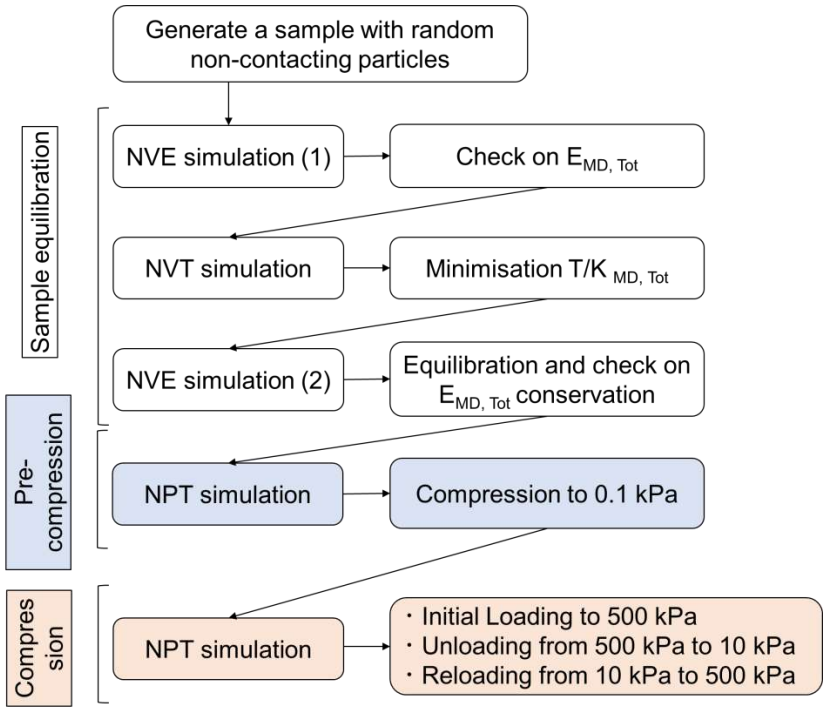
1070 face-face and edge-edge configurations for ellipsoids 2,000 nm in diameter and 200 nm thick.



1071

1072 Fig. 4. Calibrated EB (energy barrier) potential (U_{EB}) compared with DLVO-generated data for

1073 face-face and edge-edge configurations for ellipsoids 2,000 nm in diameter and 200 nm thick.



1074

1075 Fig. 5. Workflow of isotropic compression simulation

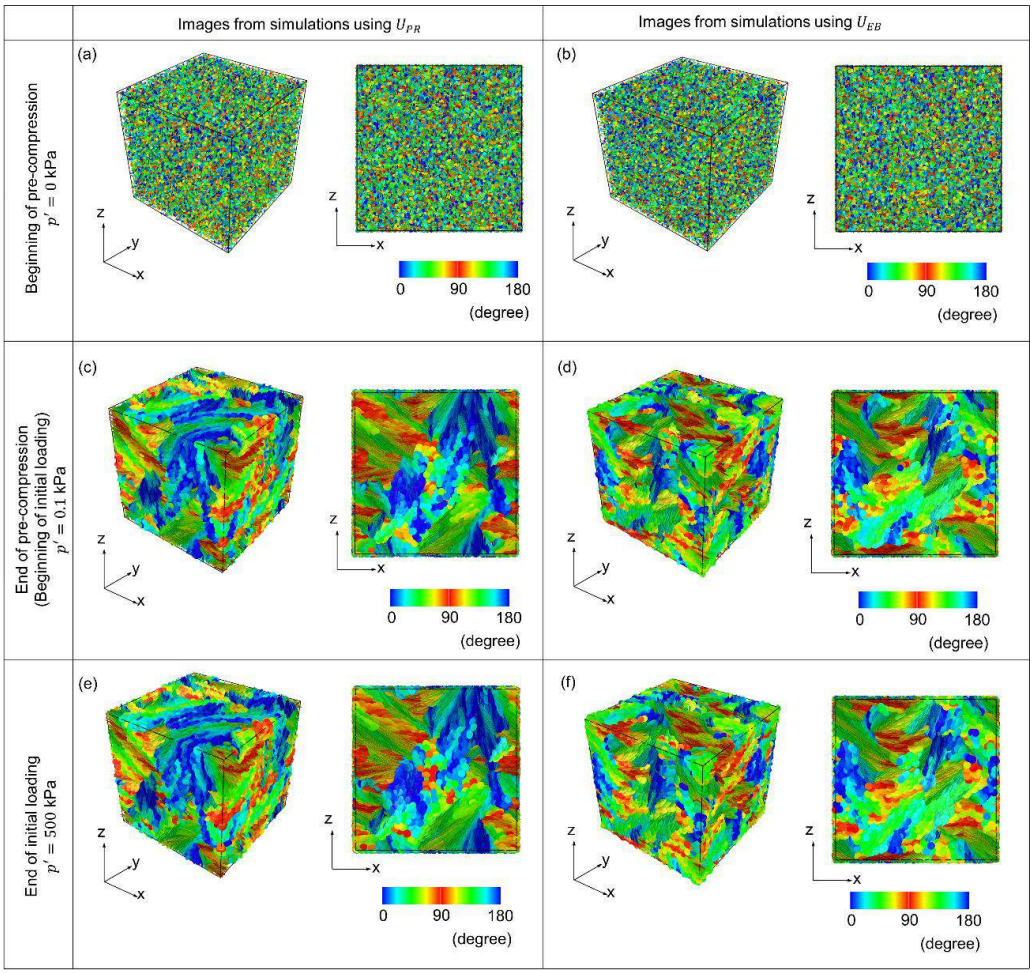


Fig. 6. Illustrations of virtual samples (103,823 particles). Left hand column gives images from simulations using the purely repulsive potential function, U_{PR}, while the right hand column gives images simulations using the energy barrier potential function, U_{EB}: (a) and (b) illustrate the initial configuration before the pre-compression phase ($p' = 0.1$ kPa), (c) and (d) illustrate the virtual samples after the pre-compression phase, and (e) and (f) illustrate the samples after compression to $p' = 500$ kPa . The colour scaling indicates the orientation of the vectors normal to the particle principal planes in the x-z plane. These orientations are determined by projecting the vectors onto the x-z plane.

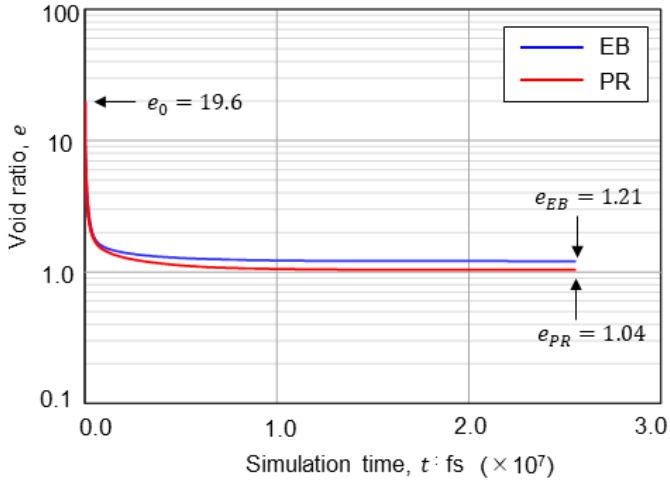


Fig. 7. Variation in void ratio with simulation time during pre-compression from an initial disperse cloud of non-contacting particles to a pressure of $p' = 0.1$ kPa.

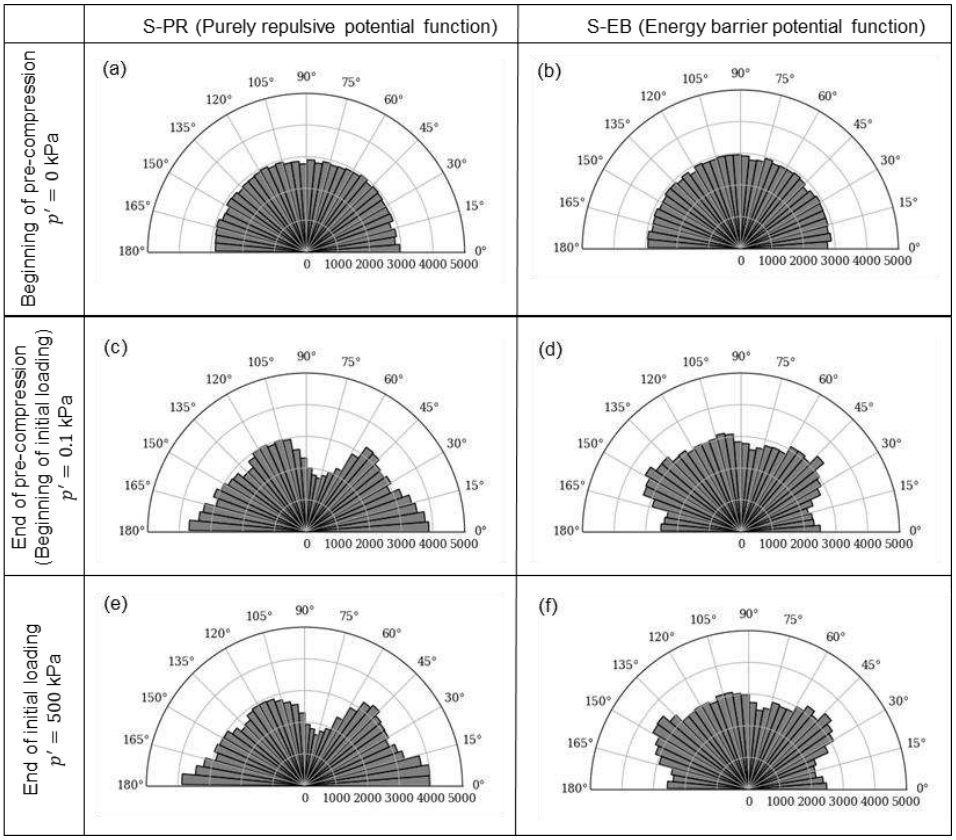


Fig. 8. Polar histogram of the orientation of the vectors normal to the particle principal planes in the x-z plane. These orientations are determined by projecting the vectors onto the x-z plane: (a) and (b) before pre-compression phase, (c) and (d) after pre-compression phase, and (e) and (f) after initial compression.

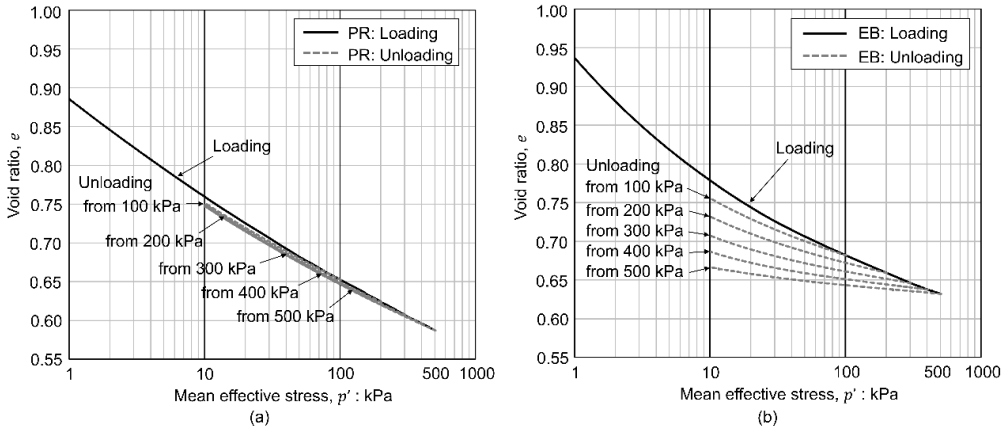


Fig. 9. Results of simulations of initial loading and unloading using (a) the purely repulsive potential function (U_{PR}), i.e. S-PR; (b) the energy barrier potential (U_{EB}), i.e. S-EB.

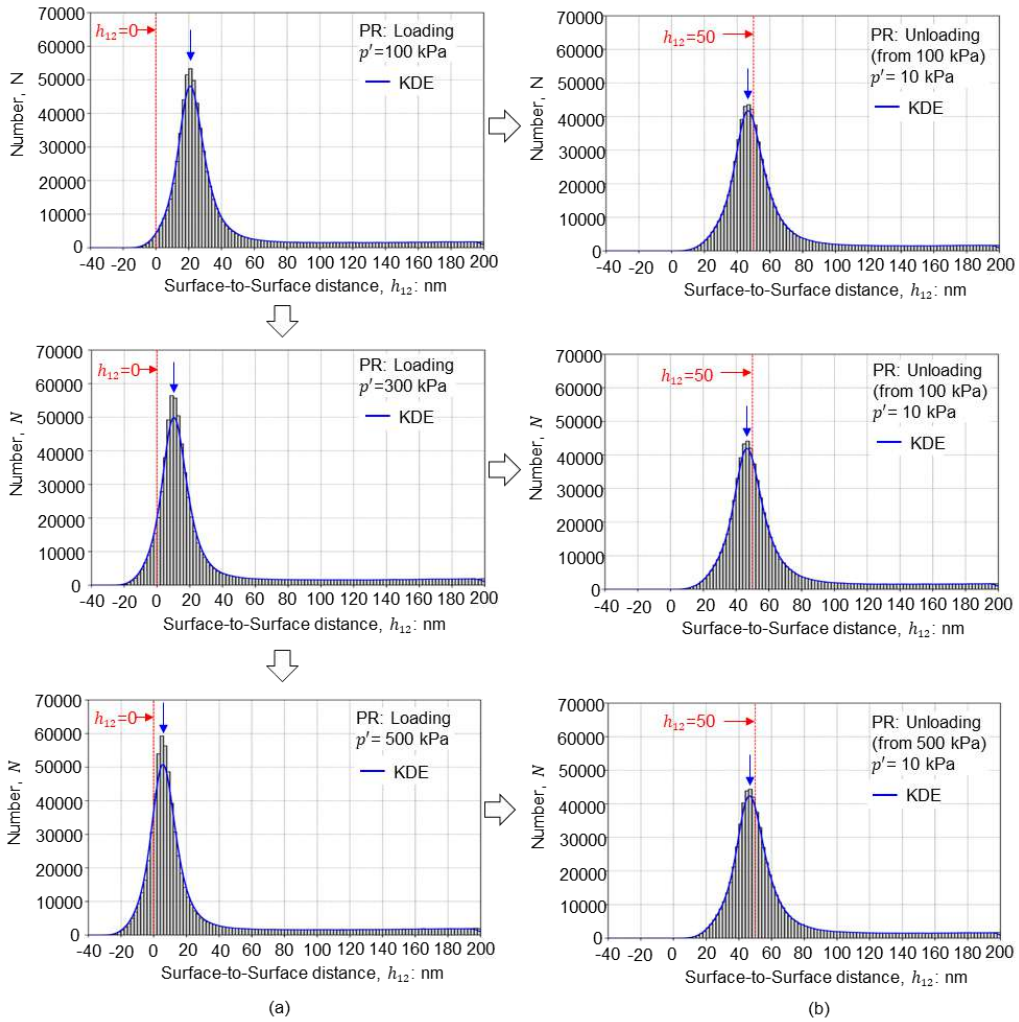


Fig. 10. Histograms of surface-to-surface distance in S-PR during (a) loading simulation; (b) unloading simulations.

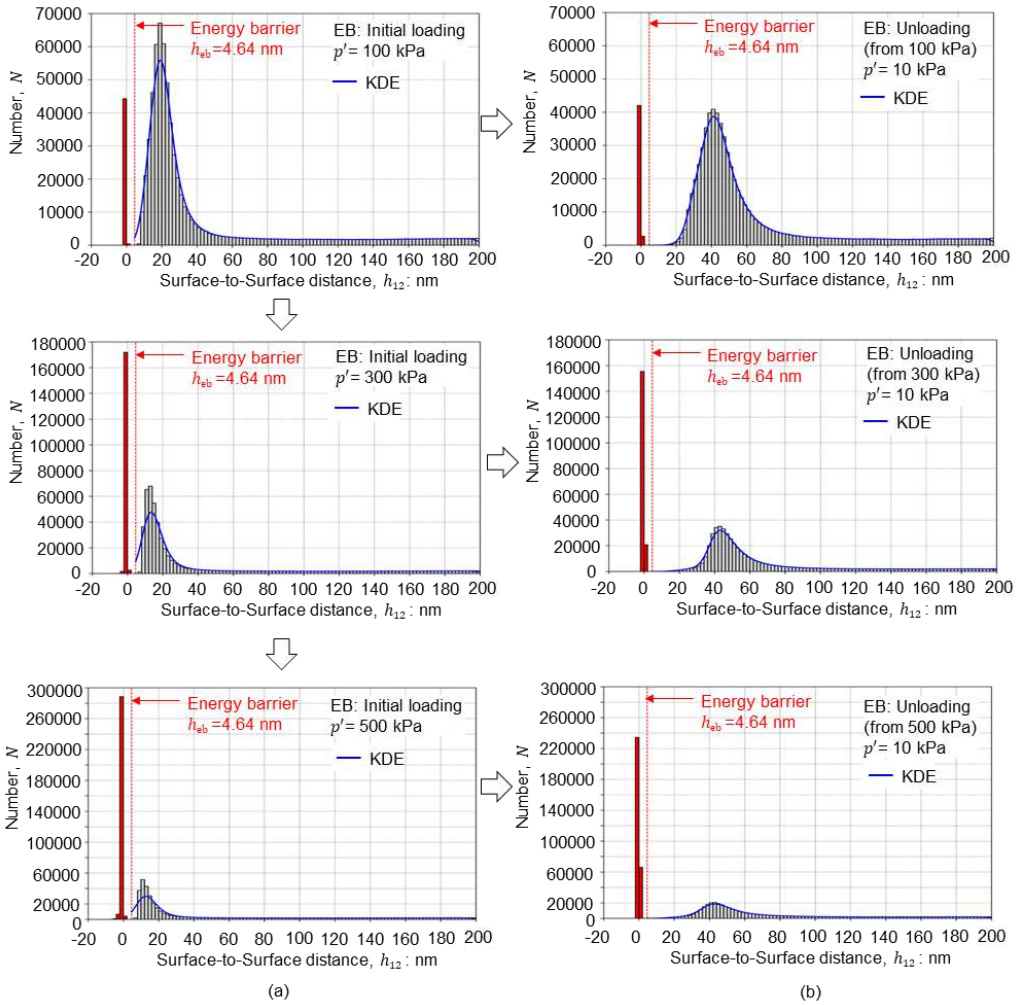
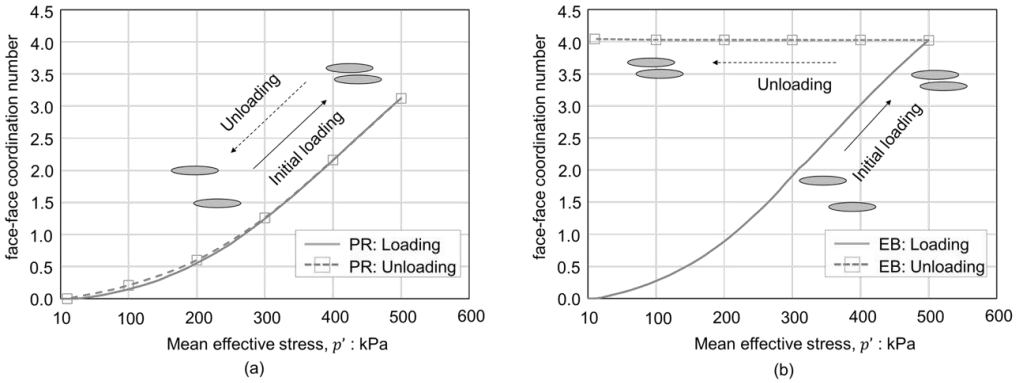
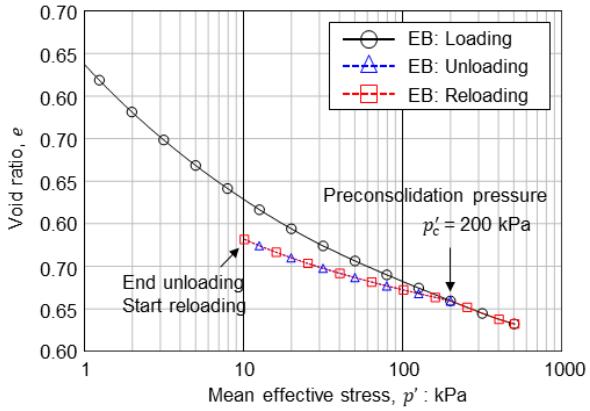


Fig. 11. Histograms of surface-to-surface distance in S-EB during (a) loading simulation; (b) unloading simulations (note change in limit on vertical axis).



1105

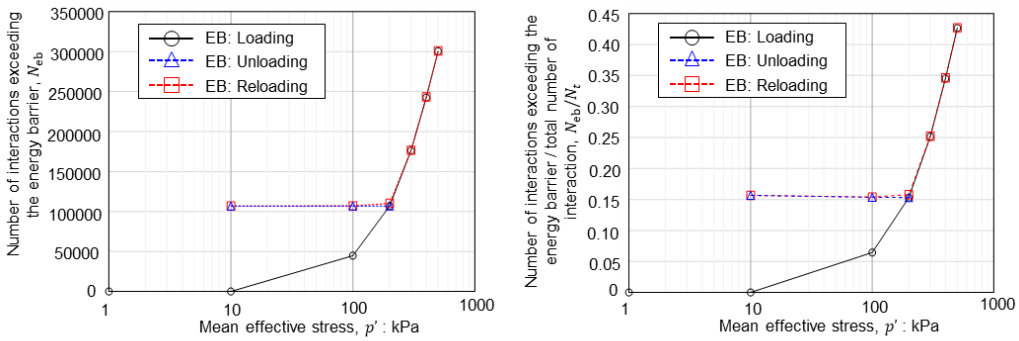
1106 Fig. 12. Variation in the face-to-face contact coordination number for (a) S-PR and (b) S-EB.



1107

1108 Fig. 13. Numerical results of simulations during reloading simulation.

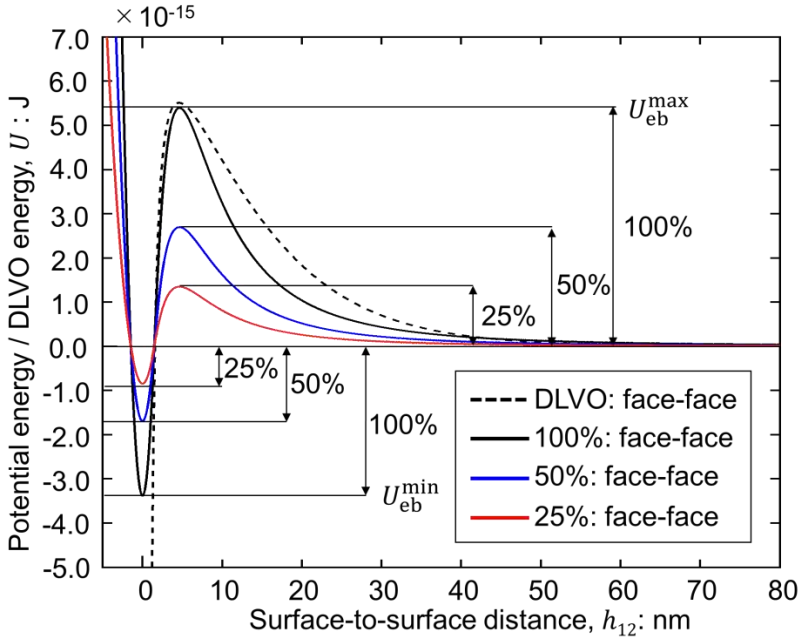
1109



1110

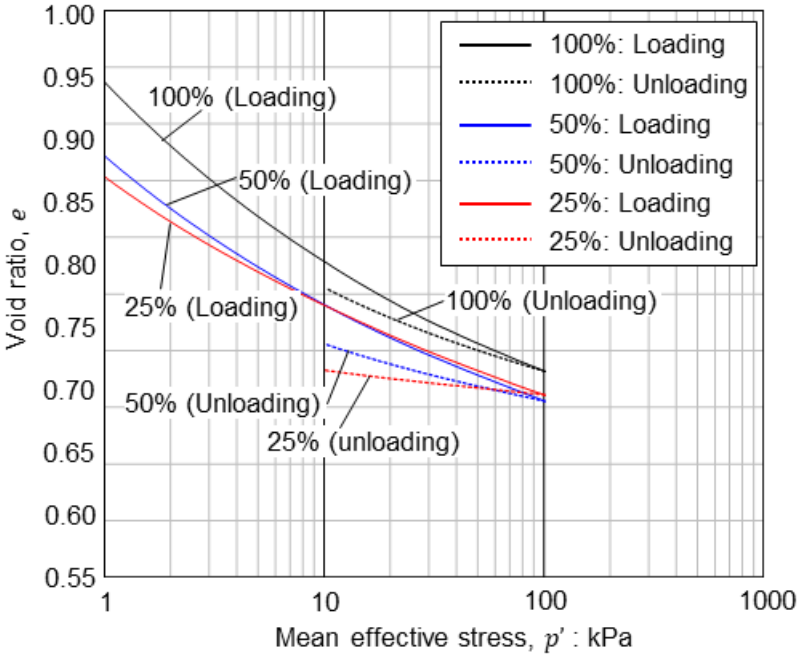
1111 Fig. 14. (a) Relationship between number of interactions exceeding the energy barrier and

1112 mean effective stress; (b) its proportion of interactions.



1113

1114 Fig. 15. Comparison of potential functions with different energy barrier heights.

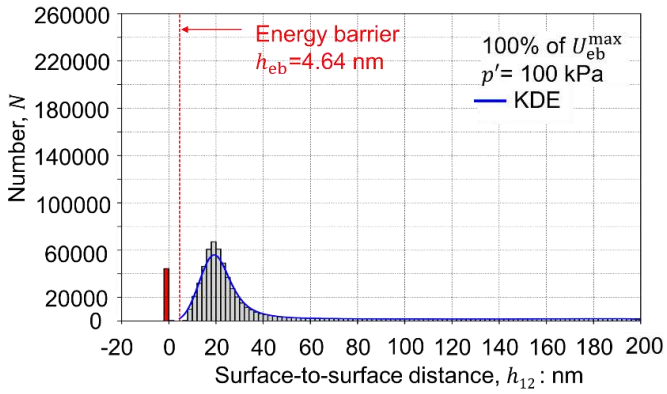


1115

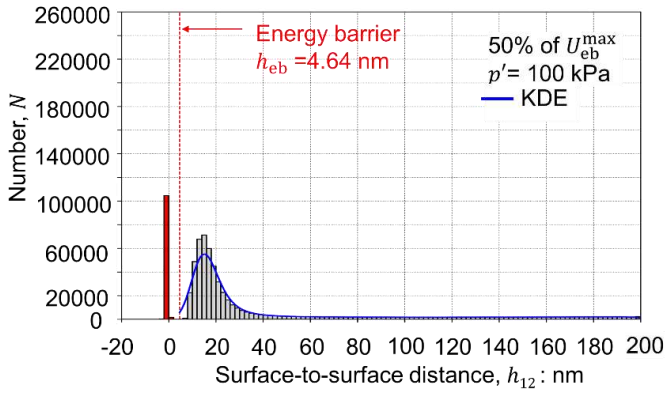
1116 Fig. 16. Numerical results for virtual samples with different energy barrier heights during loading

1117 and unloading.

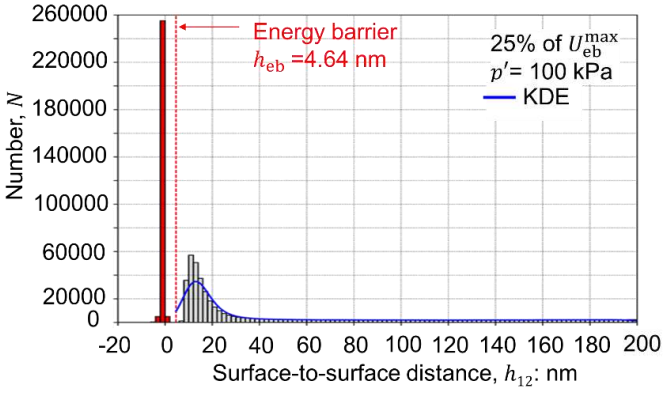
1118



(a)



(b)



(c)

Fig. 17. Histograms of surface-to-surface distance at 100 kPa (end of initial loading) for (a) 100 % of height of original energy barrier, (b) 50 % of height of original energy barrier and (c) 25 % of height of original energy barrier.

1 Table 1. DLVO parameters (see Eqs (2) and (3)) for the kaolinite particle saturated by the pore
2 water with pH = 8 and salt concentration = 1 mM (developed with reference to Gupta (2011)).

DLVO parameter		face-face configuration	edge-edge configuration
A_H	J	2.08×10^{-20}	2.37×10^{-20}
$\delta_1 = \delta_2$	nm	200	2000
ε_r		78	78
ϵ_0	F/m	8.854×10^{-12}	8.854×10^{-12}
$1/\kappa$	nm	9.6	9.6
ψ_1	mV	-67.05	-219.97
ψ_2	mV	-55.27	-219.97

3

4 Table 2. Calibrated parameters for U_{PR} and U_{EB}

U_{GB}		U_{PR}	U_{EB}
γ		0.572	1.0
ε	J	2.98×10^{-21}	—
σ	nm	199.6	846.8
$\epsilon_{ia} = \epsilon_{ib}$		63.45	3.45
ϵ_{ic}		23.74	1.0
$a_i = b_i$	nm	1000	1000
c_i	nm	100	100
A	J	—	8.25×10^{-16}
B	J	—	1.65×10^{-15}
C	J	—	8.25×10^{-16}
k	J/nm^2	—	3.13×10^{-21}
m	J/nm	—	0.0
n	J	—	-6.17×10^{-17}

5

6 Table 3. Compression and swelling indexes (C_c and C_s) in loading and unloading simulations

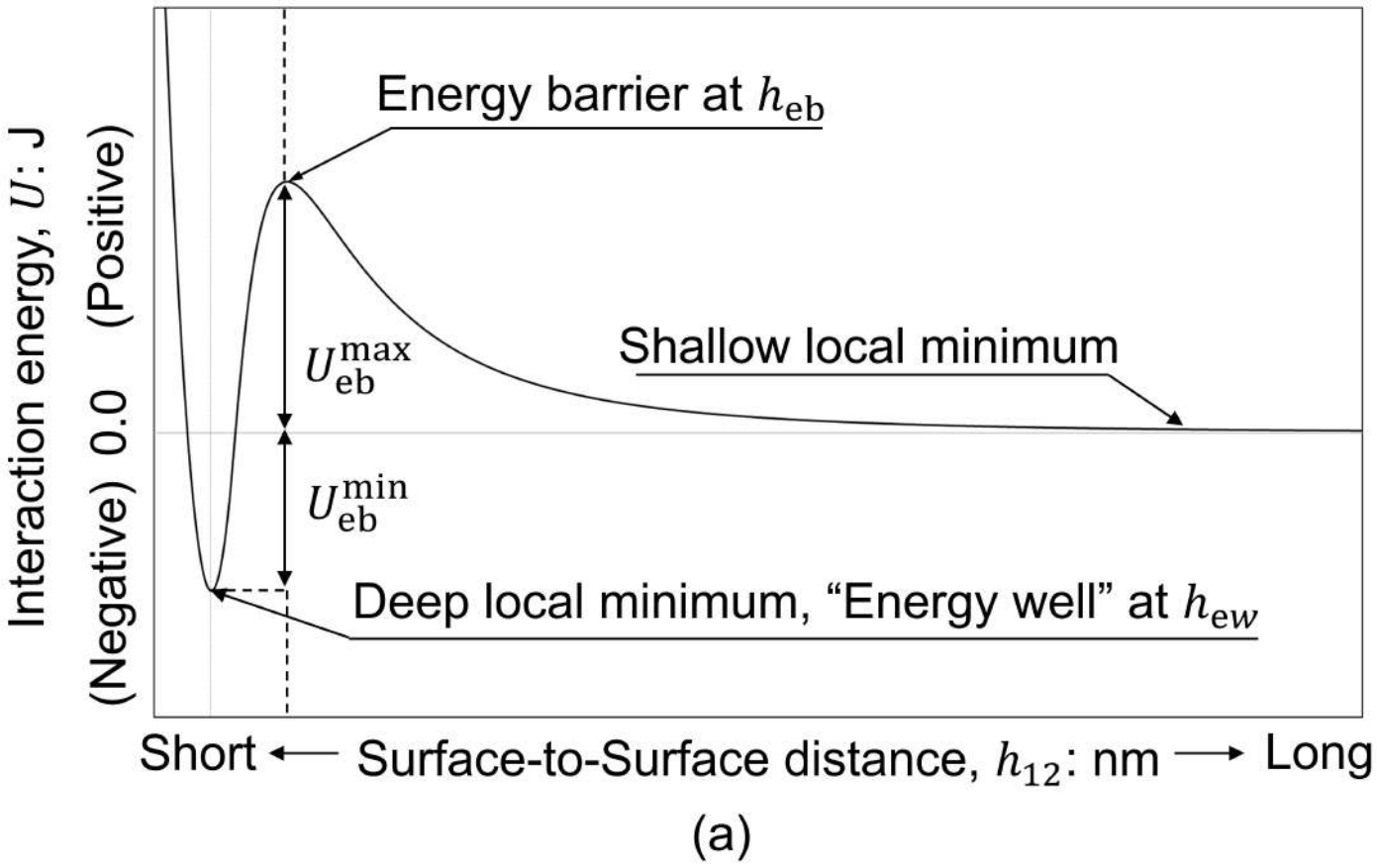
	Compression Index: C_c				
	$C_{c,\ 10\text{-}100}$	$C_{c,\ 10\text{-}200}$	$C_{c,\ 10\text{-}300}$	$C_{c,\ 10\text{-}400}$	$C_{c,\ 10\text{-}500}$
S-EB	0.0964	0.0915	0.0894	0.0877	0.0859
S-PR	0.1066	0.1041	0.1029	0.1020	0.1011

	Swelling Index: C_s				
	$C_{s,\ 10\text{-}100}$	$C_{s,\ 10\text{-}200}$	$C_{s,\ 10\text{-}300}$	$C_{s,\ 10\text{-}400}$	$C_{s,\ 10\text{-}500}$
S-EB	0.0736	0.0558	0.0414	0.0305	0.0201
S-PR	0.0986	0.0965	0.0952	0.0946	0.0941

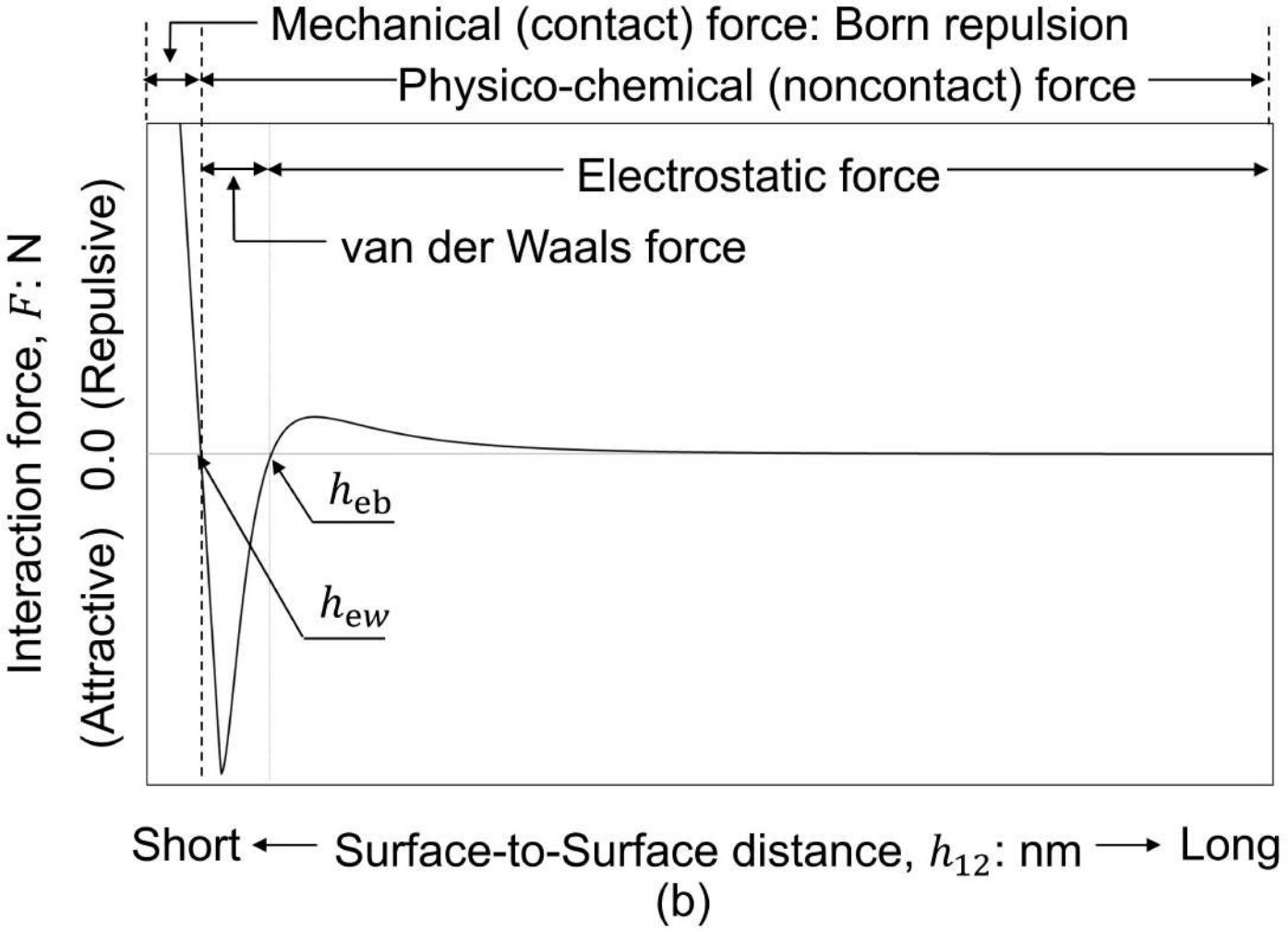
7

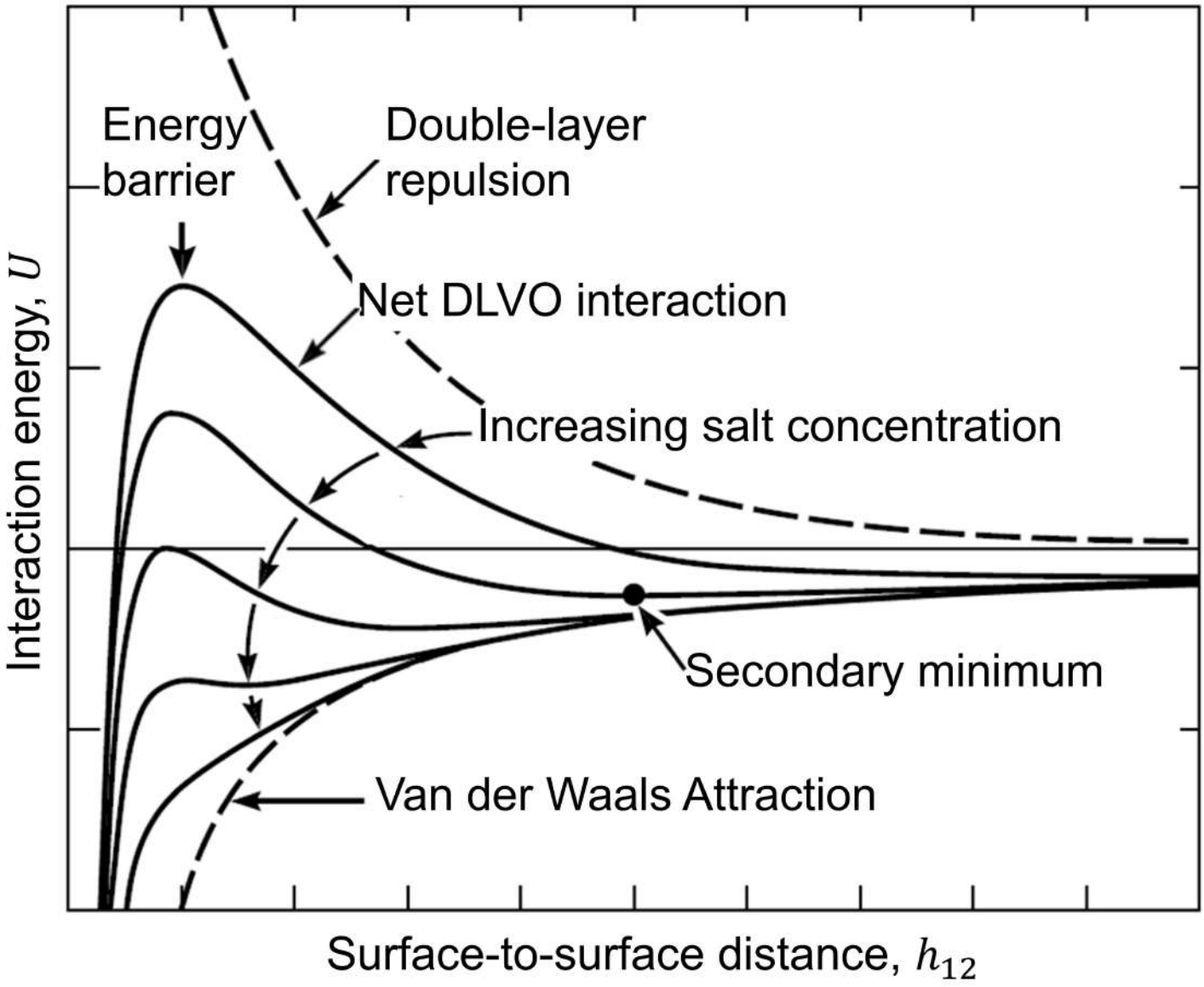
Table 4. Compression and swelling indexes for EB potentials with different heights of energy barrier

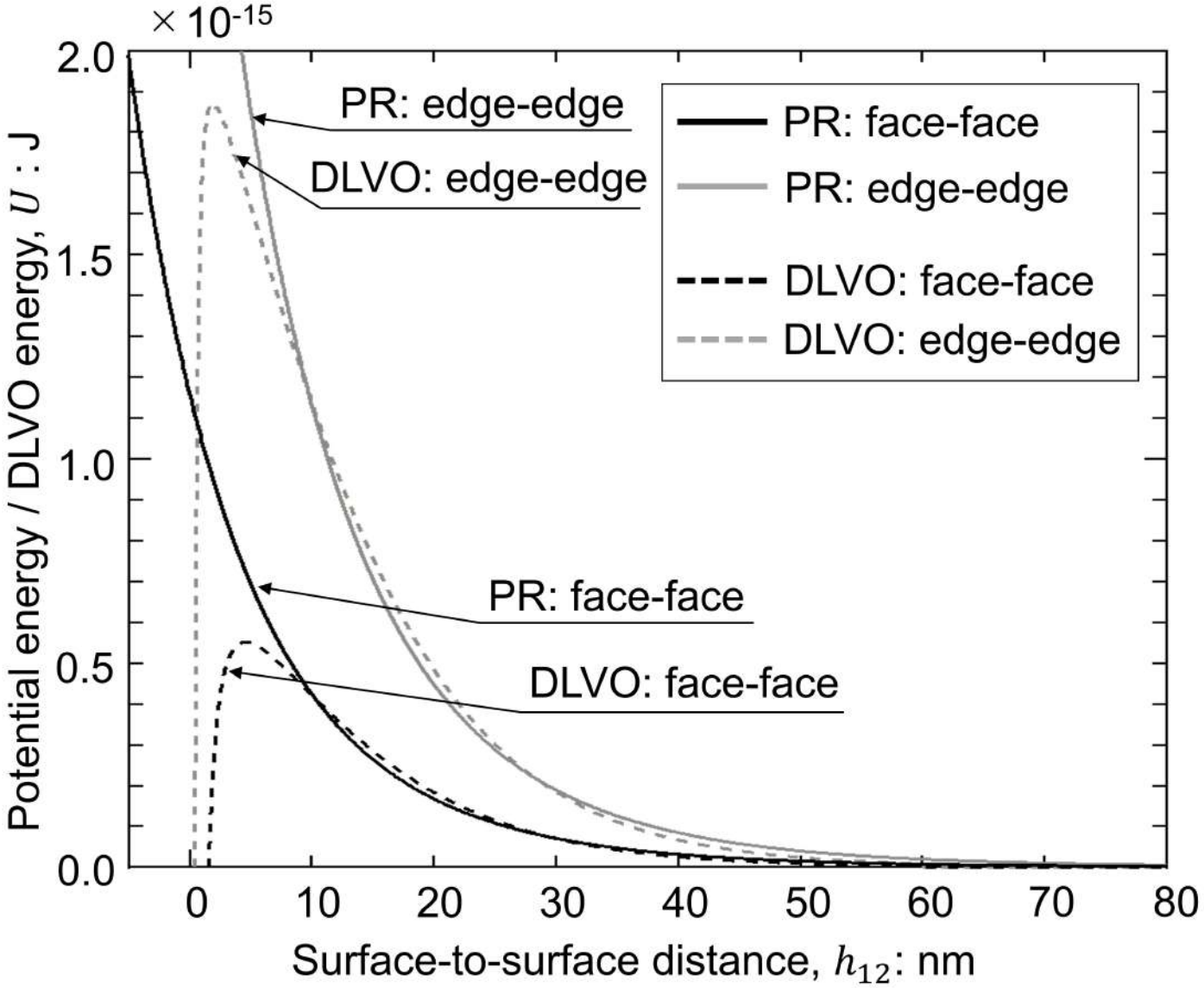
Case ID	Compression Index: C_c	Swelling Index: C_s	C_s/C_c
	$C_{c,\ 10\text{-}100}$	$C_{s,\ 10\text{-}100}$	
100%	0.0964	0.0736	0.763
50%	0.0848	0.0503	0.593
25%	0.0789	0.0218	0.276

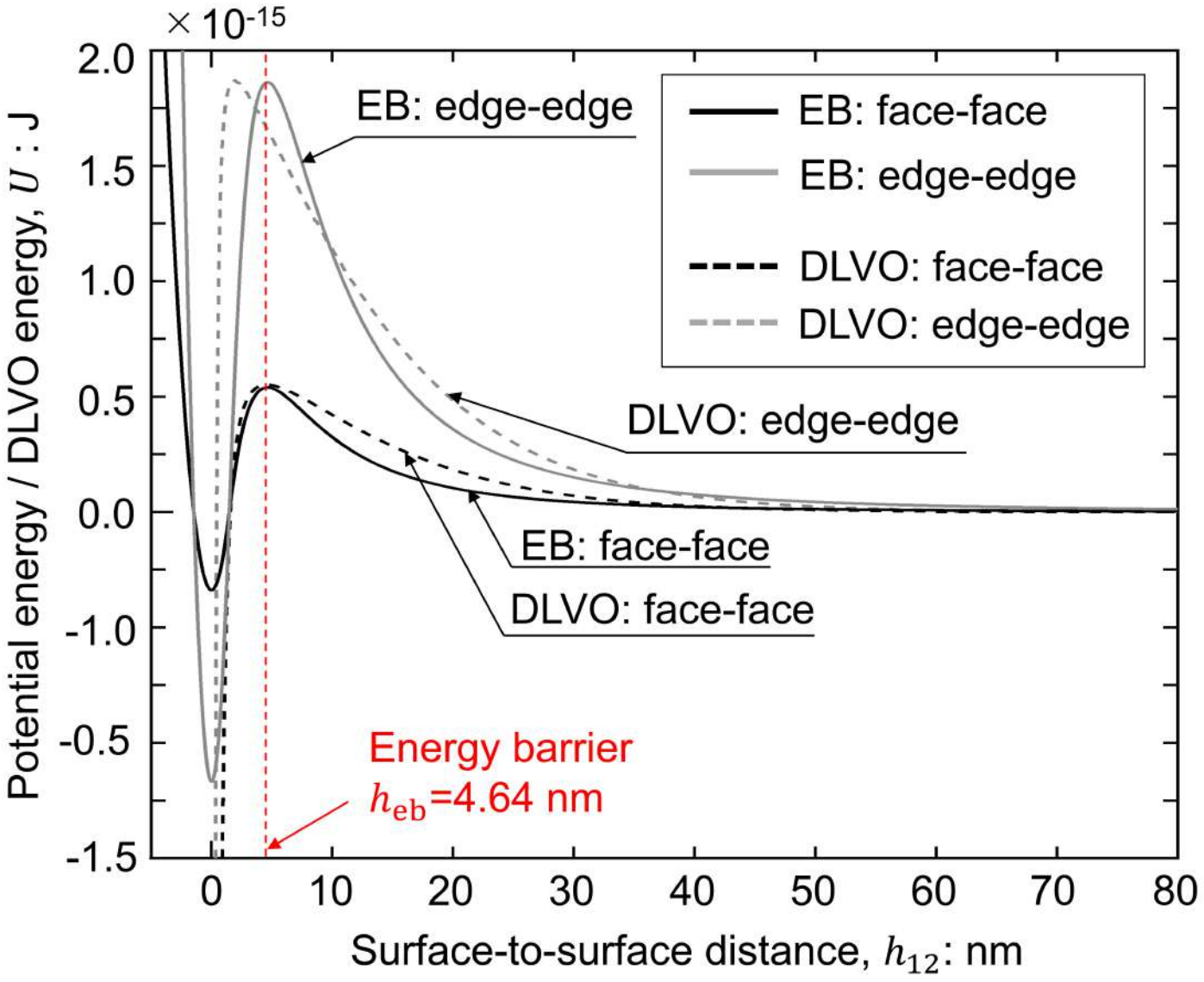

Energy barrier at h_{eb}
Shallow local minimum
$U_{\mathrm{eb}}^{\max}$
$U_{\mathrm{eb}}^{\min}$
Deep local minimum, "Energy well" at h_{ew}
Interaction energy, U: J
(Negative) 0.0 (Positive)
Short ← Surface-to-Surface distance, h_{12}: nm → Long

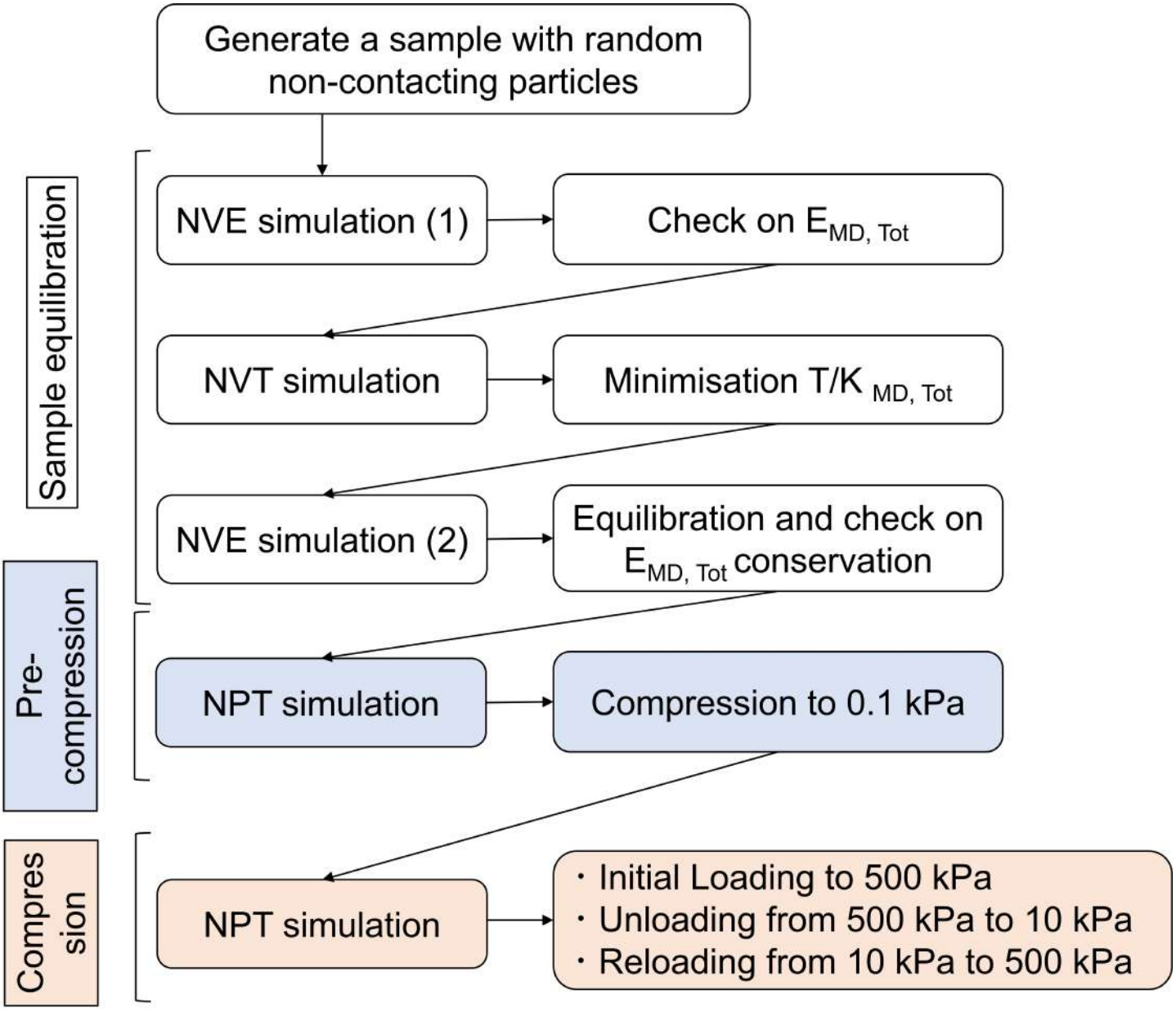
(a)

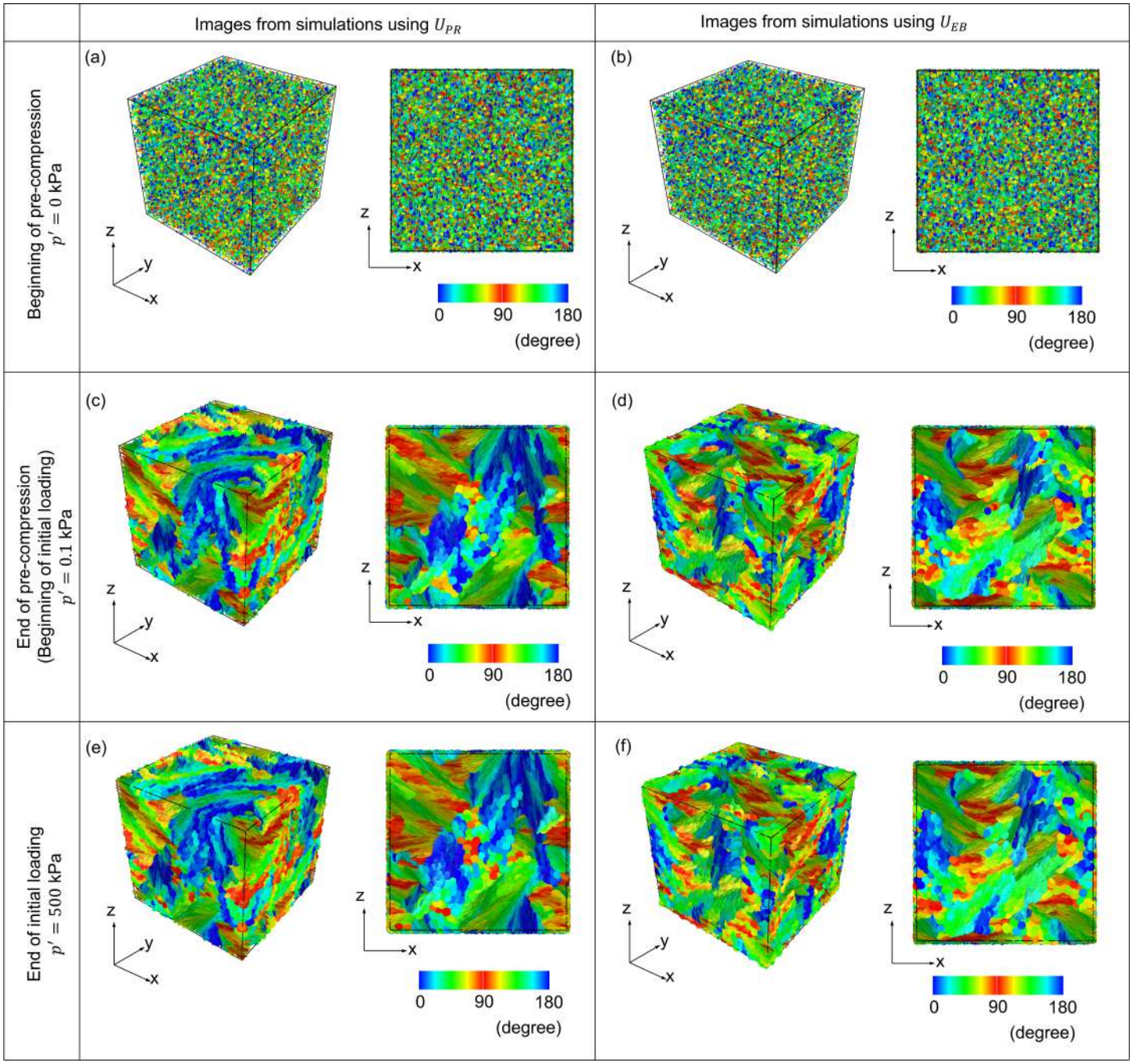

Mechanical (contact) force: Born repulsion
Physico-chemical (noncontact) force
Electrostatic force
van der Waals force
Interaction force, F: N
(Attractive) 0.0 (Repulsive)
h_{eb}
h_{ew}
Short ← Surface-to-Surface distance, h_{12}: nm → Long
(b)

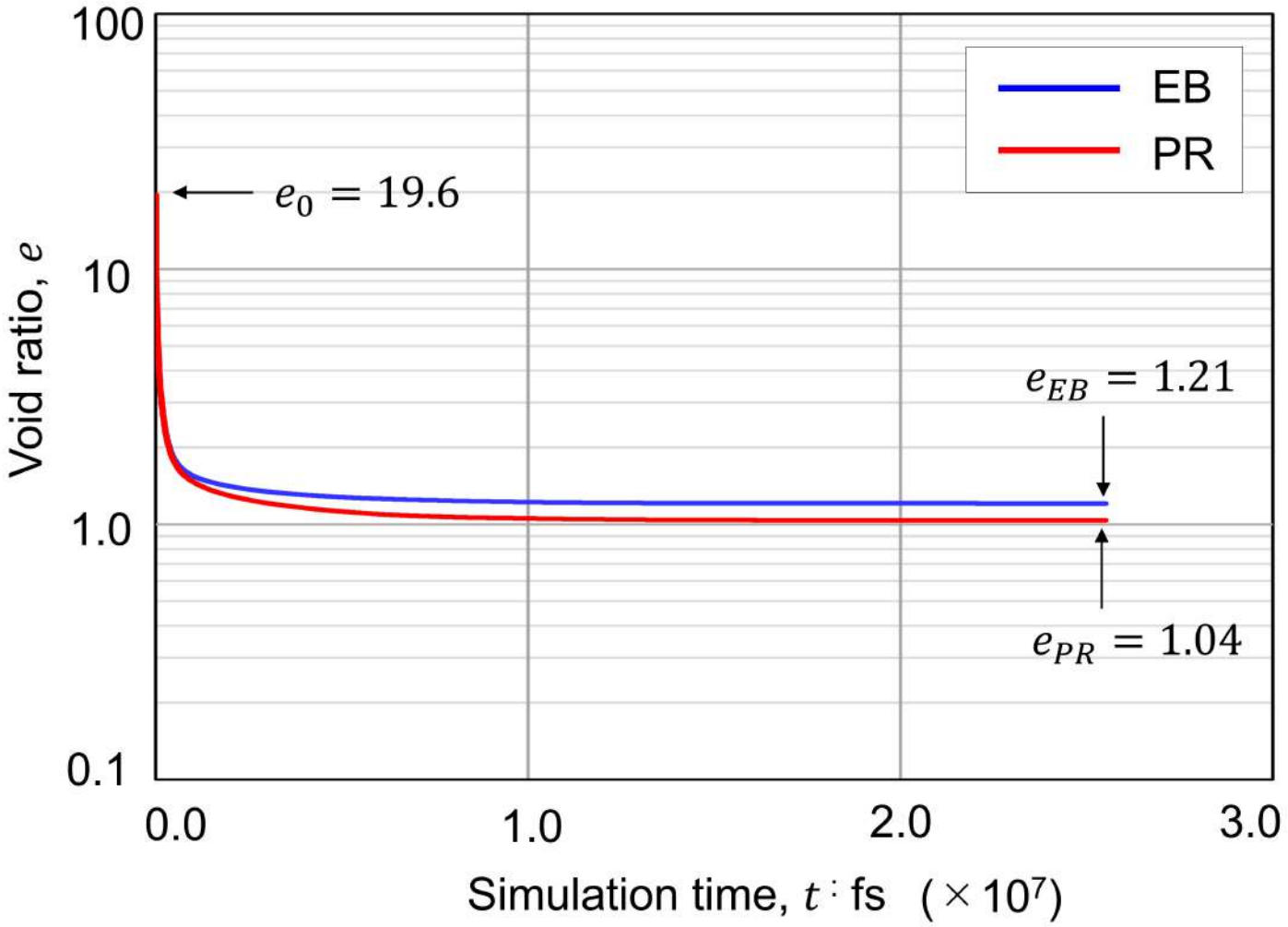

Energy barrier
Double-layer repulsion
Net DLVO interaction
Increasing salt concentration
Secondary minimum
Van der Waals Attraction
Interaction energy, U
Surface-to-surface distance, h_{12}

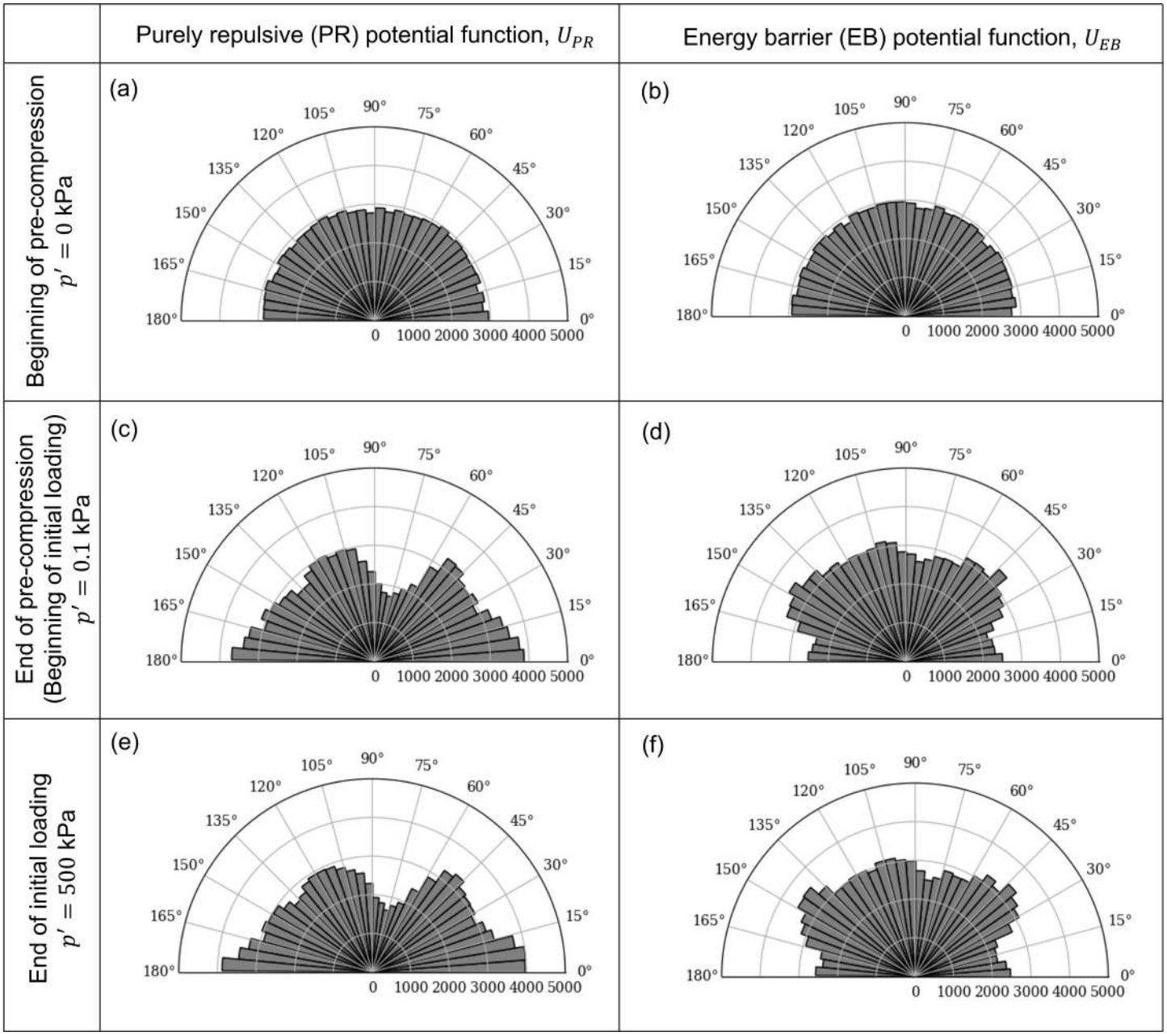

× 10-15
2.0
1.5
1.0
0.5
0.0
Potential energy / DLVO energy, U : J
PR: edge-edge
DLVO: edge-edge
PR: face-face
DLVO: face-face
PR: face-face
PR: edge-edge
DLVO: face-face
DLVO: edge-edge
0
10
20
30
40
50
60
70
80
Surface-to-surface distance, h12: nm

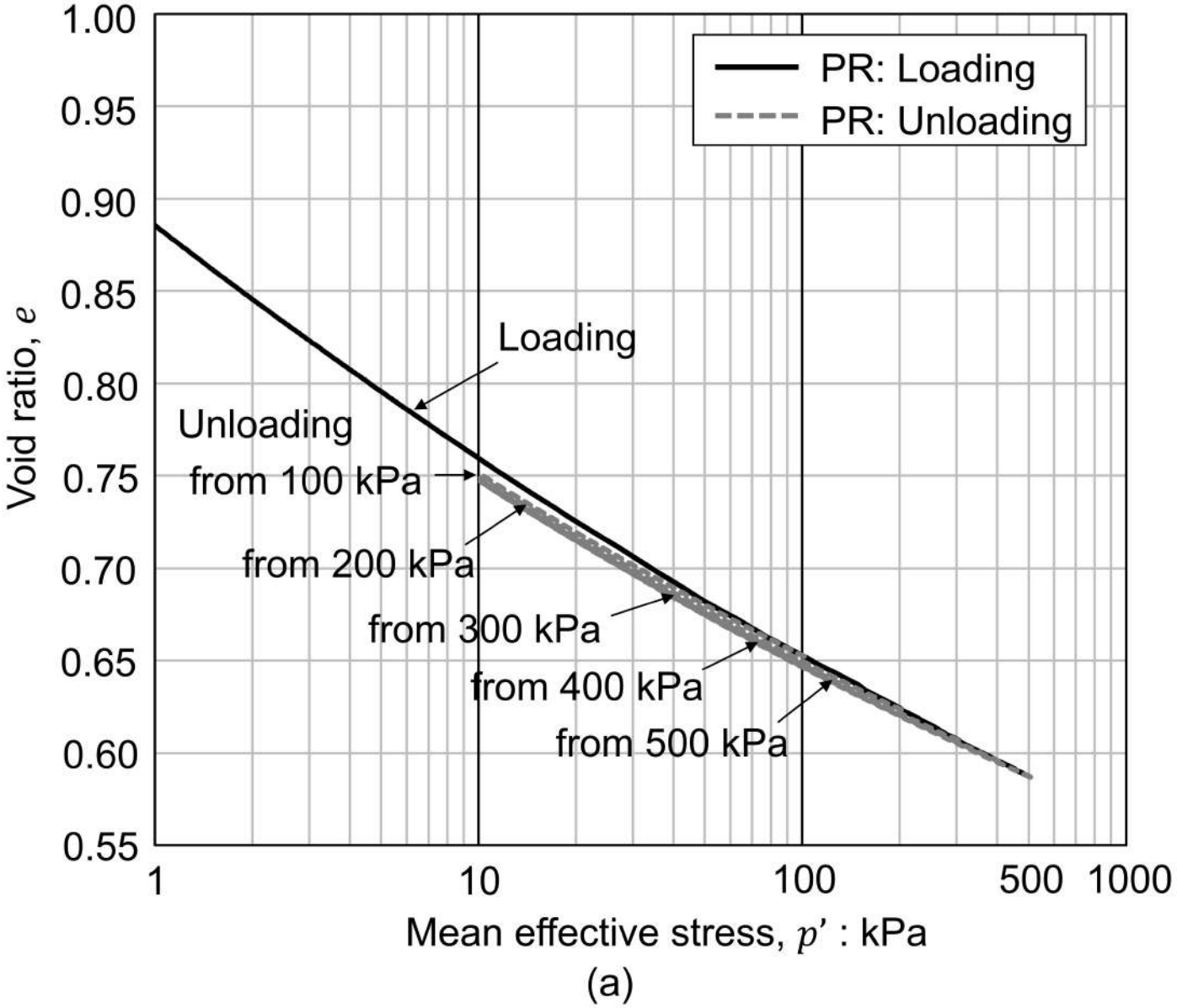

× 10-15
2.0
1.5
1.0
0.5
0.0
-1.0
-0.5
-1.5
Potential energy / DLVO energy, U : J
0
10
20
30
40
50
60
70
80
Surface-to-surface distance, h12: nm
EB: face-face
EB: edge-edge
DLVO: face-face
DLVO: edge-edge
EB: edge-edge
DLVO: edge-edge
EB: face-face
DLVO: face-face
Energy barrier
heb=4.64 nm

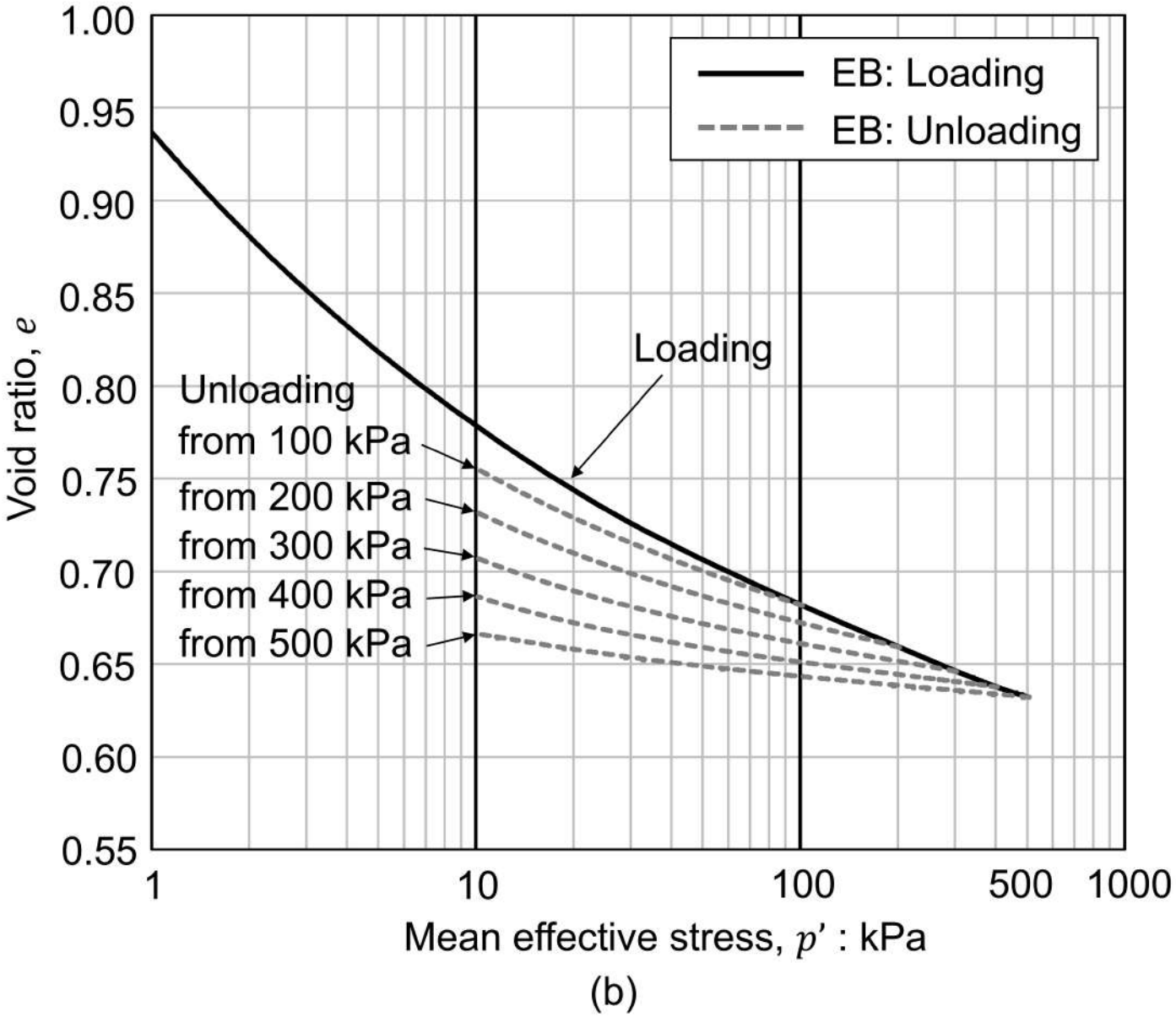

Generate a sample with random non-contacting particles
Sample equilibration
NVE simulation (1)
Check on $E_{MD, Tot}$
NVT simulation
Minimisation T/K $_{MD, Tot}$
NVE simulation (2)
Equilibration and check on $E_{MD, Tot}$ conservation
Pre-compression
NPT simulation
Compression to 0.1 kPa
Compression
NPT simulation
・Initial Loading to 500 kPa
・Unloading from 500 kPa to 10 kPa
・Reloading from 10 kPa to 500 kPa


Images from simulations using U_{PR}
Images from simulations using U_{EB}
Beginning of pre-compression
$p' = 0$ kPa
End of pre-compression
(Beginning of initial loading)
$p' = 0.1$ kPa
End of initial loading
$p' = 500$ kPa
(a)
(b)
(c)
(d)
(e)
(f)
z
y
x
0
90
180
(degree)

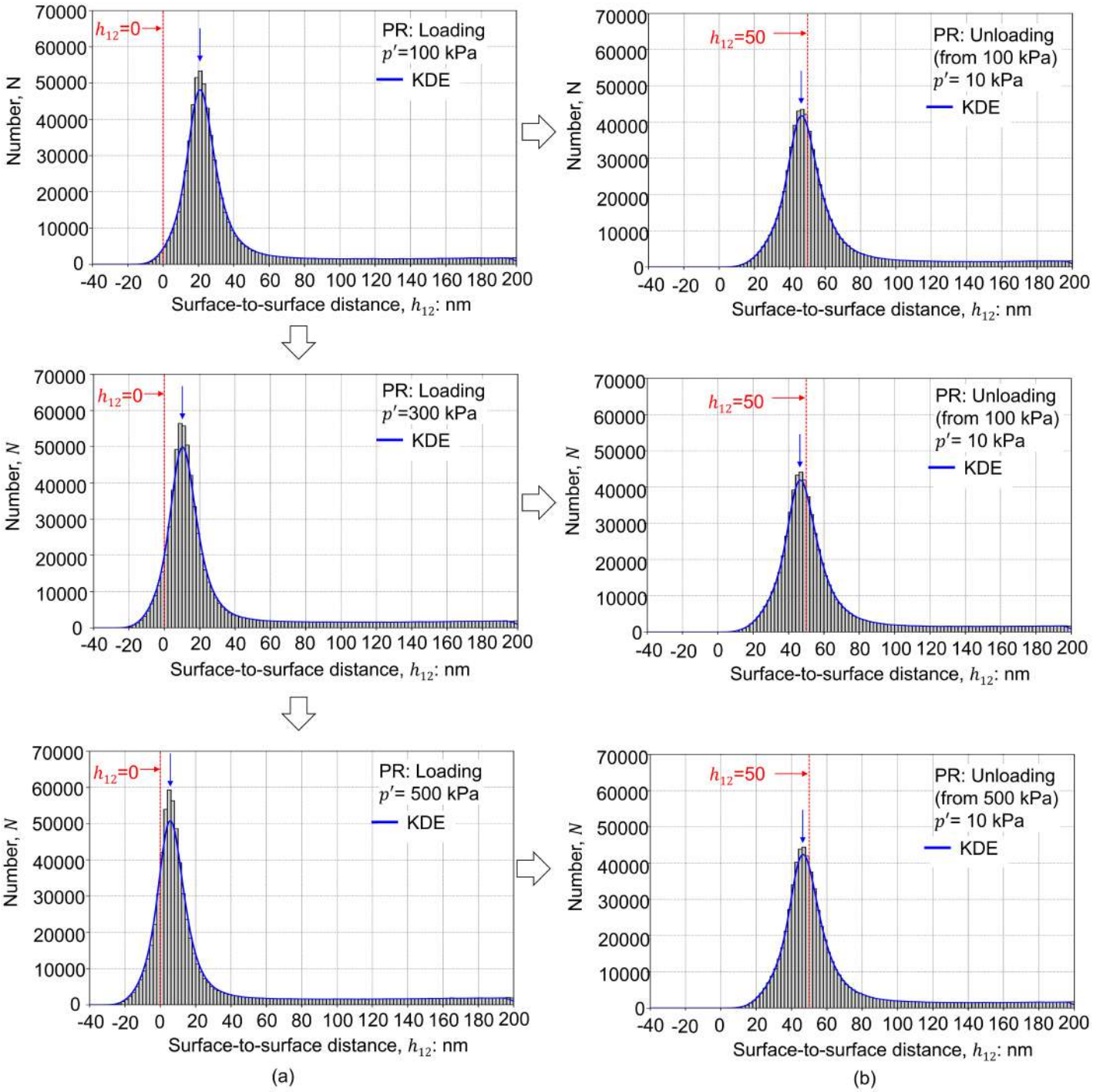

100
10
1.0
0.1
Void ratio, e
$e_0 = 19.6$
EB
PR
$e_{EB} = 1.21$
$e_{PR} = 1.04$
0.0
1.0
2.0
3.0
Simulation time, t : fs (×10⁷)

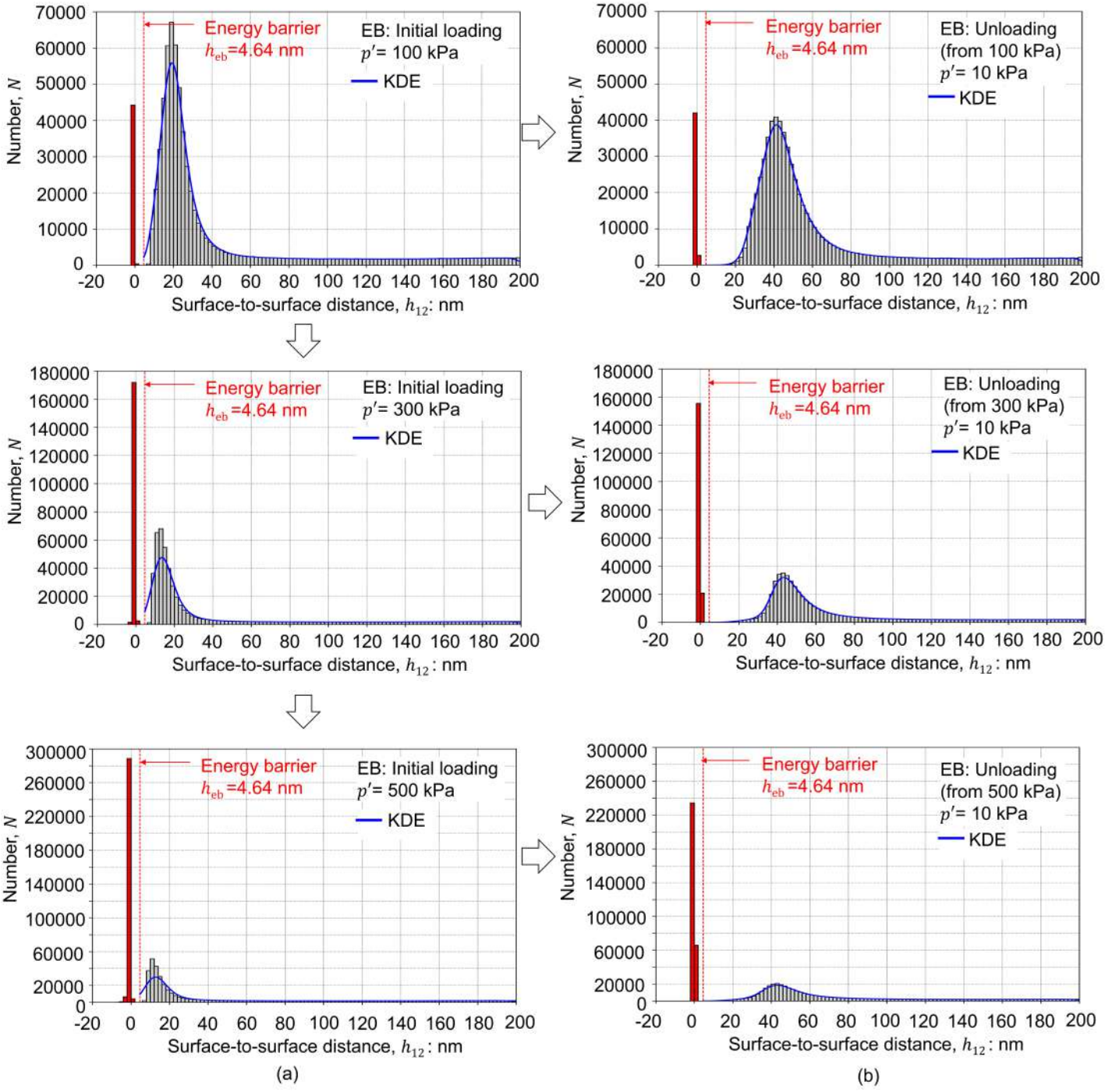

Purely repulsive (PR) potential function, U_{PR}
Energy barrier (EB) potential function, U_{EB}
Beginning of pre-compression
$p' = 0$ kPa
End of pre-compression
(Beginning of initial loading)
$p' = 0.1$ kPa
End of initial loading
$p' = 500$ kPa
(a)
(b)
(c)
(d)
(e)
(f)
90° 75° 60° 45° 30° 15° 0°
105° 120° 135° 150° 165° 180°
0 1000 2000 3000 4000 5000

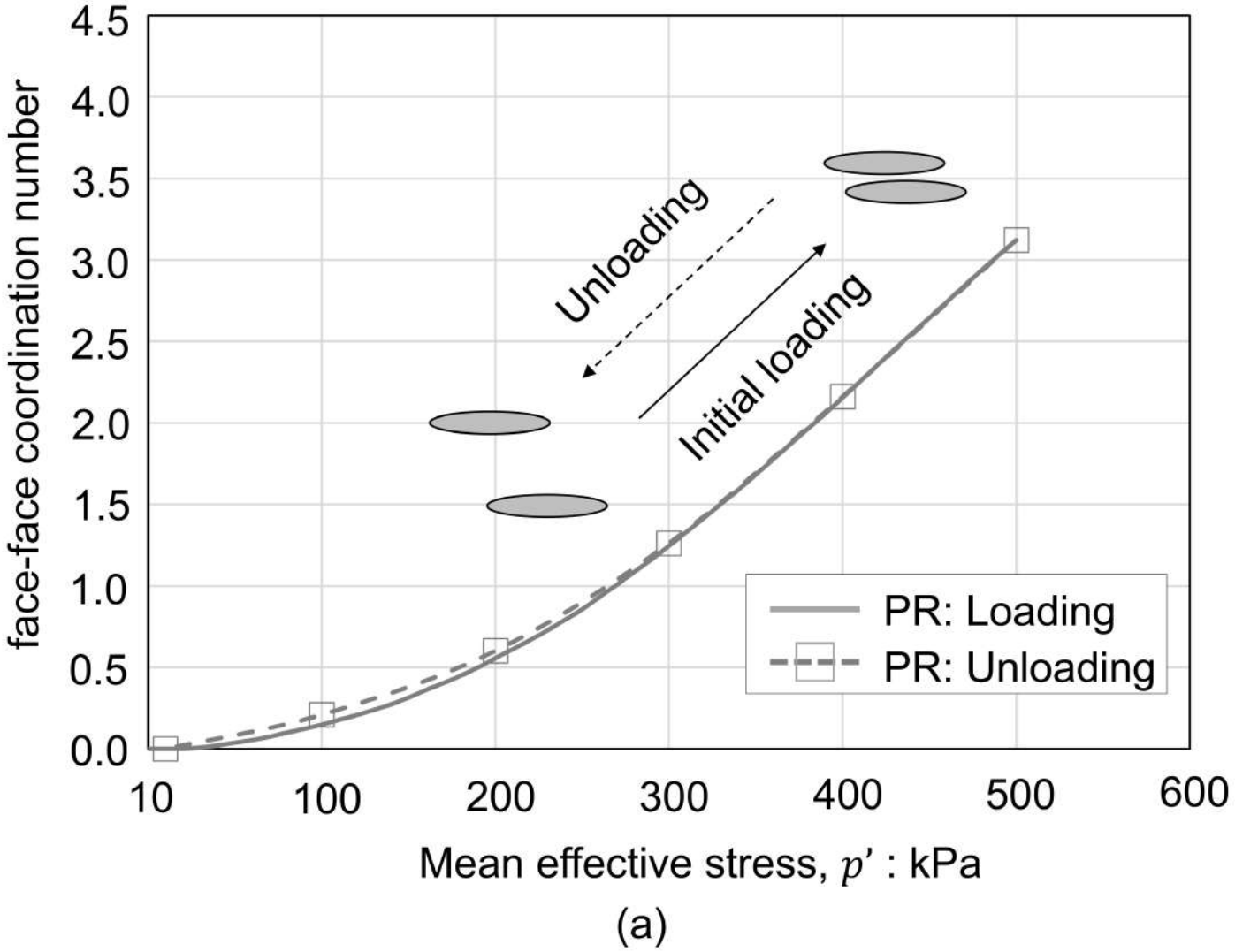

PR: Loading
PR: Unloading
Loading
Unloading
from 100 kPa
from 200 kPa
from 300 kPa
from 400 kPa
from 500 kPa
Void ratio, e
1.00
0.95
0.90
0.85
0.80
0.75
0.70
0.65
0.60
0.55
1
10
100
500
1000
Mean effective stress, p' : kPa
(a)

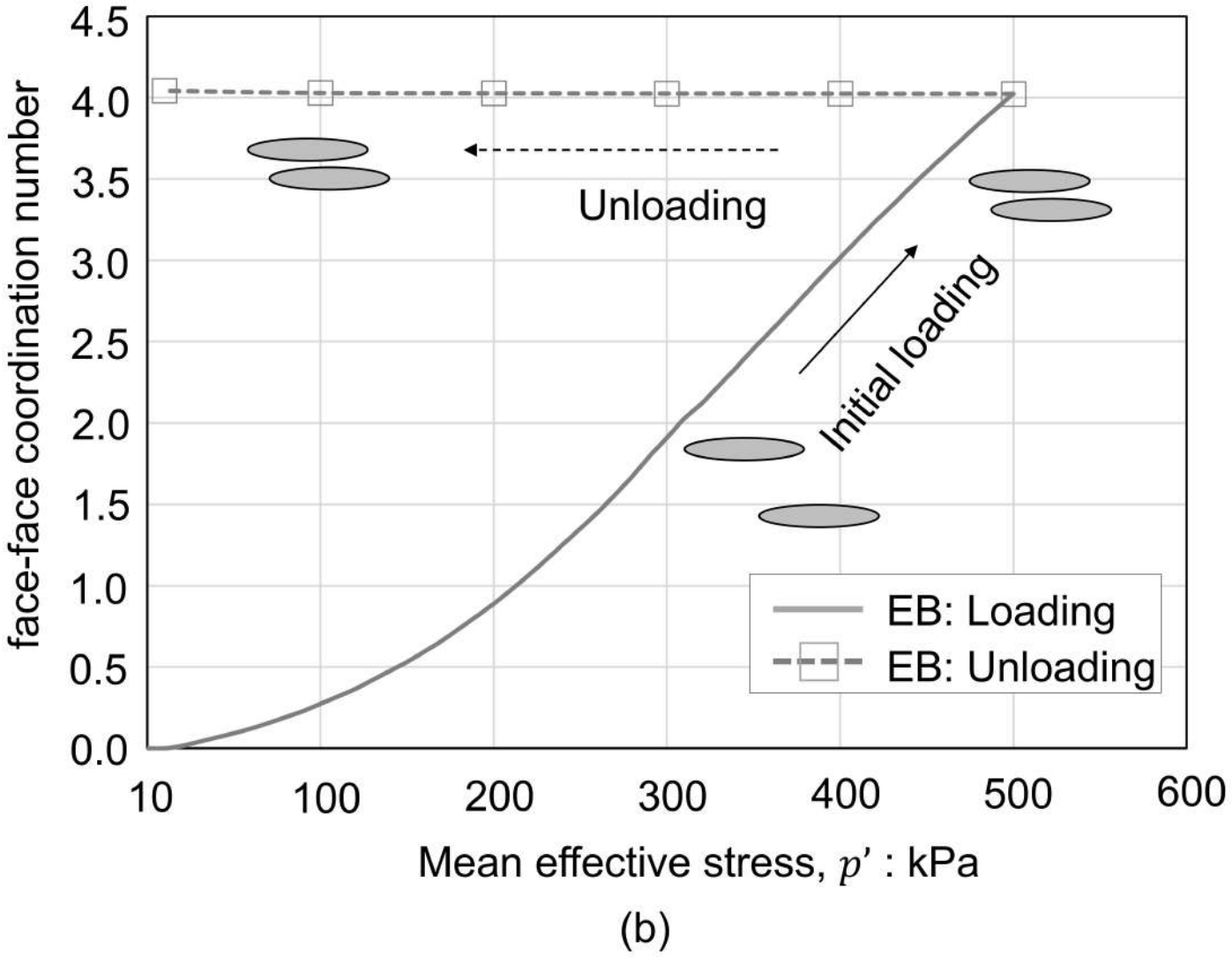

1.00
0.95
0.90
0.85
0.80
0.75
0.70
0.65
0.60
0.55
Void ratio, e
EB: Loading
EB: Unloading
Loading
Unloading
from 100 kPa
from 200 kPa
from 300 kPa
from 400 kPa
from 500 kPa
1
10
100
500
1000
Mean effective stress, p' : kPa

(b)

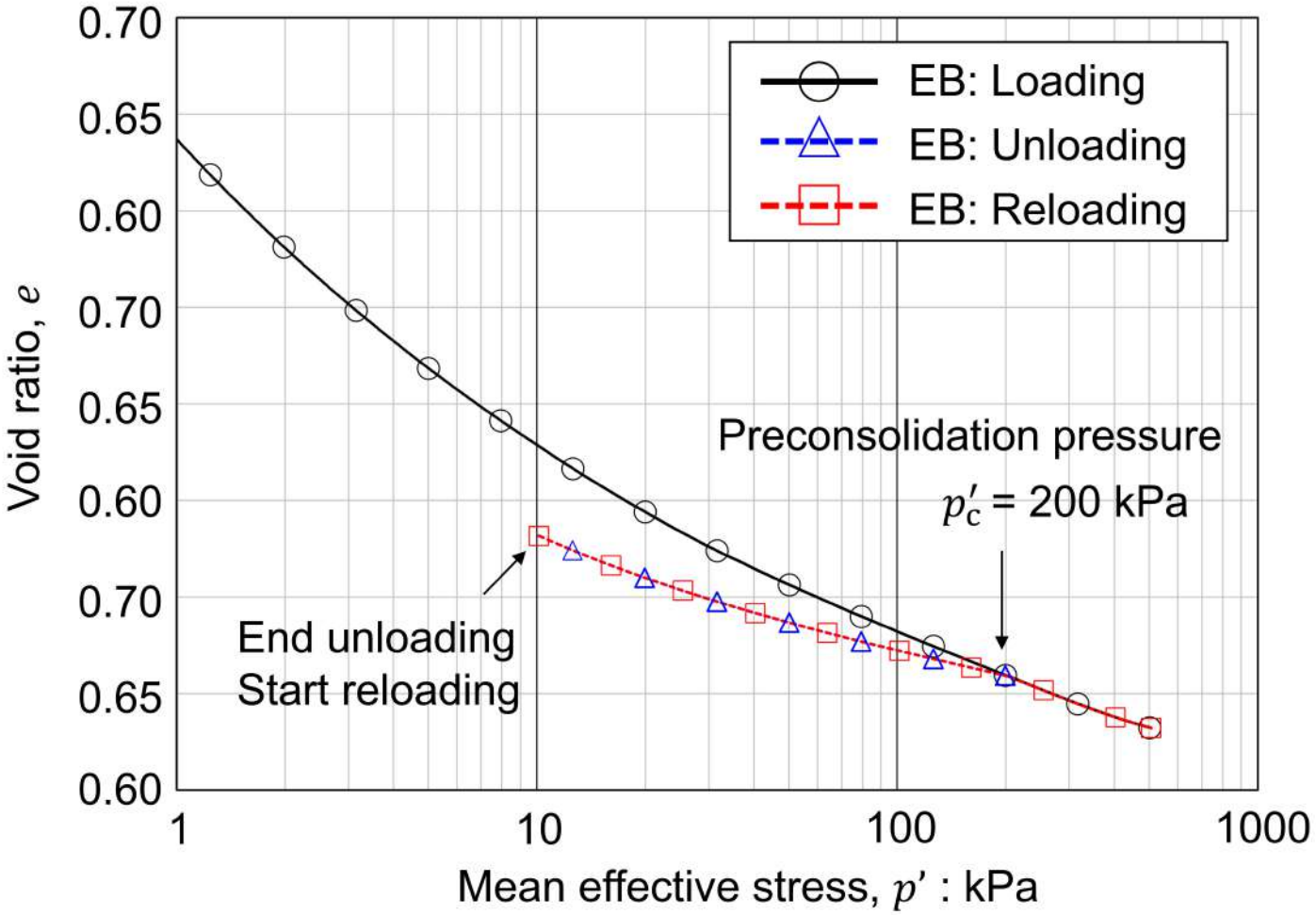

h_{12}=0
PR: Loading
p'=100 kPa
KDE
Number, N
Surface-to-surface distance, h_{12}: nm
h_{12}=50
PR: Unloading
(from 100 kPa)
p'= 10 kPa
KDE
h_{12}=0
PR: Loading
p'=300 kPa
KDE
Number, N
Surface-to-surface distance, h_{12}: nm
h_{12}=50
PR: Unloading
(from 100 kPa)
p'= 10 kPa
KDE
h_{12}=0
PR: Loading
p'= 500 kPa
KDE
Number, N
Surface-to-surface distance, h_{12}: nm
(a)
h_{12}=50
PR: Unloading
(from 500 kPa)
p'= 10 kPa
KDE
Number, N
Surface-to-surface distance, h_{12}: nm
(b)

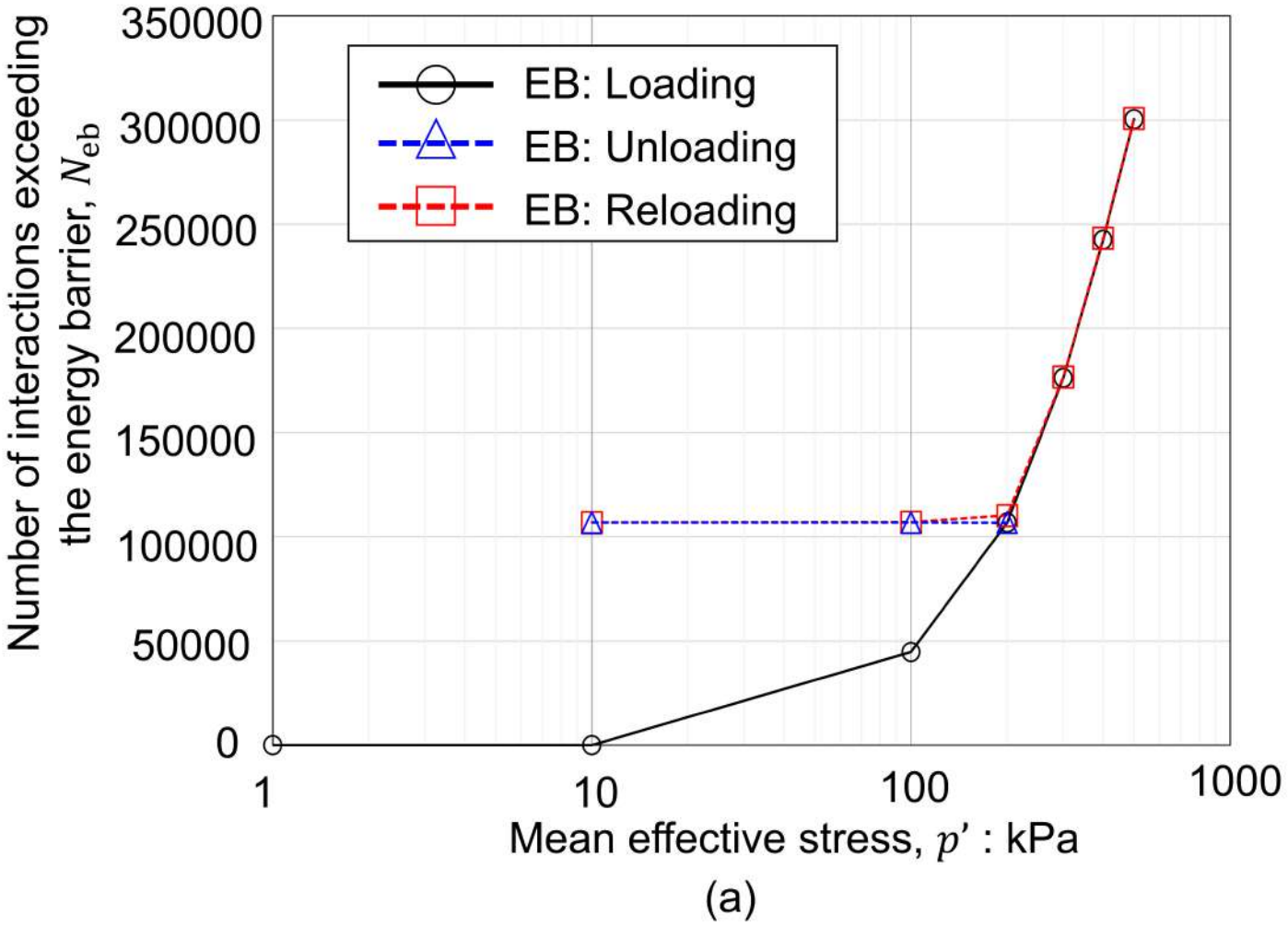

Energy barrier
h_{eb}=4.64 nm
EB: Initial loading
p'= 100 kPa
KDE
EB: Unloading
(from 100 kPa)
p'= 10 kPa
EB: Initial loading
p'= 300 kPa
EB: Unloading
(from 300 kPa)
p'= 10 kPa
EB: Initial loading
p'= 500 kPa
EB: Unloading
(from 500 kPa)
p'= 10 kPa
Number, N
Surface-to-surface distance, h_{12}: nm
(a)
(b)

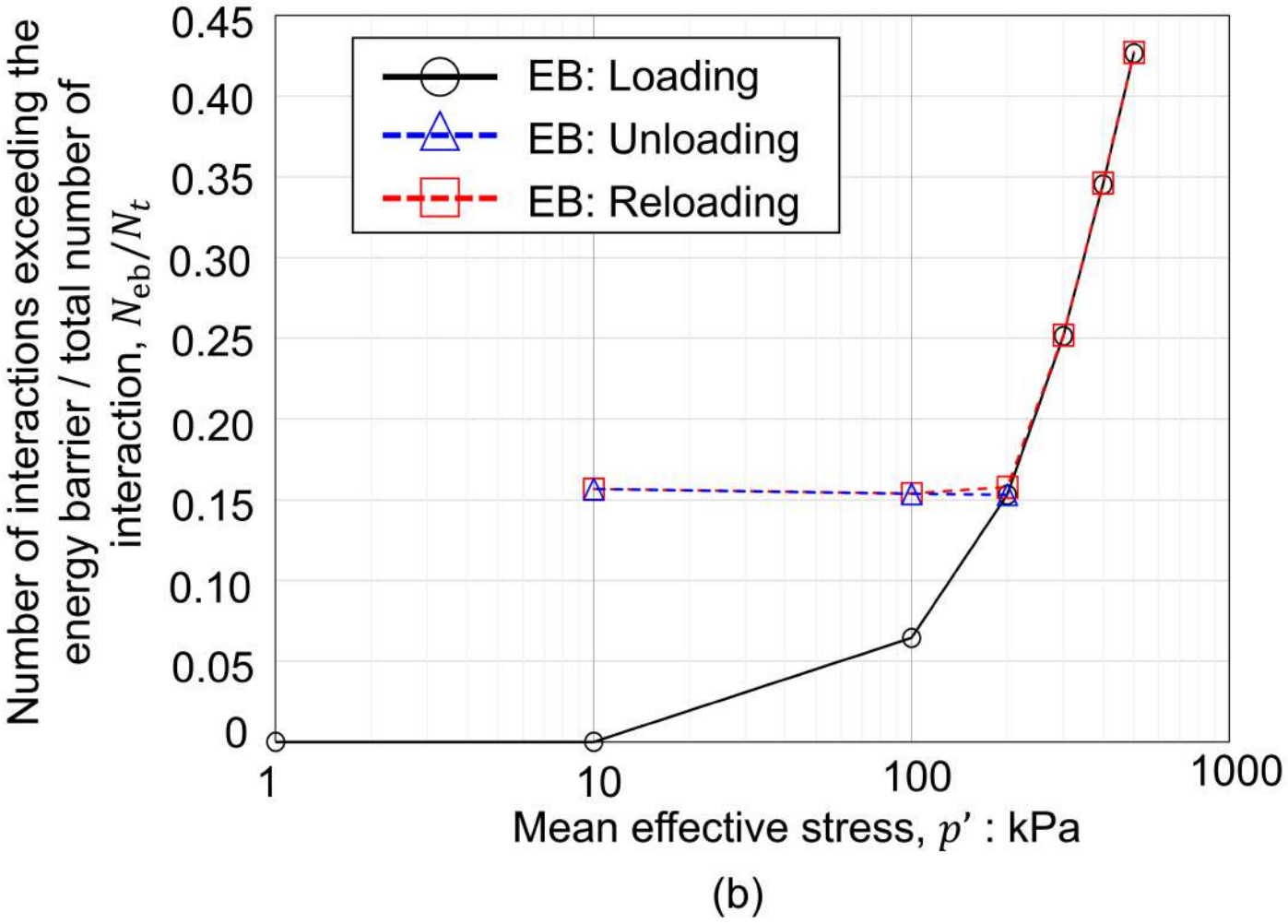

face-face coordination number
4.5
4.0
3.5
3.0
2.5
2.0
1.5
1.0
0.5
0.0
10
100
200
300
400
500
600
Mean effective stress, p' : kPa
Unloading
Initial loading
PR: Loading
PR: Unloading
(a)

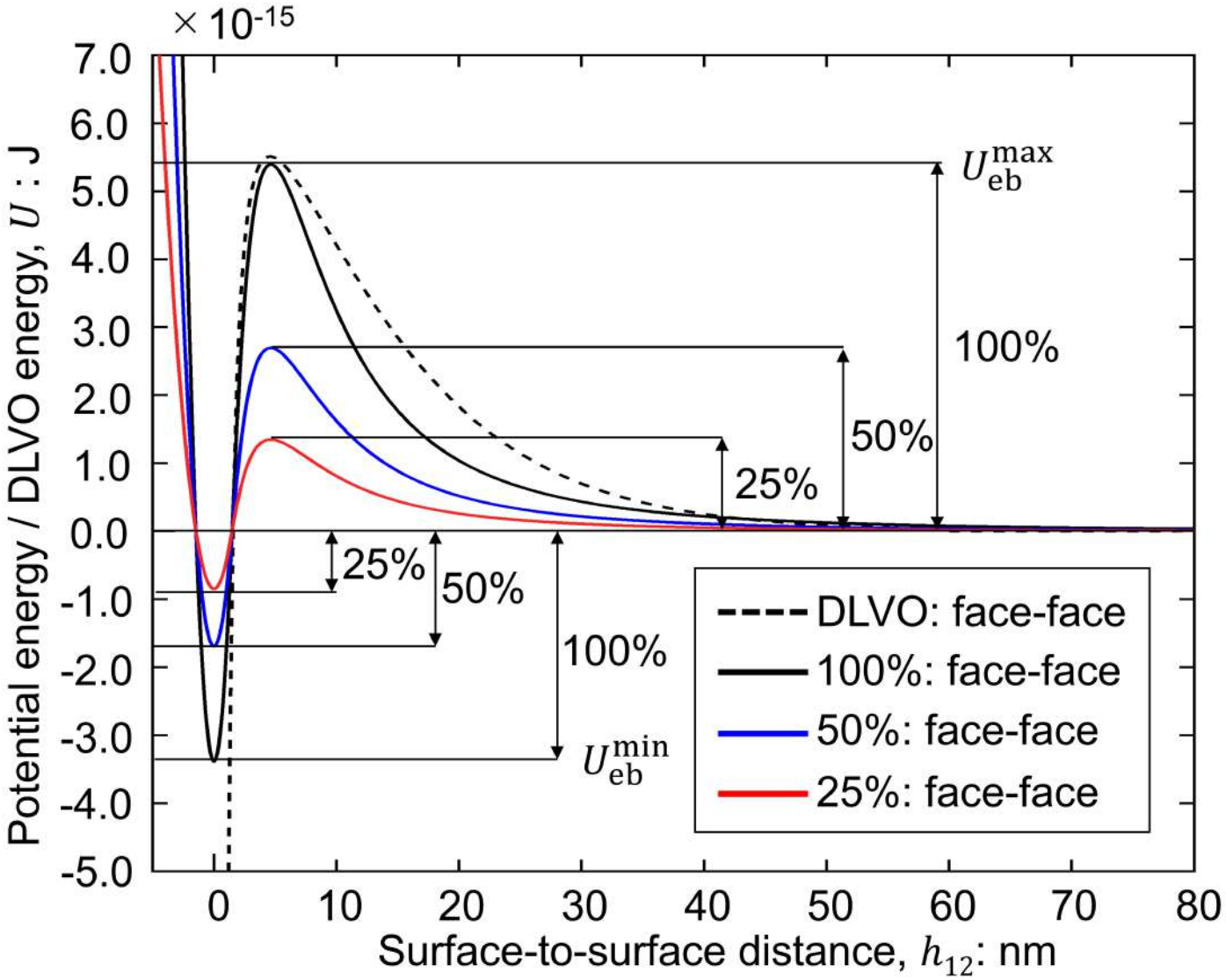

face-face coordination number
4.5
4.0
3.5
3.0
2.5
2.0
1.5
1.0
0.5
0.0
10
100
200
300
400
500
600
Mean effective stress, p' : kPa
Unloading
Initial loading
EB: Loading
EB: Unloading

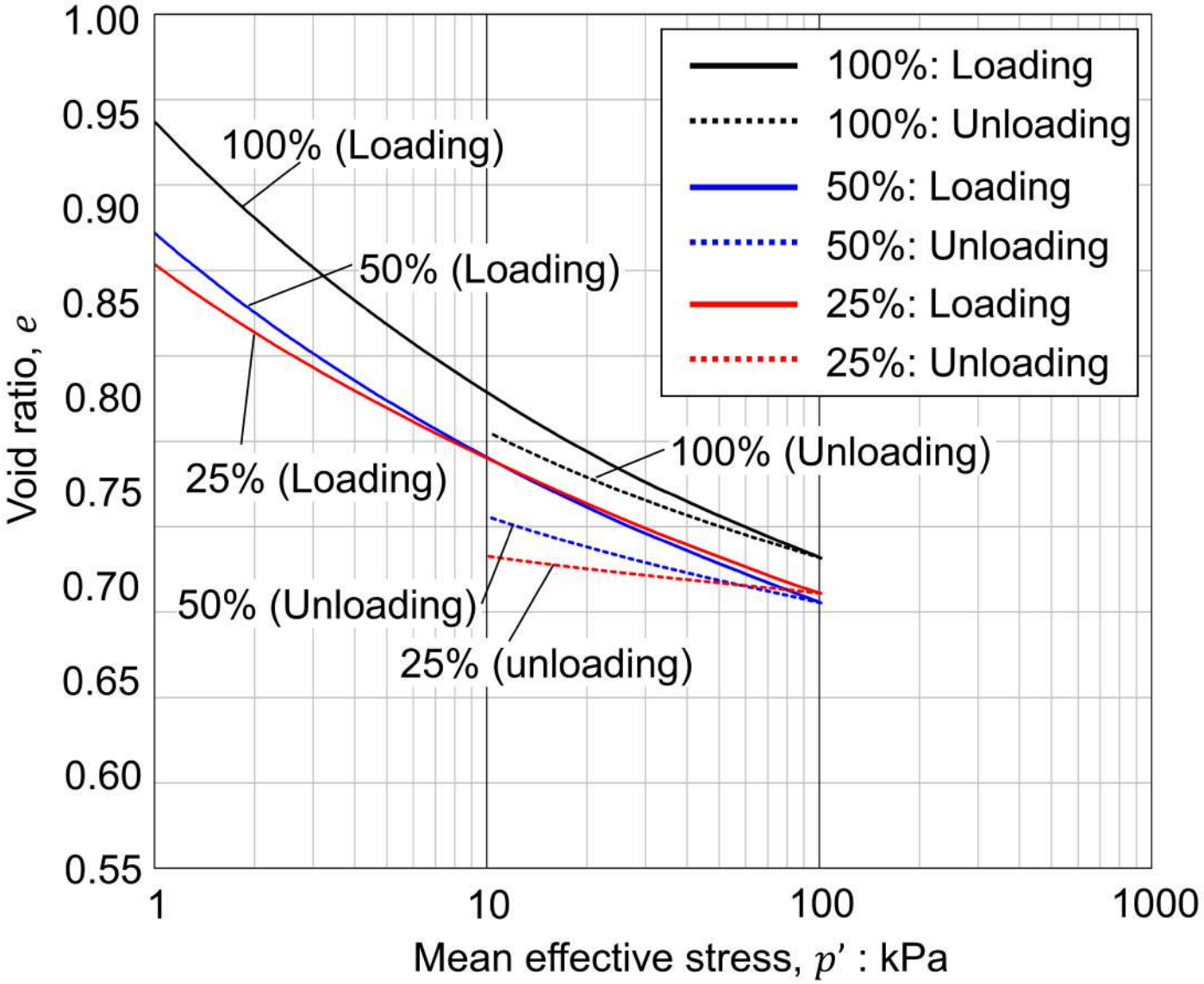
(b)

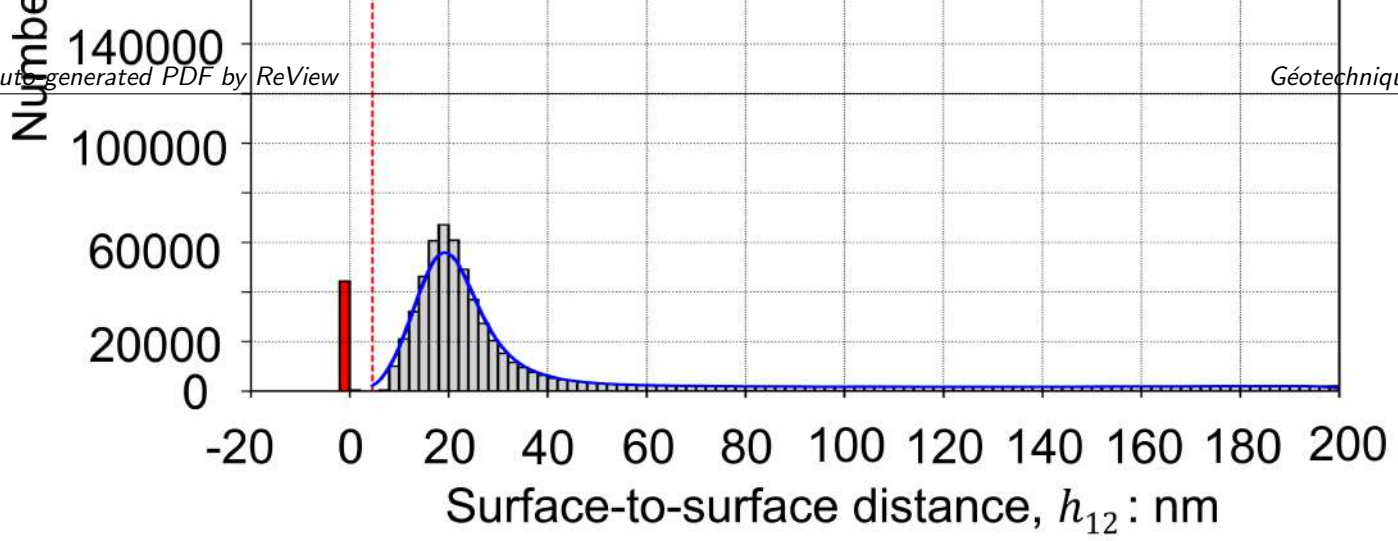

0.70
0.65
0.60
0.70
0.65
0.60
0.70
0.65
0.60
Void ratio, e
1
10
100
1000
Mean effective stress, p' : kPa
EB: Loading
EB: Unloading
EB: Reloading
Preconsolidation pressure
p'_c = 200 kPa
End unloading
Start reloading


EB: Loading
EB: Unloading
EB: Reloading
Number of interactions exceeding the energy barrier, N_{eb}
350000
300000
250000
200000
150000
100000
50000
0
1
10
100
1000
Mean effective stress, p' : kPa
(a)

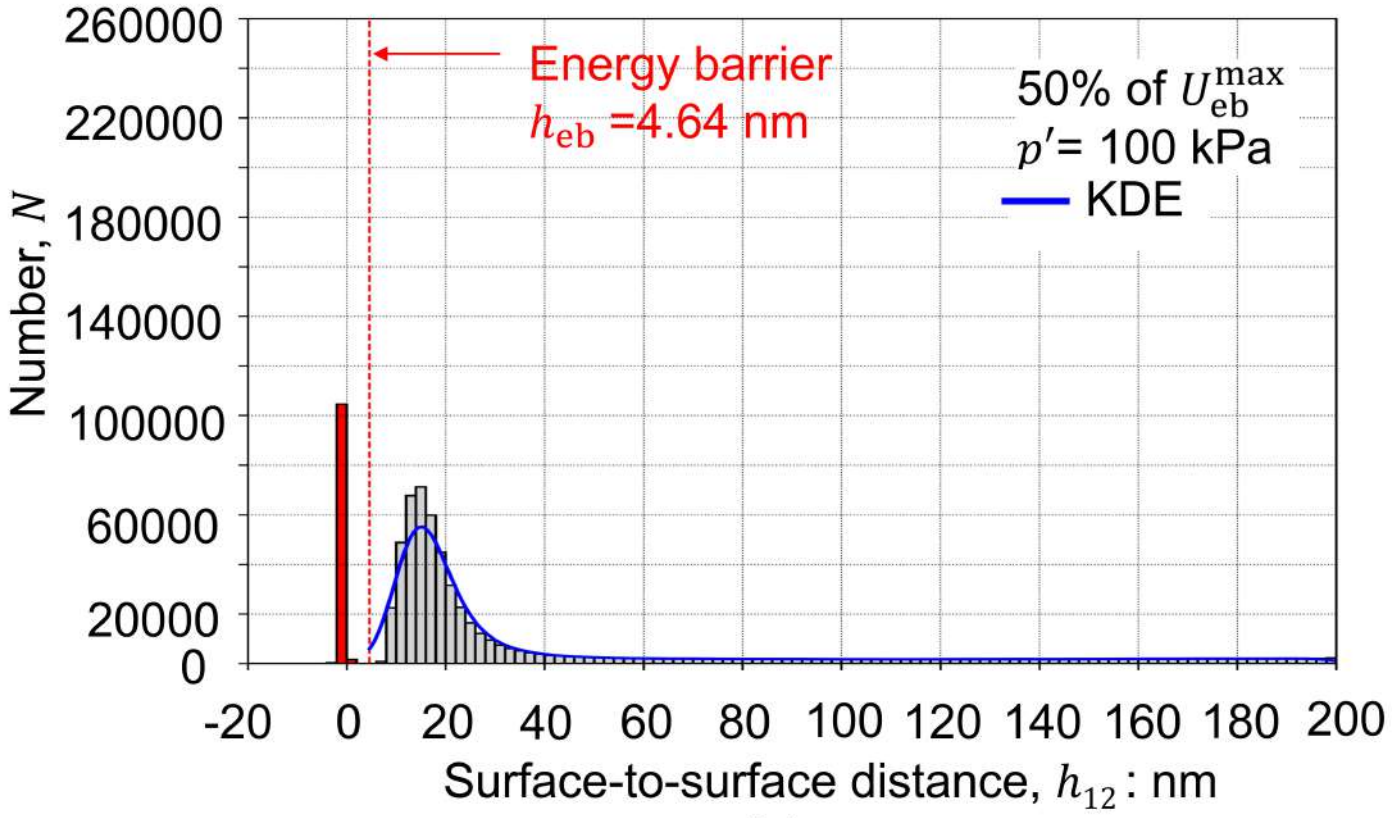

Number of interactions exceeding the energy barrier / total number of interaction, N_{eb}/N_t
0.45
0.40
0.35
0.30
0.25
0.20
0.15
0.10
0.05
0
EB: Loading
EB: Unloading
EB: Reloading
1
10
100
1000
Mean effective stress, p' : kPa
(b)


× 10-15
Potential energy / DLVO energy, U : J
Surface-to-surface distance, h12: nm
DLVO: face-face
100%: face-face
50%: face-face
25%: face-face
Ueb max
Ueb min
100%
50%
25%
25%
50%
100%

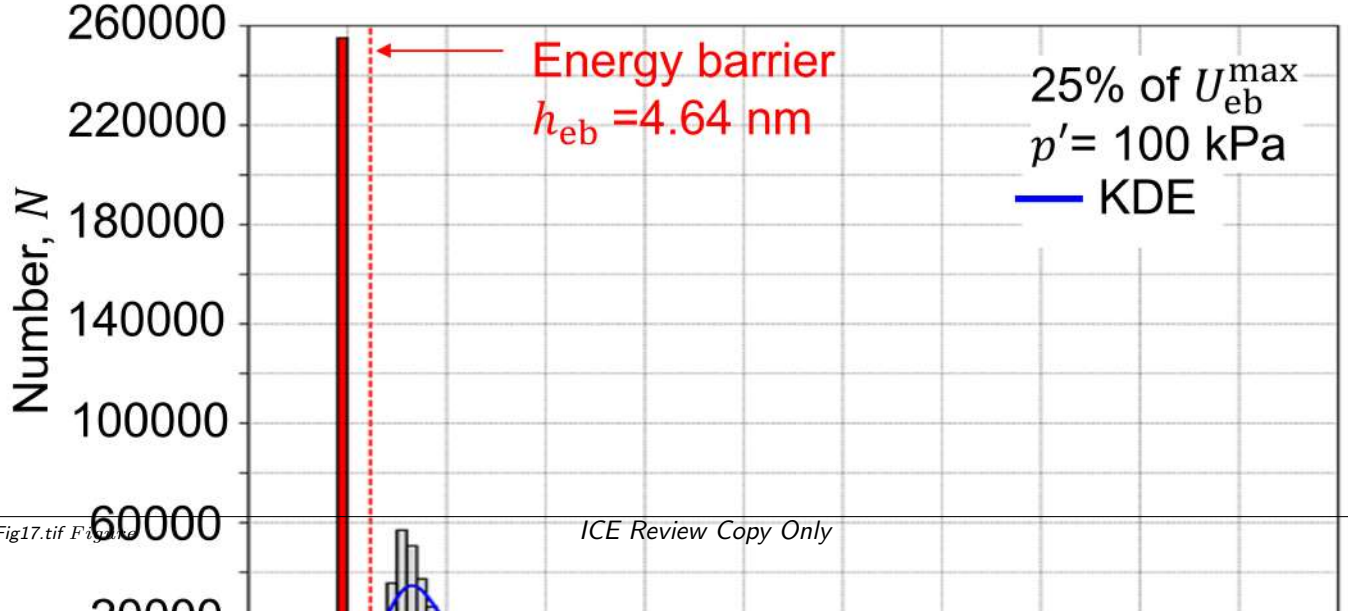

1.00
0.95
0.90
0.85
0.80
0.75
0.70
0.65
0.60
0.55
Void ratio, e
1
10
100
1000
Mean effective stress, p' : kPa
100%: Loading
100%: Unloading
50%: Loading
50%: Unloading
25%: Loading
25%: Unloading
100% (Loading)
50% (Loading)
25% (Loading)
100% (Unloading)
50% (Unloading)
25% (unloading)


Number
140000
100000
60000
20000
0
-20
0
20
40
60
80
100
120
140
160
180
200
Surface-to-surface distance, h_{12} : nm

(a)


Number, N
260000
220000
180000
140000
100000
60000
20000
0
Energy barrier
h_{eb} =4.64 nm
50% of U_{eb}^{max}
p'= 100 kPa
KDE
-20
0
20
40
60
80
100
120
140
160
180
200
Surface-to-surface distance, h_{12} : nm

(b)


Number, N
260000
220000
180000
140000
100000
60000
Energy barrier
h_{eb} =4.64 nm
25% of U_{eb}^{max}
p'= 100 kPa
KDE